Large-scale imaging of optical antennas and single molecules

Doctoral Thesis

by

Lisa Saemisch

Thesis Advisor:
Prof. Dr. Niek F. van Hulst

ICFO – Institut de Ciències Fotòniques
BIST – Barcelona Institute of Science and Technology
UPC – Universitat Politècnica de Catalunya

March 2021

Thesis advisor:

Prof. Dr. Niek F. van Hulst

Thesis committee:

Dr. Esther A. Wertz (Rensselaer Polytechnic Institute, NY, U.S.A.)
Prof. Dr. Lukas Novotny (ETH Zürich, Zürich, Switzerland)
Prof. Dr. María García-Parajo (ICFO – Institut de Ciències Fotòniques, Castelldefels, Spain)

To my parents. You are more than I could have ever wished for.

Acknowledgements

My PhD journey began when Niek decided it would be a good idea to keep me in his group (I hope you still think it was!), upgrading from a Master to a PhD Student. Thank you Niek, for giving me this amazing chance. While you are not the typical boss - giving more scientific freedom than most other and loving to have a casual conversation over a few cups of coffee - you let me go-and-fly to exactly where I am now - defending my thesis. Thank you for all your advice along the way, for the constructive criticism and the encouragement, for the opportunity to present my work even at the most remote locations in Europe and for all the great conversations over a cup of coffee or a rare-to-medium Argentinian steak.

I am wondering where my thesis journey would have gone without Matz. I think I cannot thank you enough for trusting me with the ideas that keep pouring out of your brain. Thank you for all the help you provided in all the times that desperate-me came knocking on your door, for the many hours enclosed in the lab together, for all the times you kept pushing me, for the laughter and the nightmares you have caused me. And of course, for the mushrooms. Danke!

I have been part of the MolNanoPhot group for almost six years now - a long time with many people to thank for great discussions, advice and great times. Ion, thank you for teaching me how to not-get-crazy fabricating tiny gold nanostructures. Thank you James, for being such a great first mentor. Thank you Gaetan and Alex for all the Matlab help. Thank you Nicola, for accompanying me to (almost) every conference and for sharing a lab and the crazy nanoantenna work. Gracias a Unai por todas las risas en la ofi, por compartir la pasión de la montaña así como la carga de trabajar con holografía. Thank you Jana, for the many outdoor and indoor adventures that we have enjoyed together and for all your advice in the past years. Grazie Luca, for great Risottos and Tiramisu, and your hugs that always came when I needed them. Thanks to the other past and present members of our group, Nicolò, Łukasz, Richard, Anshuman, Vikas, Esther, Alex D, Monse, Paweł, Giulia and Saurabh. I will miss being part of this group. I would also like to thank Leticia and her research group, who made me feel very welcome when I first came to ICFO as an internship student.

Thanks to all ICFO units, who have largely contributed to making ICFO not only a great place do to science, but also a place to feel welcome and home. A special thanks goes to Anne, my adopted mum-in-Spain, not only for your countless emails of solutions to all kinds of problems, but also the many lovely moments we shared together.

I am beyond grateful for all the people I have met at ICFO during these years and with whom I share countless amazing memories. Irene, gracias por mostrarme

la belleza de yoga, por poner los pastelitos de chocolate más ricos en mi mesa, y por bailar y sonreir juntas. Pamina, danke für die vielen schönen Spaziergänge zusammen und deine offenen Ohren. Sarah, thanks for beers (+water), music and just great times. Kavitha, thanks for my culinary enlightenment caused by your beautiful wedding. Sandra, gracias por crear el diccionario "Sandra-Español-Español-Sandra" en mi cabeza, y gracias a ti y Antoine por el viaje más chulo en bici. Kevin und Achim, danke für die ganzen geilen IFF-"Partys", die wir zusammen gefeiert haben. Gracias a Silvana, Miriam, Juan, Pau, Ferran y Miquel por aceptarme con agua cuando solo habían cervezas, por los bailes y risas a altas horas de la noche y por desesperarme de seguir una conversación en español con cuatro accentos diferentes.

Gracias a Bruno y Enoe por convertiros en mis primeros amigos en Barcelona y todos los momentos bonitos que hemos tenido desde entonces. Gracias a Jenny, por compartir la pasión de atletismo y mostarme la cultura catalana. Thanks to Barbara and Raissa, who make opening the entrance door feel like coming home. Thanks to Milka and Lindt, which made every moment a bit happier.

Stefan, Martin und Bj, ohne euch hätte ich den Bachelor und Master nicht überlebt. Danke für die stundenlangen Praktikumsauswertungen, die gemeinsame Verzweiflung über absurden Aufgaben und die wunderschöne Zeit zusammen.

Betti und Felix, danke (ihr wisst schon, so für alles!). Caro, irgendwie haben wir es beide geschafft vom Sport in die Physik zu sprinten/springen, und irgendwie bin ich der festen Überzeugung, dass du immer eine verdammt gute Freundin von mir sein wirst. San, danke für die vielen Jahre deiner Freundschaft, für deine Liebenswürdigkeit und für die coolste Geburtstagstorte überhaupt.

Vero, danke, dass du genauso verrückt bist wie ich, dass wir alle unsere schönen und schlechten Momente zusammen durchleben und du immer meine beste Freundin bleiben wirst. Wir rocken das Leben.

Danke an Oma und Alfred, dass ihr immer an mich geglaubt habt.

Gracias Roly, por mostrarme el sol siempre cuando yo no lo veía, por subir y bajar las montañas más altas bajo la lluvia y bajo el sol, por explicarme la locura de las transformaciones de Fourier, por tu cariño infinito y claro, por la R.

Balu, danke für deine Fellbällchen, deine Samtpfoten und die ständige Vorfreude, mit dir zu schmusen.

My last and infinite gratitude goes to my parents. Mama und Papa, danke, dass ihr immer an mich geglaubt und mich bedingungslos unterstützt habt, dass ihr die schönen Momente mit mir gemeinsam feiert und die schwierigen Momente mit mir durchsteht und dass ich bei euch immer ich sein kann. Ich liebe euch.

Lisa's Adventures in Nanowonderland

This informal summary is dedicated to my family and non-nerd friends, and to all other people with a non-related background who are interested in knowing what I did during the past four and a half years of my life, hiding in a dark cave called "lab" and forming some tiny tiny gold structures in a very-clean-room.

1 The story of a molecule falling in love with a nanoantenna

The two things I have been mainly working with during my PhD are molecules and nanoantennas. A nanoantenna can help explore, manipulate and control the properties of the molecule. In my thesis, we put the emphasis on exploring *a lot* of encounters of a single molecule and a nanoantenna, to explore their different kind of behaviors from a statistical point of view - because every *relation* is different and cannot be judged by looking at only one example.

Molecules are compounds of two or more atoms and everything we can see around us is made of molecules - the table, the building, humans, the trees, the stars and most of the ocean and the atmosphere. Therefore, to understand matter in general and the processes in nature, it is crucial to explore molecules. Nanoantennas can help doing so. They are tiny antennas of approximately the size of a virus and work in the visible region of the spectrum, hence they are counterpart to conventional radio or telecommunication antennas. Radio antennas can transmit and receive radio waves and are the main tool of communication in our daily lives, integrated in radios, smartphones and television. These radio waves travel (in vacuum) at the speed of light and extend spatially from one millimeter to hundreds of kilometers. Their length avoids the interaction with objects that are smaller than they are and hence they easily pass atmosphere and most building materials. Unfortunately we cannot use them to explore molecules, because most molecules absorb and emit light at visible wavelengths, which is the light that we see all around us. These wavelengths are only hundreds of nanometers long, contrarily to the huge wavelengths radio antennas use, and therefore radio antennas cannot help us to access molecules - but *nanoantennas* do! These nanoantennas are small metal particles, usually made of gold, silver or aluminum. They are about 50 nanometers wide and 60 to 180 nanometers long - so roughly as big as a (corona)virus. Special machines are needed to fabricate such small structures, and this is why I spend so much time in a very-clean-lab operating big

machines to fabricate tiny structures. When the fabrication of the nanoantennas is done, we put molecules on top. The molecules must be able to *talk* to the nanoantenna, meaning that the molecule has to absorb and emit approximately the same wavelength of light as the nanoantenna.

When the molecule and the nanoantenna come very close, fall in love so to speak, the nanoantenna has a decisive influence on the properties of the molecule (Figure 1). This is what I have explored in my thesis work. The nanoantenna lets the molecule produce more light, so we see the molecule much brighter than usual. Normally, a molecule not only emits light of one wavelength, but a broad spectrum of light with more or less light intensity at different wavelengths - hence it emits different colors. The nanoantenna also influences the intensity with which the molecule emits light of different wavelengths and it therefore changes the color of the light emitted by the molecule.

The last drawing in Figure 1 shows the deflection of light by the nanoantenna. Here, the nano-antenna influences where the light that is emitted by the molecule comes from. In our microscope, we see the light from the molecule at a different location than where the molecule is actually placed. However, this shift in the position of the light only occurs in the nanometer range.

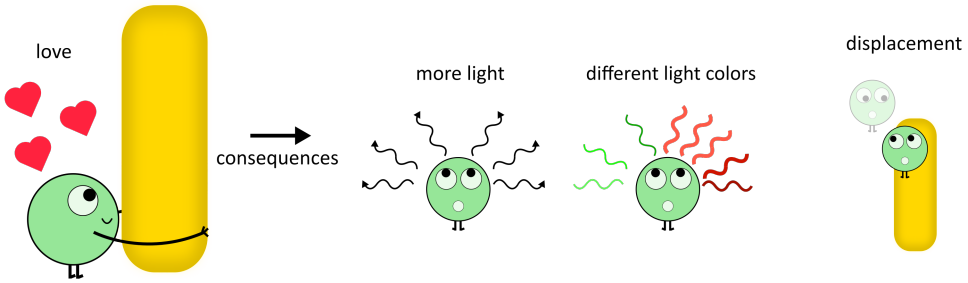

Figure 1: The molecule and its nanoantenna. When the molecule is really close the the nanoantenna (left), it emits more light, and depending on their mutual relationship also more light of a distinct color. The light from the molecule can also get deflected by the antenna, such that the molecule seems to be in a different place than it actually is (right).

Since every experiment involved a lot of single molecules falling in love with different antennas, we had the luxury of finding the encounters of strongest love - here we say the molecule that *coupled* most to the nanoantenna. The strongest coupled molecules showed the strongest change in their properties.

In the last part of my research work, I no longer worked with molecules, but only with very small gold particles and the light that they scatter. Scattered light is all around us. We see trees, buildings, fellow human beings and the blue sky because

small light-particles, photons, from the sun are scattered by these "structures" and hit our eyes. In my case, we are examining the light that is scattered by small gold particles. In particular, we want to determine the phase of this scattered light, since the phase reveals the current state of the scattered light. It is hard to imagine what exactly a phase is. As an analogy, one can look at the back and forth movement of a swing, where the phase of the swing provides information about its current position and direction of movement. We (unfortunately) didn't have a swing in the laboratory. Instead, we determined the phase of laser light that is scattered off gold nanoparticles.

Like radio antennas only work at certain frequencies or wavelengths, our nanoparticles have a certain wavelength where they work best at. If we shine light of that best-working wavelength onto the nanoparticle, the light will go back-and-forth in the particle - it will *oscillate*. After the oscillation, the nanoparticle will scatter the light. If we take the wrong, non-resonant wavelength and shine it onto our nanoparticle, the light will not go back-and-forth in the particle. So the phase of the light will be different in the two cases. With our microscope we could detect this difference in phase. Other particles, that are made from different materials, do not have any back-and-forth oscillating behavior - much like if you were trying to get to work a radio antenna made out of plastic. So through their phase behavior, we were able to distinguish between different particles in the last part of my thesis work.

2 Outlook

Well, can all this help to change the world? Well, for sure the world of fundamental physics in my research area! But one can only speculate whether my research will one day find an application in people's daily lives.

If we look again at the relationships between a single molecule and a nanoantenna, we find that the mutual love, the coupling, exists in different strengths. Through my research work we can now select the greatest love of all - which also shows the greatest change in the properties of the molecule. This "simple" algorithm for selecting the strongest coupling could, for example, help biologists who also use molecules to explore certain biological processes. In addition, the coupling of the nanoantenna and the molecule can one day be used in organic solar cells - here, changing the color of a molecule could make the solar cell more efficient.

A look at the phase of a nanoparticle is helpful when biologists want to monitor cell properties. Nanoparticles can be injected into the cell and tracked by observing the phase of the scattered light, and thus inferring processes in the cell. Here, one can easily distinguish the nanoparticles from the rest of the cell, because they have a specific phase behavior, while the cell has no resonance phase.

Lisa's Abenteuer im Nanowunderland

Diese sehr informelle Zusammenfassung ist meiner Familie und meinen Nicht-Nerd-Freunden gewidmet, sowie auch allen anderen Menschen aus unterschiedlichen Wissenschaftsfeldern, die daran interessiert sind zu erfahren, was ich in den letzten fünf Jahren meines Lebens gemacht habe, während ich mich in einer dunklen Höhle namens "Labor" versteckt und in einem sehr sauberen Raum winzige Goldstrukturen hergestellt habe.

1 Die Geschichte eines Moleküls, das sich in eine Nanoantenne verliebt

Die beiden wichtigsten Dinge, an denen ich während meiner Promotion gearbeitet habe, sind Moleküle und Nanoantennen gewesen. Eine Nanoantenne ist eine winzige Antenne, die helfen kann, die Eigenschaften des Moleküls zu erforschen, zu manipulieren und zu steuern. In meiner Doktorarbeit haben wir den Schwerpunkt auf das Erforschen vieler Begegnungen eines einzelnen Moleküls und einer Nanoantenne gelegt, um ihre verschiedenen Verhaltensweisen mit statistischer Relevanz zu erforschen – denn jede Beziehung ist anders und kann nicht anhand eines einzelnen Beispiels beurteilt werden.

Moleküle sind Verbindungen aus zwei oder mehr Atome. Alles, was wir um uns herum sehen können, ist aus Molekülen gemacht – der Tisch, das Gebäude, wir selbst, die Bäume, die Sterne und der größte Teil des Ozeans und der Atmosphäre. Um also die Materie im Allgemeinen und die Prozesse in der Natur zu verstehen, ist es entscheidend Moleküle zu erforschen. Nanoantennen können dabei helfen. Nanoantennen sind ungefähr so groß wie ein Virus und sind das Gegenstück zu herkömmlichen Radio- oder Telekommunikationsantennen für den sichtbaren Bereich des Lichts. Radioantennen können Funkwellen senden und empfangen und dienen als Hauptmittel zur Kommunikation in unserem täglichen Leben, verarbeitet in Radios, Smartphones und Fernsehern. Die ausgesendeten Lichtwellen dieser Radioantennen bewegen sich (im Vakuum) mit Lichtgeschwindigkeit und erstrecken sich räumlich von einem Millimeter bis zu Hunderten von Kilometern. Die große Länge ihrer Wellen verhindert die Wechselwirkung mit Objekten, die kleiner sind als sie selbst - daher gelangen sie ungestört durch die Luft und die meisten Baumaterialien. Diese Radioantennen können wir aber leider nicht verwenden um Moleküle zu erforschen, denn die meisten Moleküle absorbieren und emittieren sichtbare Wellenlängen, somit wechselwirken sie

mit dem Licht, dass wir überall um uns herum sehen können. Die Wellenlängen dieses sichtbaren Lichts sind nur Hunderte von Nanometern lang, im Gegensatz zu den riesigen (Funk)Wellenlängen von Radioantennen. Damit können uns Radioantennen nicht helfen, Moleküle zu erforschen... das können nur sogenannte Nanoantennen.

Man kann sich Nanoantennen als kleine Metallstäbe vorstellen, meist hergestellt aus Gold, Silber oder Aluminium. Sie sind etwa 50 Nanometer breit und 60 bis 180 Nanometer lang - also ungefähr so groß wie ein (Corona-) Virus. Man benötigt spezielle Maschinen, um solche kleinen Strukturen herzustellen, was der Grund ist, weswegen ich so viel Zeit in einem sogenannten „Reinraum" verbracht habe. Sobald die Nanoantennen hergestellt sind, können wir die Moleküle neben sie legen. Die Moleküle müssen in der Lage sein, mit der Nanoantenne zu "sprechen". Dies bedeutet, dass das Molekül nicht nur in unmittelbarer Nähe der Nanoantenne sein muss, sondern auch ungefähr die gleiche Wellenlänge des Lichts absorbieren und emittieren muss.

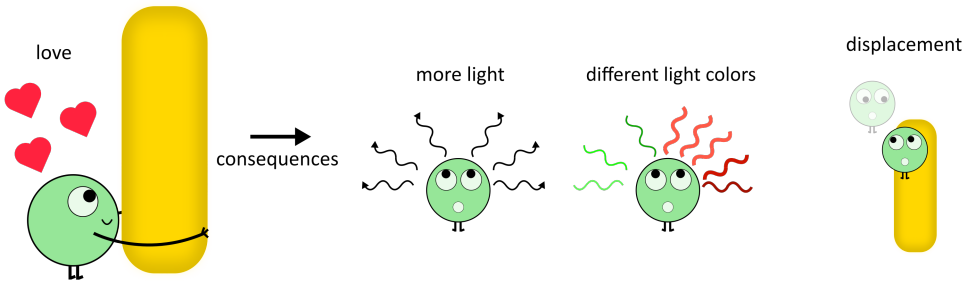

Figure 1: Ein Molekül verliebt sich in eine Nanoantenne (links), was dazu führt, dass es mehr Licht emittiert (2. Bild), sowie auch Licht in verschiedenen Farben (3. Bild). Eine Nanoantenne kann das Licht vom Molekül auch Ablenken, sodass es scheinbar von einem anderen Ort kommt, als sich das Molekül befindet.

Wenn sich Molekül und Nanoantenne nahe kommen, sich sozusagen verlieben, beeinflusst die Nanoantenne die Eigenschaften des Moleküls entscheidend (Figur 1). Plötzlich emittiert das Molekül viel mehr Licht, als wenn es keine Nanoantenna neben sich hätte. Normalerweise emittiert ein Molekül auch nicht nur Licht einer Wellenlänge, sondern ein breites Spektrum an Licht mit mehr oder weniger Intensität bei verschiedenen Wellenlängen – somit verschiedenen Farben. Die Nanoantenna beeinflusst ebenfalls, mit welcher Intensität das Molekül Licht von verschiedenen Wellenlängen emittiert – somit ändert sie Farbe des ausgestrahlten Lichts des Moleküls. Die letzte Zeichnung in Figur 1 zeigt die Ablenkung von Licht durch die Nanoantenne. Hier beeinflusst die Nanoantenne von wo das Licht kommt, das vom Molekül ausgesendet wird, und wir sehen dann in unserem Mikroskop das Licht an einem anderen Ort als das Molekül, was das Licht ursprünglich emittiert hat. Diese Verschiebung in der Position

des Lichts ereignet sich allerdings nur im Nanometerbereich.

Da bei jedem Experiment wirklich viele einzelne Moleküle mit verschiedenen Antennen wechselgewirkt haben, konnten wir ein paar Fälle finden, wo sich ein Molekül wirklich stark in eine Nanoantenne verliebt hat - wir haben das Molekül gefunden, das am meisten an die Nanoantenne gekoppelt war. Die stärkste Kopplung ist gleichbedeutend mit den stärksten Veränderung der Eigenschaften der Moleküle – also eine erhebliche Veränderung ihrer Farbe, der Intensität und der Ablenkung ihres Lichts.

Im letzten Teil meiner Arbeit habe ich nicht mehr mit Molekülen gearbeitet, sondern nur mit sehr kleinen Goldpartikeln und dem Licht, das sie streuen. Gestreutes Licht sehen wir überall um uns herum. Bäume, Gebäude, Mitmenschen und den blauer Himmel sehen wir, da kleine Lichtteilchen der Sonne von diesen "Strukturen" gestreut werden und auf unsere Augen treffen. In meinem Fall untersuchen wir das Licht, was von kleinen Goldpartikeln gestreut wird. Insbesondere wollen wir die Phase dieses gestreuten Lichts bestimmen, da die Phase etwas über den aktuellen Zustand des gestreuten Lichts aussagt. Es ist schwer sich vorzustellen, was genau die Phase ist. Als Analogie kann man die Hin- und Herbewegung einer Schaukel betrachten, bei der die Phase der Schaukel Auskunft über ihre aktuelle Position und Bewegungsrichtung gibt. Wir hatten (leider) keine Schaukel im Labor, haben aber trotzdem Laserlicht an Nanopartikeln gestreut und seine Phase bestimmt. So wie Funkantennen nur bei bestimmten Frequenzen oder Wellenlängen arbeiten, haben unsere Nanopartikel ebenfalls eine bestimmte Wellenlänge, wo sie am besten arbeiten und das Licht am effektivsten streuen. Bevor das Licht dieser bestimmten Wellenlänge vom Nanopartikel gestreut wird, geht das Licht im Partikel hin und her - es schwingt, weil es die Resonanz des Nanopartikels getroffen hat (wie in einem Resonator). Nach der Schwingung streut das Nanopartikel das Licht. Wenn wir allerdings die falsche, nicht-resonante Wellenlänge auf unser Nanopartikel richten, schwingt das Licht im Nanopartikel nicht hin und her, sondern wird sofort gestreut. Somit ist die Phase des gestreuten Lichts in beiden Fällen unterschiedlich, da einmal eine Schwingung stattfindet. Mit unserem Mikroskop konnten wir diesen Unterschied in der Phase sehen. Partikel aus anderen, nicht-metallischen Materialen lassen das Licht ebenfalls nicht hin- und herschwingen - ähnlich wie wenn man versuchen würden, eine Radioantenne aus Kunststoff zum Arbeiten zu bringen. Wegen ihres verschiedenen Phasenverhaltens konnten wir also im letzten Teil meiner Doktorarbeit zwischen verschiedenen Partikeln unterscheiden.

2 Ausblick

Kann meine Forschung dazu beitragen, die Welt zu verändern? Die Welt der fundamentalen Physik in meinem Forschungsbereich bestimmt! Ob meine Forschung eines

Tages eine Anwendung im täglichen Leben der Menschen findet, darüber kann man nur spekulieren.

Wenn wir nochmals Beziehungen eines einzelnen Moleküls und einer Nanoantenne betrachten, stellen wir fest, dass die gegenseitige Liebe, die Kopplung, in verschiedenen Stärken existiert. Durch meine Forschung können wir nun die stärkste Liebe von allen auswählen - die auch die stärkste Änderung der Eigenschaften des Moleküls zeigt. Dieser "einfache" Algorithmus zur Auswahl der stärksten Kopplung könnte zum Beispiel Biologen helfen, die ebenfalls mit Hilfe von Molekülen bestimmte biologische Prozesse erforschen. Zudem kann die Kopplung von Nanoantenne und Molekül eines Tages in organischen Solarzellen verwendet werden - hier könnte die Änderung der Farbe eines Moleküls die Solarzelle effizienter machen.

Ein Blick auf die Phase eines Nanopartikels ist hilfreich, wenn Biologen die Zelleigenschaften überwachen möchten. Man kann Nanopartikel in die Zelle injizieren und diese verfolgen, indem man die Phase des gestreuten Lichts beobachtet, und somit auf Prozesse in der Zelle schliessen. Man kann hier die Nanopartikel einfach vom Rest der Zelle auseinanderhalten, da sie ein spezifisches Phasenverhalten aufweisen, während die Zelle keine Resonanzphase hat.

Abstract

The interaction of light and matter is of crucial importance in fundamental science as well as in high-end technology. Ultimately, this concerns the interaction between a photon and a single quantum system, e.g. the absorption or emission of a photon by a single molecule. At room temperature this interaction is very inefficient as the absorption cross-section of a molecule is small compared to the wavelength of light, which inhibits many photons from interacting and hence limits the absorption, emission and scattering of a photon. An equivalent problem, and its solution, is found in our daily lives: small electric circuits (as found e.g. in our smartphones), which radiate very poorly by themselves, are linked to (radio) antennas to radiate and transfer information efficiently. Analogously, antennas working in the visible, so-called nanoantennas, are an effective tool to link matter and light. The strength of the coupling of a single molecule with a nanoantenna depends on many factors: the overlap of the antenna resonance and the molecular absorption/emission spectrum, the molecule's dipole orientation, the distance between molecule and nanoantenna, etc. Hence, strong interaction needs rather special conditions, which are hard to engineer. Moreover, to get a full interaction picture, a lot of single molecule encounters with different nanoantennas are needed - on one hand to make a statistically relevant statement including the many different factors and, on the other hand, to be able to observe the rare stronger interactions, that would have stayed hidden in experiments of only a few encounters.

The central idea of this thesis is to statistically map and control the interactions of a very large number of single molecules with different tailored nanoantennas, to cover the landscape of interaction factors and thus extend the current knowledge of the mutual interaction. For this purpose, a home-built wide-field microscope is combined with a large array of lithographically fabricated nanoantennas, which are all probed by freely diffusing molecules. Thus in time millions of encounters are recorded in parallel.

Chapter 2 introduces the necessary knowledge and methodology to understand the research work presented in chapters 3 to 5. Chapter 3 shows super-resolved nanoscale interaction maps of molecules and nanoantennas, linking the strength of interaction to the emission polarization and intensity of every encounter. Chapter 4 extends this approach by simultaneously recording the emission fluorescence and spectrum of every single molecule event, revealing strong spectral manipulation. Here, a suppression as well as an extreme enhancement of the vibrational sideband of the used molecule is observed. Additionally, the statistical mapping allows the freely diffusing molecules to encounter rare hotspots of extreme field intensities, enabling the observation of surface-enhanced Raman scattering.

Finally, chapter 5 takes the first step in the direction of characterizing the interaction of molecule and nanoantenna with high sensitivity via phase measurements. Here, an interferometric wide-field microscope enables the measurement of the absolute phase of nanoparticles and demonstrates the distinction of different plasmonic and dielectric particles via their phase behavior. Furthermore, we implement a novel two-color excitation method, capable of rapidly identifying two types of nanoparticles in a single-shot image.

Resumen

La interacción entre la luz y la materia tiene una alta importancia en la ciencia fundamental, así como en la tecnología de punta. En última instancia, esto se refiere a la interacción entre un fotón y un sistema cuántico, por ejemplo la absorción o emisión de un fotón por una sola molécula. En condiciones ambientales y temperatura ambiente, esta interacción es muy ineficiente ya que la sección transversal de absorción de una molécula es pequeña en comparación con la longitud de onda de la luz, lo cual inhibe la interacción de muchos fotones y, por lo tanto, limita la detección de absorción, emisión y dispersión. Un problema equivalente, y su solución, se puede encontrar en nuestra vida cotidiana: pequeños circuitos eléctricos (como los que se encuentran, por ejemplo, en nuestros smartphones) están conectados a antenas (de radiofrequencia) para emitir y transferir información de manera eficiente. De manera análoga, las antenas que trabajan en el visible, así llamadas nanoantenas, son una herramienta eficaz para vincular la materia y la luz. La fuerza del acoplamiento de una sola molécula con una nanoantena depende de muchos factores: la superposición del espectro de la resonancia de la antena y de absorción/emisión molecular, la orientación del dipolo de la molécula, la distancia entre la molécula y la nanoantena, etc. Por lo tanto, la interacción fuerte necesita condiciones bastante especiales, que son difíciles de generar. Además, para obtener una imagen completa de la interacción, se necesitan muchos encuentros de una sola molécula con diferentes nanoantenas, por un lado para hacer un estudio estadísticamente relevante que incluya los multiples factores y, por otro lado, para poder observar las menos frequentes interacciones más fuertes, lo que habría permanecido oculto en experimentos de solo unos pocos encuentros.

La idea central de esta tesis es mapear y controlar estadísticamente las interacciones de un gran número de moléculas individuales con diferentes nanoantenas adaptadas, para considerar todos los factores de interacción y así ampliar el conocimiento actual de la interacción mutua. Para este propósito, un microscopio hecho en casa de campo amplio se combina con una gran variedad de nanoantenas fabricadas litográficamente, que son todas probadas por moléculas que se difunden libremente. Así, con el tiempo, se registran millones de encuentros en paralelo.

El capítulo 2 introduce el conocimiento y la metodología necesarios para comprender el trabajo de investigación presentado en los capítulos 3 a 5. El capítulo 3 muestra mapas de interacción nanoescalar superresueltos de moléculas y nanoantenas, vinculando la fuerza de interacción con la polarización de emisión e intensidad de cada encuentro. El Capítulo 4 amplía este enfoque al registrar simultáneamente la fluorescencia de emisión y el espectro de cada evento de una sola molécula, revelando una fuerte manipulación espectral. Aquí, se observa una supresión así como una mejora

extrema de la banda lateral vibratoria de la molécula utilizada. Además, el mapeo estadístico permite que las moléculas que se difunden libremente encuentren puntos inusuales de intensidades extremas del campo eléctrico, lo que permite la observación de la espectrometría Raman de superficie mejorada.

Finalmente, el capítulo 5 da el primer paso para caracterizar la interacción de la molécula y la nanoantena con alta sensibilidad a través de mediciones de fase. Aquí, un microscopio interferométrico de campo amplio permite la medición de la fase absoluta de nanopartículas y demuestra la distinción de diferentes partículas plasmónicas y dieléctricas a través de su comportamiento de fase. Además, se implementa un novedoso método de excitación de dos colores, capaz de identificar rápidamente dos tipos de nanopartículas en una imagen de un solo disparo.

Contents

1 Introduction

1.1 Nanoscale interaction of optical antennnas and single emitters

The interaction between light and matter in free space is intrinsically a weak process, at least at ambient temperatures. The reason is a huge size-mismatch between the nanometric dimensions of single emitters - such as atoms, molecules and fluorescent dyes - and the incoming light-radiation. The probability of interaction between a photon and a single emitter is quantified by the emitters absorption cross-section. At very cold, cryogenic temperatures this absorption cross-section scales with the square of the wavelength of light. It is therefore very likely for a molecule placed in the center of a diffraction limited beam to interact with almost all of its photons - given that the wavelength of the photons matches the absorption wavelength of the molecule. In this scenario we can observe strong light-matter interactions. But the world outside the laboratory does not work at these very low temperatures but at normal, ambient temperatures. Here, the same molecule would, under ideal conditions, only interact with one in ten million photons - due to the mismatch between the small absorption cross-section of the molecule at ambient temperatures and the comparatively huge area of the diffraction limited beam. Hence we observe a very weak and very inefficient process. But exactly this light-matter interaction under ambient temperature conditions is of crucial importance to study, control and manipulate the fundamental properties of light emitters, with the potential for new advances in modern technology.

At this point, plasmonics enters to save the day. Plasmonics describes the coupling of freely propagating light to charges at the interface of metal and dielectric, resulting in electromagnetic waves that travel along this interface, which are known as surface plasmon polaritons (SPPs)[1,2]. The wavelength of these SPPs is shorter

than the wavelength of the freely propagating light exciting the plasmons, due to the dispersion porperties of noble metals such as gold, silver and aluminium. Consequently, the SPPs are able to confine the light into much smaller volumes than the freely propagating wave could, causing the concentration of electromagnetic waves into sub-diffraction-limited volumes at the surface of the metal, so called *hot spots*. These volumens are even reduced further by using metallic nanostructures instead of infinite metallic surfaces, which highly localize the SPPs (localized surface plasmon polaritons- LSPPs). Due to this high concentration of light over a nanometric volume, these *hot spots* enable a very strong field enhancement for an emitter placed in their vicinity[2–4] causing the emitter to absorb and emit much more light. This was first discovered in 1974 by Fleischmann and co-workers[5], who observed an unusually strong spectroscopic signal from pyridine molecules next to a silver electrode, which was three years later confirmed and explained as surface enhanced Raman scattering (SERS)[6,7]. A few years after the discovery of SERS, plasmon-enhanced fluorescence of molecules next to metallic films was observed and recognized[8–13]. Since then, the field has been evolving dramatically due to advances in nanofabrication and spectroscopic techniques, as well as biological and chemical sensing. As a result, numerous records of the detection and the fluorescence enhancement of single molecules next to different metallic nanostructures have been reported[14,15].

Here, single molecule measurements are prefered and needed, contrarily to easier ensemble measurements, to understand and explore the heterogenity of the nanoscale interaction. The interpretation of single molecule measurements is limited by the number of molecules measured, since every emitter can give slightly different results when put in an environment[16]. Due to the typical time-consuming factor of measuring single emitters one by one, the resulting publications typically do not exceed the measurement of 100 to 10000 single molecules[17,18] - which lowers their statistical relevance. The situation complicates itself even more when placing a molecule next to a nanostructure. Here, not only the molecules heterogeneity results in slightly different molecule-nanostructure interactions, but also the distance of molecule and nanostructure, their respective orientations and the overlap of their resonances play a crucial role.

In order to fully control the interaction of a single emitter and a nanostructure, near-field scanning optical microscopy (NSOM) has been used to scan a nanostructure, usually in form of a nanoaperature/nanoparticle/nanorod, in a fully deterministic way over a molecule. NSOM not only provides full vectorial control, but also nanoscale, sub-diffraction limited resolution. Since its first implementation in 1984[19], its precision has been improving, with aperature/antenna probes offering a resolution of about 5-50nm nowadays[20–23]. Hence, this fully deterministic measurement seems

to be the perfect tool to measure and map the nanoscale interaction of single emitter and nanoantenna. However, the experimental complexity and serial scanning of this approach dramatically limit its applicability and throughput. The build-up of the experiment takes at least a couple of years, every single nanoantenna tip needs to be fabricated and can easily be damaged during the measurement. This technique is furthermore limited by the minimal controllable distance between antenna and surface. In summary, it probably takes more than an entire PhD term to measure a detailed interaction of 20 molecules with 5 different antennas using NSOM.

1.2 Ensemble level-single molecule studies and beyond

In this thesis research, the aim is to measure the nanoscale interaction of a large number of single molecules with many different nanoantennas, to record statistically relevant results and to identify rare interaction cases with a robust and easy-to-use, home-built microscope. These requirements are met by combining super-resolution microscopy based on single molecule localization (single molecule localization microscopy - SMLM) with plasmonic nanoantennas. This combination promises high throughput measurements on a relatively easy-to-handle experiment, which allows not only for the easy exchange of excitation sources and samples but also for probing a large number of single molecules.

SMLM includes different widefield techniques such as STORM, PALM, DNA-PAINT and PAINT[24–27]. All of these techniques achieve sub-diffraction limited resolution by localizing the position of single fluorescent dyes on a very dense sample through activating only a fraction of the molecules at a time. Determining the position of all dyes in several hundreds to thousands of camera frames allows the reconstruction of a super-resolved image. STORM and PALM make use of the stochastic activation of switchable fluorescent dyes (STORM) or autofluorescent proteins (PALM) at fixed positions, and are therefore limited by the number of fluorescent emitters and their respective positions. The PAINT method however lets the molecules probe a sample fully stochastically and acquires the dyes position through a single blinking signal during adsorption, followed by desorption or photobleaching. While the DNA-PAINT method is limited by the number of DNA-strains on a surface or nanostructure, freely diffusing molecules with no specific place to bind (as used in PAINT) can - in theory - probe every nanometer of a sample - we just have to wait long enough.

SMLM in plasmonics was used first by Cang et al[28] to map sub-diffraction limited features on plasmonic substrates. They interrogated a rough metallic film using the

Brownian motion of freely diffusing molecules in solution and resolved surface regions of strong fluorescence enhancement which they attributed to hotspots of approximately 15 nm in size. Given that far-field localizations are strongly dependent on the orientation of an emitter it comes as no surprise that placing a resonant nanostructure next to a molecule can dramatically alter its apparent position. This phenomenon has received considerable attention and the position displacement of molecules close to different metallic nanostructures has been studied extensively with SMLM[28–36]. Despite these imaging problems, the combination of plasmonics with SMLM holds great promise for systematically studying the interaction between individual nanostructures and fluorophores.

In this PhD research, instead of observing the nanoscale interaction of only a few single molecules with one plasmonic nanostructure - as in NSOM or confocal microscopy -, thousands to millions of single molecules probing many different antennas at a time will be observed - all ideally within one day of the PhD life. The crucial parameters here are the widefield excitation and the detection of the entire excited area with a pixel-camera, allowing the observation of many interactions in parallel (Figure 1.1a) - contrarily to serial NSOM or confocal measurements, where a photo diode measures only a single point on the scanning sample (Figure 1.1b). The widefield approach shifts the problem of the time consuming measurement of a lot of single molecule encounters to the analysis of a huge amount of data - the main idea of my PhD project. The approach requires a high concentration of freely diffusing single molecules - hence an *ensemble*-level single molecule measurement - that probe a sample consisting of many different plasmonic nanoantennas. Apart from acquiring enough statistics to characterize thoroughly the nanoscale interaction, this method has the possibility to observe the *one-in-a-million* chance of seeing a specific rare interaction, which would likely stay hidden in a single-molecule-single-antenna measurement.

In this thesis work, I will first employ widefield localization microscopy to study the interaction of single molecules with plasmonic nanoantennas on an ensemble level. Here, I use statistics to analyze correlations of fluorescence intensity, polarization and the position error of the fitted molecular landings to discriminate between stronger and weaker interactions. Moreover, nanoscale interaction maps of strongly interacting molecules next to nanoantennas will be presented, that depend on the overlap of the resonance of molecule and nanoantenna, as well as their coupling strength.

Through dramatic changes in their radiative and non-radiative properties[3], nanoantennas also impact the overall emission spectrum of molecules through the selective spectral control of individual vibronic spontaneous emission rates. This spectral-reshaping induced by the nanostructure has remained largely unexplored and most of our understanding is based on ensemble-based experiments[37–39] where it is difficult

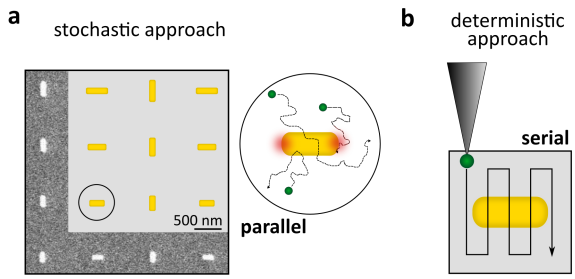

Figure 1.1: Parallel vs serial approach to measuring the nanoscale interaction of molecules and plasmonic antennas. a) Molecules are freely diffusing and probe a large sample containing nanoantennas of different length and orientation. An entire region on the sample is imaged onto the EMCCD with widefield microscopy, measuring different interactions in *parallel* - the stochastic approach. b) Fully deterministic approach, in which an NSOM with a molecule as tip scans over a sample containing nanoantennas. This method measures a single spatial point at a time, hence the need for scanning - the *serial* approach.

to distinguish overall spectral shifts from the potentially dominating contribution of individual, highly coupled, emitters. In the second part of my thesis, I monitor for the first time the spectral development of an ensemble of single molecules strongly interacting with different nanoantennas. Here, dramatic changes in the fluorescence spectra of single molecules will be observed, that depend on the resonance overlap of molecular emission and the different nanoantennas. The surprising observation of sharp, distinct peaks hints at the presence of even stronger coupling - in this case corresponding to surface-enhanced-raman-spectra (SERS) of many single molecules.

In these first two thesis parts, we see different coupling strengths between molecules and nanoantennas resulting in different interaction maps and different spectral manipulations. Here, the results always relied on intensity based measurements. The next step is now to better quantify the coupling of molecule and nanoantenna, with the possibility to observe an onset of strong coupling in the unified system. For this to happen, the coupling has to exceed both the cavity loss rate of the nanostructure and the emitter decay rate, such that the energy can cycle back and forth between matter and light components. In this case, a splitting into upper and lower hybrid plasmon-exciton bands is observed in the scattering spectra, going from a single peak in the scattering spectrum for weak coupling, to a double peak in the case of strong coupling[40,41].

But in our case of freely diffusing molecules probing different nanorods, the likeliness to observe a clear split in the scattering intensity spectrum is low. On one hand, nanorods do not provide a sufficiently confined mode volumen to get the required coupling strength. On the other hand, we are dealing with single molecules with a

small dipole moment - and not an ensemble combining lots of weak dipole moments to a strong one. Here, a promising alternative is to turn away from purely intensity based measurements to see a change in coupling. It is widely known in the surface plasmon sensing community, that detecting the phase change of a plasmonic nanoparticle is more sensitive than a change in amplitude[42,43].

Therefore, in the last part of my thesis, I will take the first step towards measuring the phase change of the combined system of nanoantenna and molecule, by measuring the absolute phase change of plasmonic and dielectric particles. A widefield off-axis holographic microscope has been built to measure the phase of different nanoantennas. The new microscope allows to distinguish plasmonic and dielectric nanospheres and identifies them in a one-shot approach. Beyond the possibility to measure a phase change of a strongly coupled system of molecule and nanoantenna, the knowledge of the absolute phase can push our understanding of nanoscale properties of plasmonic particles and can help to distinguish them from other dielectric particles in future detection and tracking measurements in physics and biology.

1.3 Thesis outline

- The following chapter 2 outlines the basic knowledge and the methods necessary to understand the results of my PhD thesis. Here, I will briefly describe the characteristics of plasmonic nanoparticles and single emitters. Furthermore, the fabrication process for gold nanoantennas and how to simulate their behavior with the used FDTD software will be explained in detail, as well as the setup and analysis procedure used for nanoscale interaction measurements in chapters 3 and 4.

- Chapter 3 presents the experimental results for the spatial nanoscale interaction of an ensemble of single molecules and many different nanoantennas. Here, the interaction of hundreds of thousands of molecules with nanoantennas depends on their respective resonance overlap. The results show correlations between their fluorescence intensities, fluorescence polarization and error in localization of their position. By treshholding and filtering these characteristics, the reconstructed interaction maps of molecules and nanoantenna can be dramatically altered. Furthermore, the procedure to simulate the nanoscale interaction in our far field microscope is explained in detail.

- Chapter 4 uses the same methodology as before but extends the setup by a grating to measure the fluorescence spectra of single rhodamine molecules next to antennas directly in the widefield image. Here, a coupling dependent dramatic

change in the median spectra of molecules next to different antennas is observed, which depends on the overlap of antenna resonance and molecule emission. The vibronic sideband (0-1 transition) of a single molecule is tuned up to 25x, either by suppressing or enhancing it to show a similar transition rate as that of the main 0-0 transition. Furthermore, characteristic sharp lines in the fluorescence spectra of the single molecules are observed and identified as surface-enhanced-Raman-Scattering spectra in a slightly modified setup.

- In chapter 5, I use off-axis holography to measure the absolute phase in plasmonic and dielectric particles. A detailed description of the holography setup and the analysis necessary to extract the absolute phase is given. Starting by measuring the phase change of gold nanoantennas of different lengths, we successfully discriminate between gold and dielectric particles by looking at their phases rather than their amplitudes. A new two color detection is employed to distinguish different particles in a single shot image.

- Finally, chapter 6 summarizes the results of presented in this thesis, compares the used techniques to other research works and gives an outlook of possible future experiments that build up on this thesis work, as well as possible applications.

2

Optical antennas and single emitters: properties, fabrication and measurement

In this chapter I revise shortly the properties and the fabrication of the plasmonic nanoantennas used throughout the research in this thesis. I give an overview over the two widefield microscopes and the analysis procedures used in chapters 3 and 4 for the interaction of nanoantenna and molecules and in chapter 5 for the phase extraction of the scattering from different nanoparticles. Furthermore, I will introduce the working principle of the used FDTD simulation software.

This chapter contains information from the publication:
L.Saemisch, M. Liebel and N.F. van Hulst, Isolating strong nanoantenna-molecule interactions by ensemble-level single-molecule detection, *Nanoscale* **12**,3723-3730 (2020)

2.1 Nanoscale interaction of optical antennas and single emitters

An introduction to optical antennas

Photons, and therefore light, are ultimately released by single emitters - like atoms and molecules - through electronic transitions in their systems. The cross-section of single emitters at room temperature is with about $10^{-16} cm^2$ extremely small, while the the typical diffraction limited focus size of a laser beam is in the order of $10^{-9} cm^2$[44]. Therefore only one in 10 million photons will be absorbed by the emitter. To overcome this fundamental problem, optical antennas are employed to improve the coupling of single emitters to far field propagating light.

Optical antennas are the counterpart to conventional radio and microwave antennas in the optical wavelength regime[45–47]. By scaling down the dimensions of the conventional antennas about a million times, optical - or nano - antennas are able to interact with the visible part of the spectrum. By definition, a nanoantenna is able to confine light and convert the localized energy in the near field into radiation to the far field and vice versa, which makes it ideal for light-matter interactions. Since optical antennas henceforth provide an efficient way to in- and out-couple light on the nanometer scale, they are excellent linkers for the interaction of single molecules with light.

Optical antennas are metallic structures of a few tenths to hundreds of nanometers in size. The complex permitivity of the metal has a real part expressing the ability to store energy in the nanoantenna, and an imaginary part responsable for the dissipation of the energy in the nanosystem, usually in form of heat[48,49] - used nowadays in medical applications to e.g destroy cancer cells[50]. In a nanoantenna, incoming light excites localized surface plasmon polaritons (LSPP) at the interface of the metal and the surrounding dielectric[2]. The plasmon is a quasiparticle, quantifying the oscillation in the metal - like a phonon quantifies mechanical vibration. The wavelength of these plasmon polaritons is shorter than the wavelength of the incoming free-space light, hence $\lambda_{SP} << \lambda_0$. This difference is due to strong dispersion of light in the metal when going from radio-frequencies to optical frequencies. On the other hand, the short wavelength of the plasmons allows for a tight confinement of light into sub-diffraction limited volumes, so called *hot spots* of strong light intensity.

Depending on the geometry and material of the nanoantenna, the resonance can be tuned in the visible and near-infrared region of the spectrum. In order to excite an antenna efficiently, the wavelength of the incoming light has to overlap with the antenna resonance. Therefore, for the strongest interaction between a molecule and a nanoantenna, the emitter absorption and emission spectra should ideally overlap

with the nanoantenna resonance. For an emitter placed right in the hotspot of a nanoantenna, its properties will be controlled by the nanoantenna. Among others, the emitter experiences a change of both radiative and non-radiative rate of emitted photons, as well as its polarization and its spectral properties (Figure 2.1).

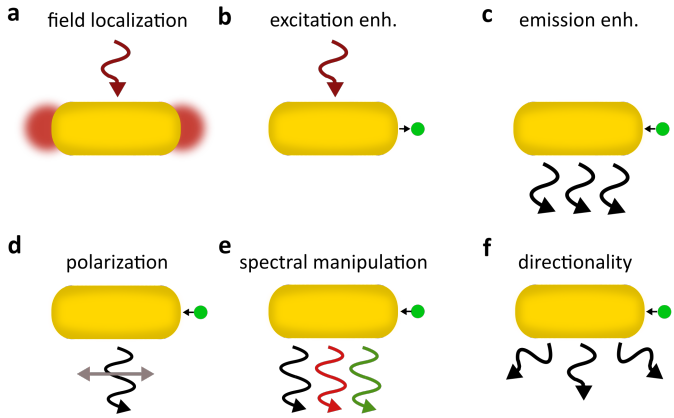

Figure 2.1: Interaction between a molecule and a nanoantenna. Excited LSPPs lead to tightly confined intensity regions (a) where the molecule experiences excitation enhancement (b). The interaction with a nanoantenna also leads to emission enhancement (c), where the emission polarization can be modified (d), as well as the spectral properties (e) and the directionality of the emission (f).

Excitation and emission enhancement

The amount of spontaneous emitted photons per second coming from an emitter, the fluorescence intensity, is a crucial parameter for the detection of single molecules or fluorophores, and the observation and manipulation of their spectral properties. The fluorescence is enhanced by controlling the excitation and emission rates through the interaction with the nanoantenna. The total fluorescence intensity I_{tot} of an emitter can be described as:

$$I_{tot} \propto \eta \Gamma_{ex} \tag{2.1}$$

Here, Γ_{ex} is the excitation rate, which is proportional to the dipole transition d of the emitter, and the local electric field E, thus $\Gamma_{ex} \propto |E \cdot d|^2$. By confining the incoming radiation into sub-diffraction limited volumes, the antenna enhances the local field E, which results in a excitation enhancement of the emitter.

The emission enhancement is described through the quantum efficiency $\eta = k_{rad}/(k_{rad} + k_{non-rad})$, which corresponds to the fraction of light that is radiated instead of being lost through non-radiative processes. Here, k_{rad} and $k_{non-rad}$ are the radiative and non-radiative rates of an emitter close to the antenna, respectively. The magnitude

of the radiative rate enhancement depends on the intrinsic quantum efficiency, η_0, of the emitter far from the antenna. The nanoantenna increases the intrinsic radiative rate of the emitter by the Purcell factor P which leads to an increase in the quantum efficiency and therefore in the amount of fluorescence. However, if an emitter is placed too close to the antenna non-radiative processes take over, as part of the emitters radiation will be transferred to the metal and dissipated into heat resulting in a quenching of fluorescence.

If the emitter has a low intrinsic quantum efficiency η_0, the antenna can enhance its fluorescence significantly by boosting its radiative rate. However, for an emitter with η_0 close to unity, the quantum efficiency can only decrease and fluorescence intensity enhancement can only be a achieved through excitation enhancement.

The half-wave dipole antenna: Resonance and phase change

The most commonly used antenna is the half-wave dipole antenna, which is employed throughout this thesis in the shape of a metal nanorod or a spherical nanoparticle. Apart from the half-wave-dipole, many other higher order modes are possible and depicted in Figure 2.2a for the example of a nanorod. Upon excitation of the LSPP in the nanorod, i.e. a bound wave in the metallic structure, the wave travels along the nanorod and is reflected at its ends, such that a resonant cavity mode is formed. These resonances have a simple relation with the length of a nanrod, and occur when the nanorod length is close to a multiple of half the plasmon wavelength λ_{SP}. While the first resonance is called a half-wave dipole nanoantenna mode, the consecutive resonances exhibit an increasing number of oscillations in the near field of the nanorod, seen in Figure 2.2a for the first three orders.

Figure 2.2b shows typical extinction cross-sections (added emission and absorption cross-section) for four different gold nanorods, indicating the wavelength dependent changes with a maximum at a given resonance wavelength. The increase in absolute value of the maximal cross-section indicates that gold works more effective when going to the near-infrared region of since the dimensions of the rod increase and it therefore becomes a stronger scatterer.

Metallic nanoantennas are lossy, which results in a broad resonance spectrum of several tenths to hundreds of nanometer in wavelength. At the same time, the bandwidths of the resonances show the region of frequencies, in which the nanorod is able to exhibit oscillations and interacts most strongly with the incoming light. While the resonance of a plasmonic particle has a lorenzian shape, the phase change of the light scattered off the particle changes from maximum to minimum, see Figure 2.3. The particle behaves essentially like an harmonic oscillator, changing from a difference of

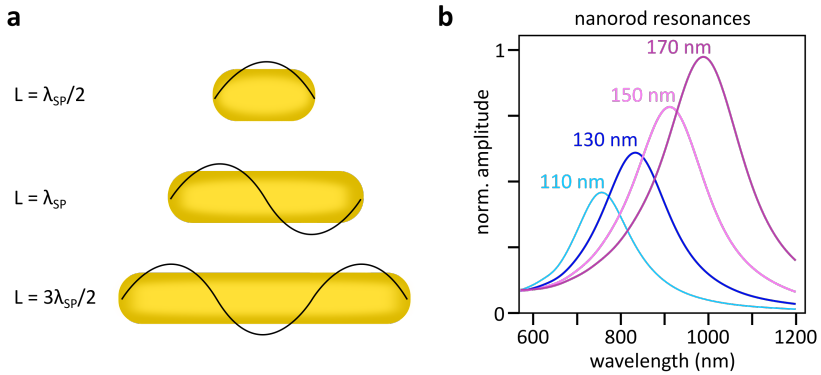

Figure 2.2: Nanorod modes and resonances. a) Intuitive picture of how to understand the resonances of a nanoantenna, where the excited plasmon-wave travels along the nanorod and is being reflected at the ends. Pictured are the first three order modes, but only the first, the dipole antenna, is considered in this thesis. b) Simulated extinction (absorption+scattering) cross-sections of four nanorods of increasing length, where the maximum (hence, the resonance wavelength) shifts to the red part of the spectrum.

π in phase with respect to the incoming light to a phase difference of zero. Here, for small driving frequencies ν ($\nu < \nu_{res}$), the restoring force of the oscillator is large, so the phase difference between external force and the oscillator position is small. At the resonance frequency, the restoring force and inertia caused by the force of the driving field are equal. For frequencies larger than the resonance frequency, the inertia dominates and the restoring force can no longer keep up with the change of movement initiated by the driving field, which leads to a phase difference of π between scattered and incoming light field.

The amplitude and phase behavior differ significantly for a nanoresonator, while being clearly correlated. At the frequency of the maximum amplitude the phase experiences the steepest slope, hence the largest change in value. Consequently, the phase is more sensitive to small changes in a nanoparticle and its environment than the intensity. This increased sensitivity of phase over amplitude is widely used in different detection schemes for biosensing, nanoplasmonics and for material science[42,43].

Nanoscale interaction: polarization and spectral control

The nanoantenna is able to control the polarization of the emitted light in the near and far-field[51,52], due to its specific orientation and the strong dipole oscillator strength. If an emitter with an intrinsic weak dipole moment couples to a nanoantenna, the emission will be dominated by the one of the strong dipole - hence the antenna mode emission pattern.

A nanoantenna can also shape the emission spectrum of a molecule[37–39,53]. The

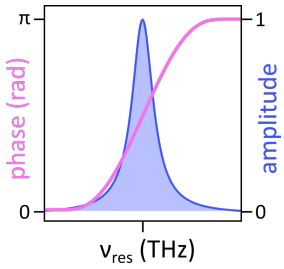

Figure 2.3: Schematic phase and amplitude change of a plasmonic nanoparticle as a function of excitation frequency.

resulting spectrum depends on the resonance overlap of the respective resonances of emitter and nanoantenna. Here, the various transition rates in the emitter are modified by coupling to the local density of states (LDOS) of the nanoantenna, which indicates the relative importance of the nanoantenna-modes an emitter can couple to[54–57]. We can differentiate between the spatial and spectral LDOS, where the former indicates at what position the emitter will feel the maximal LDOS (e.g in the antenna hot spot) and the latter determines the frequency range mostly influenced by the LDOS.

Why single emitters

Apart from the fundamental challenge (and the obvious satisfaction) of being able to control and to manipulate the interaction of a single emitter with a nanoantenna, there are various reasons why single emitters are preferred to an ensemble of molecules next to an optical antenna.

A single molecule is a vectorial point detector. As an example, in scanning-probe experiments single emitters are utilized because of their vectorial field propiertes that would not show in bulk concentration, which can be mapped by a scanning nanoantenna. Generally, the values obtained in ensemble measurements for fluorescence intensities, lifetimes, spectra and coupling strengths are averages and do not reflect on the interaction of a single emitter with a nanostructure. This can be due to different positions and orientations of emitters next to an optical antenna in bulk measurements, as well as the intrinsic heterogenity of single emitters of the same species[16]; there is not such a thing as *the* lifetime and *the* fluorescence spectrum of a species, as every single molecule shows slightly different values for the same property.

This is the crucial reason why single molecule experiments are of utmost importance to reveal the full distribution of a given property and to understand nanoscale interactions of optical antennas and emitters, where rare special cases are not averaged out, but show in full contrast.

2.2 Fabrication of optical antennas

Optical antennas are made of metal, most common silver, gold and aluminum. Silver and aluminum perform better on the blue side of the spectrum, while aluminum is more lossy than silver. Silver oxidizes fast during the fabrication process and storage, and is therefore often not the preferred nanoantenna material. Gold on the other hand is most efficient in the red and near-infrared, and more handy when it comes to fabrication. Although I have fabricated antennas with all three metals, I focus in the following on the fabrication of gold antennas since these are the ones used for the experiments in the next chapters, as we work with red to infra-red emitting molecules and laser excitation wavelengths. Example pictures taken with a scanning electron microscope (SEM) of nanoantennas of different materials, as well as silver oxidation processes are presented in Figure 2.4.

The rod nanoantennas are fabricated using electron beam (e-beam) lithography. The two common processes are called positive and negative resist lithography and are outlined in Figure 2.5a and b, respectively.

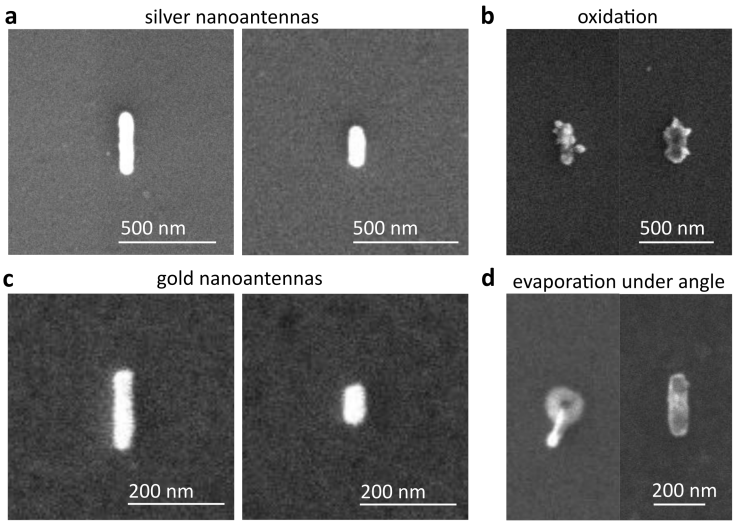

Figure 2.4: SEM images of different nanoantennas. a) Two examples of silver nanoantennas and how their shape generally changes due to oxidation after two weeks (b). c) Examples of gold nanoantennas. d) SEM images of a gold disc (left) and a nanoantenna (right) after lift-off, when beforehand evaporating gold with an angle between source and sample.

For the positive resist lithography process, we evaporate a 7nm indium-tin-oxide layer (ITO) on top of a cleaned glass substrate of thickness 0.17mm. The coated glass is subsequently baked at 350°C for about 5 minutes, which causes the ITO to absorb

sufficient oxygen to turn transparent. The reason for using ITO is two-fold: First, it acts as a adhesion layer for the gold evaporated on top and second, as it is conductive it removes excess charge during the e-beam lithography process.

Subsequently, the positive resist polymethyl methacrylate (PMMA) is spincoated on top to form a roughly 180nm thick layer, which is baked at 150°C to harden. During the e-beam lithography process, the electrons destroy the PMMA at the antenna positions, and the subsequent development process (solvent of MIBK:IPA) removes these exposed areas. We now evaporate a 50nm gold layer on top of the sample - here it is important to place the sample directly above the gold source to avoid an angle in the evaporation, which can lead to slight irregularities in the shape of the nanostructures (Figure 2.4d). After evaporation, the excess gold is removed during the lift off process, where the sample is placed in acetone at 50°C for about three hours.

Compared to the positive resist process, the negative resist lithography process (see Figure 2.5b) has the advantage of being faster and not leaving a conductive layer behind, which could potentially result in the quenching of molecules placed on top of the antennas. On the other hand, the missing conductive layer prevents us from looking at the structures in the scanning electron microscope. For the negative lithography process, we evaporate 5nm titanium layer, followed by a 50nm gold layer. The negative resist (ARN 7500) is subsequently spincoated on top of the sample. Exposing the negative resist to the electrons, its polymeres become crosslinked and the following developing process cannot dissolve these crosslinked parts. We then etch the sample with helium ions that remove everything but the antenna structures from the sample. A subsequent oxygen-cleaning process oxidizes the titanium and cleans the sample.

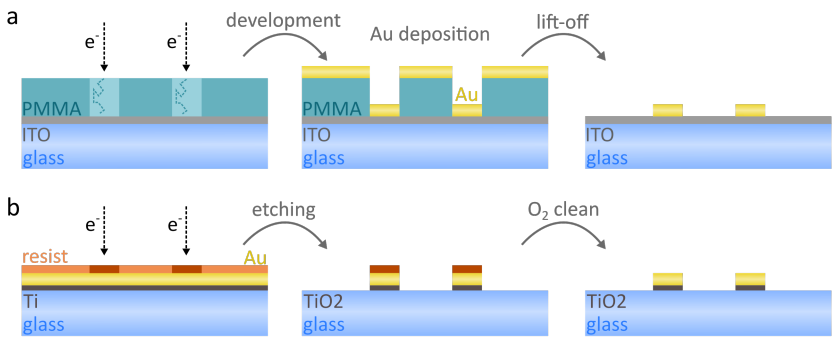

Figure 2.5: Nanoantenna fabrication process for (a) positive and (b) negative resist lithography.

Although the negative resist lithography process is faster, I have tried to opt for the

positive resist lithography process as it is easier to control and the nanorods generally have a better shape. However, the experiments in chapter 3 were performed using nanorods fabricated with negative lithography, since the interaction of nanorod and the used molecules worked better. Here, the ITO layer probably had an influence on the diffusivity and interaction of the molecules with the surface and the nanoantenna.

In conclusion, both processes allow the controlled fabrication of diverse nanoantenna arrays containing different lengths, orientations and fabrication materials.

2.3 Widefield microscopy for fluorescence and scattering

In the upcoming result-chapters, we will measure the nanoscale properties of plasmonic structures and single emitters using different widefield microscopes. An overview is seen in Figure 2.6. Generally, a widefield microscope allows the parallel observation of an entire region of a sample (in our case approximately $400\,\mu m^2$), through the excitation and subsequent imaging of the entire region onto a pixel sensor - such as an EMCCD-camera. This is in contrast to confocal microscopy (and NSOM), where a diffraction limited spot is illuminated and the light is directed onto a photo diode. Here, the entire sample can be imaged through either scanning the sample or the excitation light - the *serial* approach. Although the confocal approach usually has a higher signal-to-noise ratio and a faster detector, it lacks the statistical amount of information the widefield approach offers.

While in chapters 3 and 4 we investigate the nanoscale interaction of single molecules and nanoantennas through monitoring the molecules fluorescence, in chapter 5 we look at the scattered light of different nanostructures to determine their phase via an interferometric setup. The widefield fluorescence microscope is described in detail in the following, while the interferometric microscope will be introduced, but the in-depth explanation will follow in the respective chapter 5.

2.3.1 Widefield-fluorescence-localization microscopy

Chapters 3 and 4 explore the interaction of nanoantennas and single molecules, using a widefield-fluorescence super resolution microscope.

The idea is to let molecules freely diffuse in solution (Figure 2.7a), such that they can stochastically probe an array of immobilised plasmonic nanoantennas (Figure 2.7b). Here, the entire near field is probed as long as sufficient number of single-molecule events, alongside their positions and their spectra are obtained. Experimentally, we

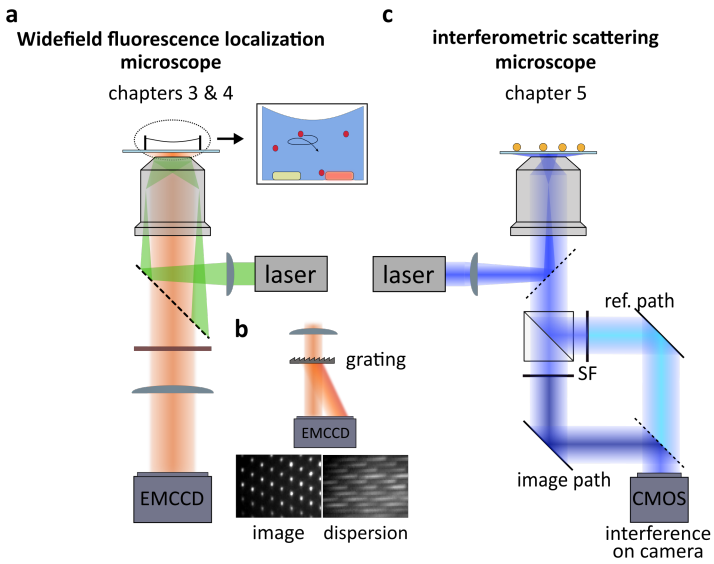

Figure 2.6: The two different widefield microscopes used in the following result chapters. a) Widefield fluorescence localization microscope, where the molecules fluorescence is detected on an EMCCD camera. b) A grating disperses the fluorescence to simultaneously image spectra and localizations. c) Simplified sketch of the interferometric scattering microscope, where the scattering from different nanoparticles alongside the laser backreflection at the samples surface is collected. The collected light is spatially separated and filtered by two spatial filters (SF) into image (dark blue) and reference path (light blue), respectively, to interfere on the camera and enable phase extraction.

simply mount the nanoantennas of interest on top of a widefield microscope and submerge the structures in a solution containing the fluorescent molecules of choice. The widefield setup allows for the simultaneous probing by freely diffusing molecules of about a hundred of nanoantennas of different lengths (resonances) and different orientations - all imaged simultaneously. Here, we ensure the occurence of sufficient identical antennas for statistics. Over the course of a few hours, thousands or millions of fluorescence encounters are recorded (Figure 2.7c)[58], revealing different nanoscale interactions depending on the distance between molecule and nanoantenna, their respective orientations and the resonance overlap.

In the following, I will give a detailed explanation of the setup and the analysis procedure. The nanoantenna sample, the laser excitation wavelength and the used molecules vary depending on the specific experiment.

Set-up

In order to image and study the interaction between single molecules and plasmonic nanoantennas, we rely on a home-built total-internal-reflection (TIRF) microscope

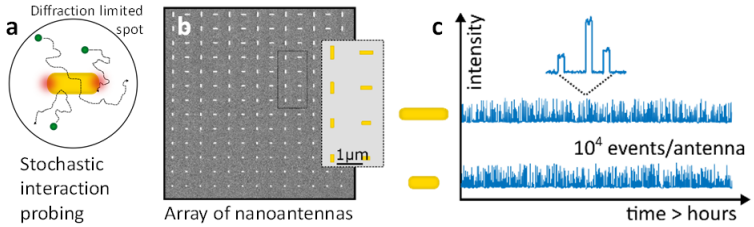

Figure 2.7: Principle of stochastic nanoantenna-molecule interaction mapping with wide-field microscopy. a) Freely diffusing molecules stochastically scan a metallic nanostructure on nanometer scale, below the diffraction limit. b) Typical sample geometry comprised of a large array of individual nanoantennas (SEM image alongside schematic sample lay-out). c) Fluorescence time traces of many single molecule emission events in the vicinity of two different nanoantennas. Over the whole antenna array events are localized in parallel by wide-field imaging.

equipped with an NA 1.49 objective (Olympus APON60x) and an EM-CCD camera (Hamamatsu ImagEM X2) for wide-field detection. A schematic drawing of the setup is seen in Figure 2.6a. We plane-wave illuminate the nanoantenna sample under the critical angle, while focusing the laser beam in the back-focal-plane of the objective to achieve widefield illumination of the sample. The objective lens collects the fluorescence emission, which is separated from the partially reflected excitation light by means of long pass filters. We subsequently image the fluorescence onto the EM-CCD camera at a magnification corresponding to 100 nm/pix. A typical sample consists of electron-beam lithography-fabricated Au nanorod-arrays with varying length and orientation. We add laser dye molecules contained in solution on top of the array-sample to record stochastically occurring fluorescence events. Here, TIRF illumination is crucially important as it allows selective interaction with the individual Au nanorods at the glass/solution interface while limiting the volume contributing to the fluorescence background to the extent of the evanescent field created in the TIRF-geometry, which is approximately 200nm.

To simultaneously record the spectra and localization of molecules next to antennas, we slightly modify the setup by placing a grating (Star Analyser SA-100) in front of the camera to disperse the fluorescence light[59,60], as shown in Figure 2.6b - more detail on this procedure is explained in the next section.

Analysis procedure

Our super-resolution widefield fluorescence microscope allows resolving nanoscale interactions using a method commonly known as "PAINT" technique (Point Accumulation for Imaging in Nanoscale Topography)[58]. Here, the molecule localizations are fit

with Gaussian functions which ultimately allows the reconstruction of a super-resolved image. In the following, I will describe the technique in detail with the example of a proof-of-concept experiment to gauge the overall experimental performance, shown in Figure 2.8.

To this end we fabricate 100x50x58 nm gold nanorods and decrease the apex-to-apex separation between individual rods from 1.5 µm down to 50nm (Figure 2.8a), which is far below the diffraction limit at our detection wavelengths. We use 780nm excitation wavelength and IR895 dye molecules, with a peak fluorescence emission at 895nm. The molecular concentration is adjusted to approximately 10µM leading to typical fluorescence images as shown in Figure 2.8b. Under the experimental conditions described above with an integration time of 50ms we observe a constant fluorescence-background from rapidly diffusing molecules, as well as static photoluminescence from the individual nanorods, which is reminiscent of the SEM-image convolved with the optical point-spread-function (PSF). Furtheremore, we observe stochastically varying single-molecule emission events. These emission events are seen as fluorescence *bursts* on the camera images, mainly consisting of strongly enhanced fluorescence as molecules couple to the nanoantenna. The two static contributions, fluorescence background and antenna photoluminescence, are conveniently isolated by computing a temporal running median-image[61] over batches of 400 images (Figure 2.8c). Subsequent subtraction of the median from the individual 400 video-frames yields essentially background-free images of the stochastically occurring emission-events of the molecules (Figure 2.8d). To correct for the small drift of the sample observed over the course of a few hours during the measurement, we fit the positions of the antenna photoluminescence and subsequently subtract the position difference from the fitted positions of the emission events.

In time, essentially all emission events last less than our integration time of 50ms with only 2% exhibiting fluorescence intensity in consecutive frames. This observation suggests that no, or only very brief, binding of the molecule to the nanostructure takes place, and that the overall "on-period" of individual molecules is considerably shorter than 50ms. This is in good agreement with typical molecule transient times determined by fluorescent correlation spectroscopy measurements, which are on the order of tens to hundreds of microseconds, for a diffraction limited confocal volume, and even smaller for molecules diffusing through antenna hotspots[62,63]. At our molecular concentrations typical wide-field images exhibit only few, spatially well-separated, emission events per image. Thus, we can determine their nanometric positions by fitting a two dimensional

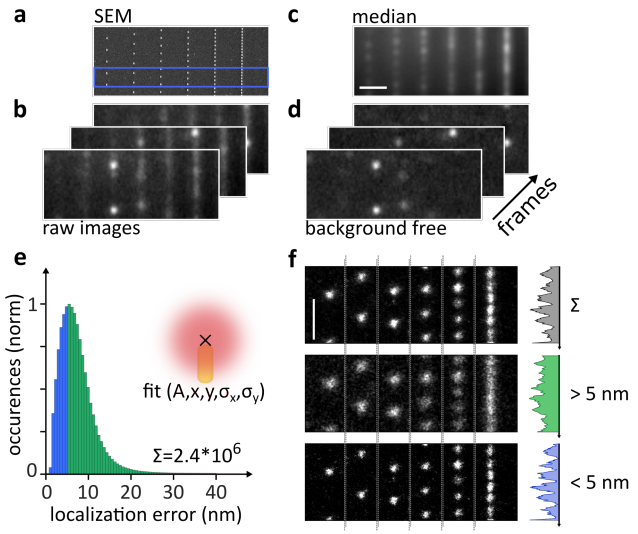

Figure 2.8: Proof of concept: statistical selection allows resolving closely spaced nanostructures. a) SEM image of the studied array of 100x50x58nm nanorods, with apex-to-apex spacing of 800nm, 400nm, 300nm, 200nm, 100nm and 50nm, from left to right. b) Representative fluorescence images as recorded on the camera after adding the n-BuOH solution containing IR895. c) Median background computed from 400 images. d) Background-free fluorescence images obtained by subtracting the median image from the individual frames shown in (b). Scale bar (a)-(d): 1.5 µm. e) Localization error histogram at one standard deviation of all localizations registered in the proof-of-concept experiment. Inset: Schematic of 2D Gaussian fitting of individual emission events, yielding the relevant fitting parameters A (amplitude), x and y (x- and y-position) and the respective localization errors σ_x and σ_y. f) Antenna positions reconstructed from stochastic single-molecule localizations using: All localizations (top), only localizations with a localization error >5nm (center) and <5nm (bottom). The area corresponds to the blue rectangle in a). Scale bar: 500nm.

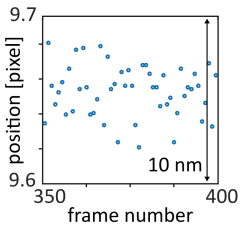

Figure 2.9: Microscope-stability test. X-position of one fluorescent bead during a measurement time of 5 seconds (50 frames), the position is determined by fitting it to a Gaussian. The short-term fluctuations in position are beneath 10nm.

Gaussian function G with amplitude A to the fluorescence event (Figure 2.8e, inset):

$$G(x,y) = \frac{A}{\sqrt{2\pi}} e^{-\frac{x^2}{2\sigma_x^2}+\frac{y^2}{2\sigma_y^2}} \tag{2.2}$$

The fitted positions will consequently have errors σ_x and σ_y in the two fitting directions x and y. The less photons a fluorescence event has, the higher the fitting error. We can henceforth calculate the localization error via $\sqrt{(\sigma_x^2+\sigma_y^2)}$ and plot the results in a histogram, shown in Figure 2.8e. Here, we have obtained $2.4*10^6$ individual single-molecule localizations events over the course of a few-hours of continuous imaging at 20 frames-per-second. Qualitatively, the histogram curve is reminiscent of a Boltzmann distribution with a maximum around 5nm. The ultimate resolution of our microscope is limited by the shot-noise, given by the finite amount of photons emitted by the molecules, and the short-term drift of our microscope stage. Here, we executed a short experiment to observe the influence of the drift on the ultimate resolution by measuring the position change of a sample containing stable fluorescent beads, of which one is shown in Figure 2.9. The short term drift observed in the graph is clearly below 10nm. The standard deviation intrinsically contains the shot noise limit due to the fitting process relying on the number of photons and is hence equivalent to the maximum precision with which we can determine the position of the beads - about 3nm and 4nm in x- and y- direction, respectively. While we use fluorescent dyes in our experiment, which have a lower photon emission than beads, their fluorescence enhancement brings them close to the beads photon emission level.

After having accumulated many dye emission-events we can now - in the spirit of super-resolution-microscopy - use them to reconstruct the underlying antenna structure. We generate super-resolved images by summing area-normalized Gaussians at the fitted positions, with a width corresponding to their localization-error, for all detection-events (PAINT-technique[58]). Figure 2.8f shows the comparison of different reconstructions for the Au nanorod-array using all localization-events (top), localiza-

tion events with large (center) or small (bottom) localization error. A comparison of the SEM image and the reconstructed images shows good agreement between the real and the reconstructed nanorod distances (Figure 2.8a, highlighted area, and Figure 2.8f) indicating that the fluorescence emission probability is greatly enhanced in the vicinity of the Au nanostructures. Indeed, using all detected events allows resolving individual nanorods separated by much less than the diffraction-limit. However, it is advantageous to exclusively rely on the subset of events with small localization errors in order to clearly resolve closely spaced nanorods.

This procedure will be used in the following chapter 3 to image the nanoscale interaction of molecule and nanoantenna. For chapter 4, we rely on finding the emission position of a molecule next to an antenna via a Gaussian fit to identify the corresponding fluorescence spectra on the other side of the camera (see Figure 2.6).

Spectral calibration

A grating allows the simultaneous recording on the camera image of the molecules localizations and their respective spectra as seen in Figure 2.6b. To minimize overlap between the spectra resulting from molecule-nanoantenna interactions, we designed antenna arrays with a vertical offsets between neighboring antennas, shown in an SEM picture in Figure 2.10a. While this layout does not ensure to have zero overlap of spectra on the other side of the camera, it balances the need for statistics with the need for separated spectra. Here, also the concentration of molecules can be adjusted to fit this balance.

The working principle of the spectral calibration done to identify the spectrum for each fluorescence event is seen in Figure 2.10b and c. An exemplary image of an emitting molecule (right) and its spectrum (left) after median subtraction is shown in Figure 2.10b. To assign the correct wavelengths to the spectrum on the left, we have previously employed a calibration method with either a calibration lamp, or a spectral filter with defined cut-off wavelengths and a white-light lamp, with which a sample of disperse nanoparticles is illuminated. Here, the nanoparticles positions alongside the scattered light - consisting of the defined wavelengths of the calibration lamp (or the cut-off wavelengths of the filter) - are imaged. Consequently, we extrapolated for all possible particle positions on the right side of the camera the positions of the defined wavelengths from the calibration source on the left part of the camera. This is schematically seen in Figure 2.10c, where different wavelength positions (I,II and III) are shown as grey dotted lines at a calibrated distance from the molecules position. In the relevant wavelength range for the experiment (visible to the onset of near-infrared) the wavelength dispersion of the calibrated wavelengths can be well approximated by a

linear fit and hence all other wavelengths are extracted easily. The spectral resolution is determined by 3nm (wavelength) per pixel, which provides sufficient resolution to identify spectral evolutions as well as Raman-peaks, while at the same time ensuring a good signal-to-noise ratio of most spectra.

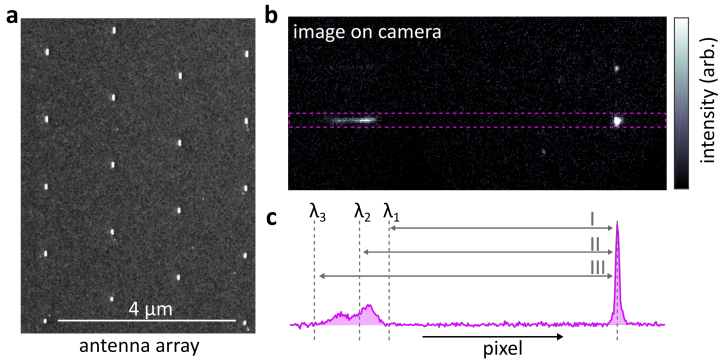

Figure 2.10: Capturing spectra and molecule localization at the same time on the camera. a) SEM picture of the nanorod array used in the spectral experiment. b) Molecule emission captured in one frame, alongside its spectrum on the left (after median subtraction, hence antenna luminescence not visible). c) Sum of columns in the rectangle seen in (b) to see localization (right) and spectrum (left) as a function of pixel. The grey lines schematically depict the asigned wavelengths after calibration procedure. Briefly, after calibration (see text) different calibrated wavelengths ($\lambda_{1,2,3}$) can be assigned to each molecules position at a fixed distance (I,II,III), from which the entire fluorescence spectrum of the molecule is extrapolated. Here, $\lambda_3 > \lambda_2 > \lambda_1$.

2.3.2 Widefield interferometric scattering microscope

In chapter 5 we use an interferometric microscope to extract the phase of the scattered light of different nanostructures. A schematic sketch is seen in Figure 2.6c, while a detailed drawing of the setup and description of the interference process can be found in chapter 5.

Shortly, we illuminate different nanoparticles in a widefield configuration, either in reflection or in transmission, and collect the scattering signal from the particles alongside the reflection or transmission from the sample surface. Consequently, the collected light is split into two paths. Here, the image path contains mainly the scattered light, while the reference path is made up of a plane wave. Both paths are interfered under a certain angle on the camera. This configuration is known as off-axis holography.

The intensity signal resulting from the interference of reference and image path on the camera is seen in Figure 2.11a, for a sample of gold nanoparticles. The intensity image on the camera contains the amplitude squared terms of the reference and the

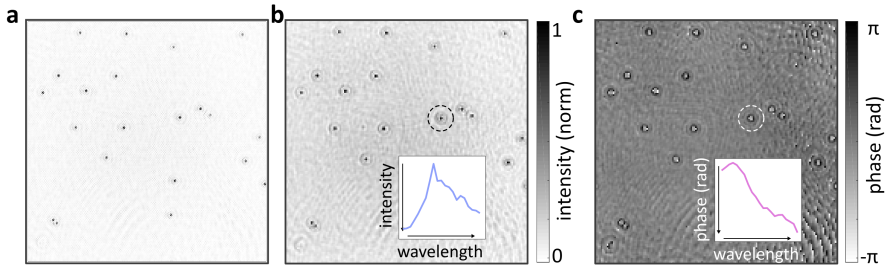

Figure 2.11: Exemplary results obtained using the widefield interferometric scattering microscope. (a) Intensity image as seen on the camera, from which the interference term of image and reference path can be isolated to extract only the intensity image (b) and the phase image (c) of the nanoparticles. The insets show an exemplary intensity and phase spectral-response curve for one circled particle.

scattered light (called "DC"-terms), as well as their interference terms ("AC" terms). Only the interference terms give access to the phase of the scattered light, and our off-axis holographic setup allows to isolate these terms in the subsequent Fourier transform analysis process. The result is a complex image, from which the intensity of the particles and their phase is extracted, seen in Figure 2.11b and c, respectively. We record the interference images at different wavelengths, using a tunable white light laser source, to get the wavelength dependent phase and amplitude result of all particles in the image (insets in Figure 2.11b and c).

2.4 Finite-difference time domain (FDTD) simulations

In all chapters, we employ finite-difference time domain (FDTD) simulations to identify the correct antenna dimensions for a specific resonance, to determine the resonance of already fabricated antennas and to do an extensive analysis of the super-resolved interaction of molecule and nanoantenna. In this section, I will shortly outline the working principle of the software used, *FDTD-solutions* (Lumerical Inc.).

The FDTD solver relies on solving the time-dependent Maxwell equations at many points in the simulation body, which specific monitors can record. As seen in Figure 2.12, the simulation body is a reconstruction of the sample used in the experiments, consisting of all used materials, from the glass coverslide to the ITO/Ti-layer up to the surrounding medium and the dimensions of the nanostructure.

In the case of the gold nanoantenna, we employ rounded edges and corners corresponding to real antenna dimensions after fabrication, as slight variances in these cause the resonance to shift a few tenth of nanometers. Consecutively, we can define

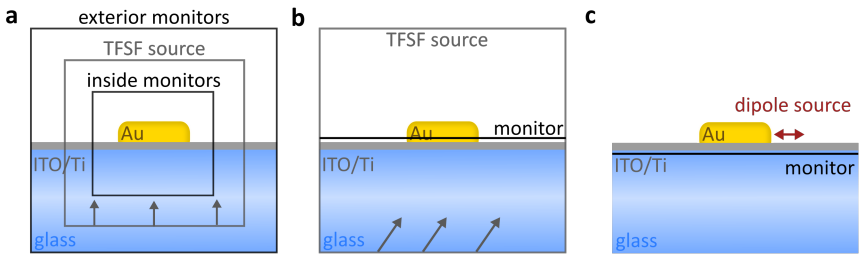

Figure 2.12: Different FDTD-simulation configurations. a) Scheme to simulate the resonance of a gold nanoantenna using the TFSF source. b) Scheme to extract the excitation field around the nanoantenna, while it is excited with a tilted wavefront, mimicking a total-internal-reflection configuration. c) The dipole source acts as a molecules emission next to an antenna recorded by the monitor.

a certain *excitation* source, which in the case of simulating the scattering resonance of our structures is the total-field-scattered-field source (TFSF) (Figure 2.12a). The TFSF source is a closed box which is smaller than the entire simulation body and injects a plane wave from one of its surfaces. At the same time, it subtracts the light that exits the box without interacting with the sample, leaving only the scattered signal. To extract the absorption and scattering spectrum of a nanoantenna, we employ a set of two boxes of planar power monitors, which are placed inside and outside of the source as seen in Figure 2.12a. While the outer monitor collects the scattering signal only, the inner monitor collects a combination of scattered signal and transmitted/injected source intensity, which allows to calculate the amount of absorption of the injected light. This "amount" is characterized by the absorption cross-section of the nanoantenna. The sum of absorption and scattering cross-section makes up the extinction cross-section; an example for the simulation of extinction cross-sections for four different nanoantennas at different wavelengths is shown in Figure 2.2b.

Furthermore, we can also extract the excitation field around a nanoantenna by placing a monitor at the desired height (Figure 2.12b). In order to mimic a molecule next to a nanoantenna and study the nanoscale interaction, one places a dipole source at the molecules position and records the signal with a monitor. This is used in the following chapter to simulate the nanoscale interaction.

2.5 Conclusion

This chapter has introduced the necessary knowledge and methods to understand the research presented in the upcoming three chapters. I have given an introduction to the basic working principles of optical antennas and their fabrication, as well as their inter-

action with single emitters. The simulation procedure for different antenna properties with the FDTD solver has been outlined. Furthermore, I introduced the two wide-field microscopes used in this research work, to measure the nanoscale interaction of molecules and nanoantennas (chapters 3 and 4) and the phase change in nanoparticles (chapter 5).

3

Isolating nanoantenna-molecule interactions by statistical data analysis

In this chapter, I will study the nanoscale interaction between molecules and nanoantennas on the ensemble level.

Traditionally, the nanoscale interaction between single photon emitters and plasmonic nanostructures is studied by relying on deterministic, near-perfect, nanoscale-control, either top-down or bottom-up. However, these approaches are ultra-low throughput thus rendering systematic studies difficult and time-consuming. Here, we show a highly parallelized far-field tactic, combining multiplexed super-resolution fluorescence localization microscopy and data-driven statistical analysis, to study near-field interactions between gold nanorods and single molecules, even at bulk concentrations. We demonstrate that ensemble-level single molecule detection allows separating individual emitters according to their coupling strength with tailored gold nanoantennas, which ultimately permits the reconstruction of super-resolved 2D interaction maps around individual nanoantennas.

This chapter is based on the following publication:
L.Saemisch, M. Liebel and N.F. van Hulst, Isolating strong nanoantenna-molecule interactions by ensemble-level single-molecule detection, *Nanoscale* **12**,3723-3730 (2020)

3.1 Introduction

The advent of super-resolution techniques has revolutionised fluorescence microscopy over the past decades[24–27]. While the field of biology has dramatically benefited from the possibility to study structures with super-resolution microscopy (SRM)[64–66], also the nanophotonic research has started implementing SRM-methodologies, but the potential of large-data-driven approaches remains mostly unexplored.

There have been numerous studies on the super-resolved interaction of molecules with different plasmonic structures and surface[28–36]. Most of these works show discrepancies between the true single-emitter position and its super-localized position, which is determined in the far field through a microscope system. Given that far-field localizations are strongly dependent on the orientation of an emitter[67], the discrepancies in position come as no surprise especially when considering the case of weak emitters placed in proximity to a resonant plasmonic structure with a strong dipole-moment[35,36]. Despite these imaging problems, the combination of plasmonics with SRM holds great promise for systematically studying the interaction between individual nanostructures and fluorophores. While near-field-scanning-antenna approaches offer ultimate control to study the interaction of molecule and antenna[20–23], the experimental complexity and serial scanning of this approach dramatically limits its applicability and throughput. Less complexity is offered by the DNA-PAINT method, in which metallic nanostructures are functionalized with DNA-strands that are labelled with fluorophores[68–71]. While these fluorophores can probe the field around the nanostructure at different engineered positions, this technique is limited by the number of strands and it is therefore not possible to probe the entire field in one experiment.

In this chapter, I will present a less complex and high-throughput experiment to study molecule-nanoantenna interactions. As outlined in chapter 2, freely diffusing molecules simultaneously probe hundreds of individual nanostructures at all positions. Statistical data analysis of millions of localization events of single molecules interacting with nanorods of different lengths, and therefore different resonances, allows to study the coupling and the dependence on the spectral overlap of nanorod resonance and molecule emission. Moreover, I show that rigorous statistical analysis of the localization error as well as the degree of linear polarization (DOLP) gives direct access to the molecule-nanostructure interaction strength, allowing the reconstruction of superesolved 2D interaction maps.

The idea behind the experiment: What does a far-field observer see when molecules interact with different nanoantennas in the near-field?

When a molecule diffuses around short gold nanoantennas with their resonances shifted to the blue with respect to the molecule´s emission spectrum (Figure 3.1a, top), the fluorescence photons emitted by the molecule will interact only weakly with the nanoantenna due to their resonance mismatch. In this case, the apparent fluorescence will come mainly from the excitation hotspot regions. On the other hand, if we take a nanoantenna that spectrally overlaps with the molecule´s emission, the photons do interact strongly with the nanoantenna. In that case, a far-field observer would see the emission coming from the phase center of the dipole-nanoantenna (Figure 3.1a, center) acting as the strong, dominant dipole emitter, while an observer in the near field would probably see the antenna mode of the nanorod being probed and driven by the fluorescent molecule. Additionally, if the molecule couples to the nanoantenna, its degree of linear polarization (DOLP) of the fluorescence changes from the intrinsic emission dipole orientation of the molecule to the direction aligned with the long axis of the dipole nanoantenna (3.1b).

In the following section, I will present the results we achieved, with both confirmation and differences compared to our expectations.

3.2 Nanoscale interaction of a molecule and a nanoantenna

3.2.1 The crucial role of localization error and polarization

We gauge our setup as outlined in detail in chapter 2. To study the nanoscale interaction for different overlaps of the molecules and nanoantenna resonances, we decide to use the laser dye IR895, whose emission is strongly redshifted with a peak at 920nm. Consequently, we use nanoantennas made of gold since they are most effective in the near-infrared part of the spectrum and overlay nicely with the molecules spectrum.

The analysis procedure is the same as presented in chapter 2. More specifically, we fabricate gold nanorod-arrays with antenna length ranging from 95nm to 145nm and a width of 58nm, using the negative lithography process. Furthermore, we equip our detection channel with a Wollaston prism to allow the detection of both polarizations simultaneously, parallel and perpendicular with respect to the long antenna-axis.

Figure 3.2a shows a super resolved interaction map of molecule and nanoantenna obtained for excitation and detection along the long axis of the nanorod (s-polarization). The reconstructions rely on all detected fluorescence events and, furthermore, averag-

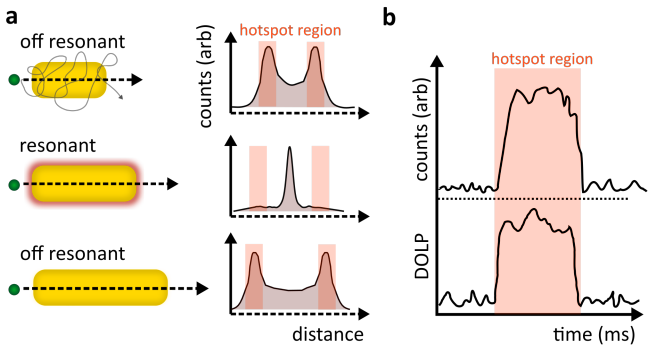

Figure 3.1: Idea behind the experiment. a) Depending on the resonant overlap of the molecule and the nanoantenna, we expect to see different nanoscale intensity maps of the fluorescence emission next to the structures - observed in the far field. For the off-resonant case where the molecules emission and antenna resonance do not spectrally overlap, the molecule probes the tightly confined electric-field hotspots at the nanoantenna apexes (hotspot region) and emits at the probed position (top and bottom case). In the resonant case however (center), the molecule interacts with the antenna and the emission is dominated by the stronger dipole, the nanoantenna, resulting in an apparent emission from the center of the nanoantenna. b) DOLP- time trace for a molecule probing different regions around a nanoantenna. In the hotspot region of the nanoantenna, where the molecule interacts stronger, the DOLP will be mostly aligned along the long axis of the nanoantenna.

ing 12 individual antennas for each length to reduce the effect of possible nanofabrication-imperfections. Qualitatively, these interaction maps look identical albeit a gradual increase in size with increasing nanorod length. Importantly, all reconstructed areas are smaller than the nanorod itself, as expected for experiments performed in the vicinity of resonant metallic nanostructures which are known to displace the molecular emission in the far-field[33,35,36].

Based on the absorption and emission spectrum of the employed laser-dye IR895 (Figure 3.2b) with its strongly red-shifted fluorescence band centered around 920nm, we would expect to observe distinct signatures of both excitation- as well as emission-enhancement phenomena due to the presence of the metallic nanostructures and their different resonances[32]. According to FDTD simulations, the fluorescence emission maximum roughly overlaps with the resonance of the 145nm nanorod, whereas the 780nm excitation laser most efficiently interacts with the structures of approximately 110nm in length. Consequently, we would expect well-separated excitation- and emission-enhancement around 110nm and 145nm, respectively, which should manifest themselves in distinctly different antenna-reconstructions. However, none of the anticipated effects is observed in the interaction maps.

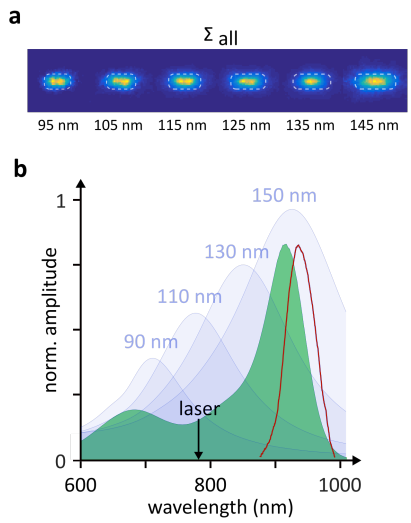

Figure 3.2: a) Antennas with lengths ranging from 95nm to 145nm reconstructed by relying on all detected fluorescence events. b) IR895 absorption (green) and fluorescence (red) spectra in comparison to simulated extinction spectra of Au nanorods of different length (blue).

So far, we only used the localization information of the average of all events. To extract more specific field information, we perform statistical analysis of all localization events. Figure 3.3a shows a correlation between the fluorescence intensity and the localization error of all fitted emission events. We observe a shot-noise like correlation with an, approximate, square-root relation between localization error and fluorescence intensity. This observation indicates that neither strong background intensities nor possible distortions of the point-spread-function (PSF), due to strong molecule-antenna coupling, affect the experimental data, as these effects would result in strong departures from the anticipated behavior. Here, strong background intensities or PSF distortions would give a large localization error while maintaining a high intensity. Therefore, the localization error and the fluorescence intensity contain qualitatively identical information and the thresholding of localization events based on either parameter should, in principle, allow isolation of strongly interacting molecules. However, our previous observations suggest that the IR895 emission events are due to molecules merely diffusing through the antenna hotspots. As a result, localization error, or intensity, based thresholding might be unable to distinguish between transiently bound molecules in a region of medium intensity or even on bare glass, and a molecule diffusing rapidly through the high-field-intensity region of interest, as we would expect to see the same intensity in both cases.

To refine the extraction of the localization events of interest we therefore introduce a

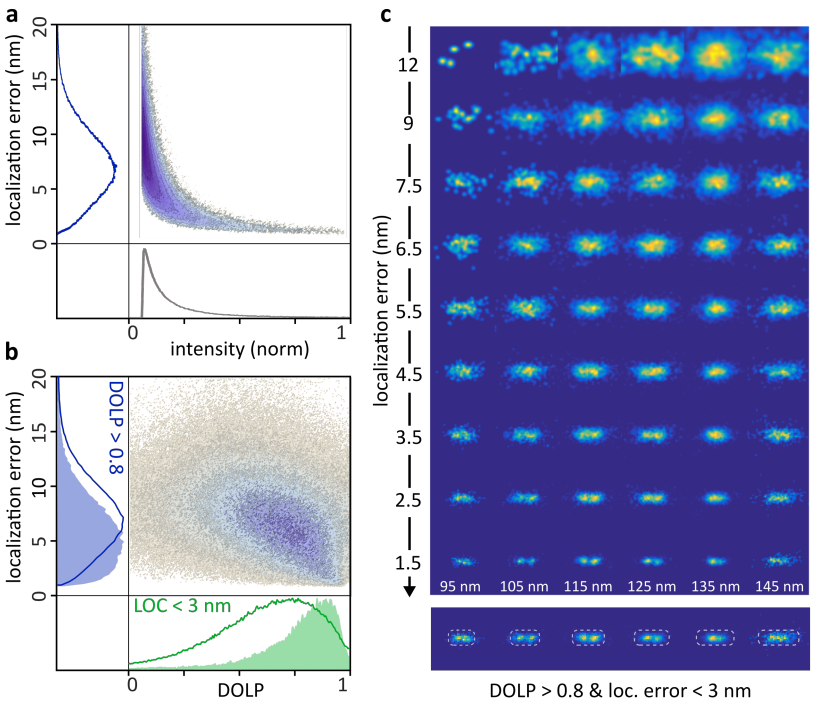

Figure 3.3: Role of statistics for mapping the nanoscale interaction. a) Correlation between emission intensity and localization error for all detected fluorescence events alongside histogram representations. b) Correlation between the DOLP and the localization error alongside histogram representations containing the full data-set (solid line) and the localization histogram for DOLP $>$ 0.8 (blue, filled) and a DOLP histogram for a localization error $<$ 3nm (green, filled). c) Antennas with lengths ranging from 95nm to 145nm reconstructed by relying on data subsets with DOLP $>$ 0.8 and decreasing localization error. Bottom: Final reconstruction with localization errors $<$ 3nm and DOLP $>$ 0.8.

second parameter, the degree of linear polarization (DOLP) computed as DOLP=(Is-Ip)/(Is+Ip) with Is and Ip being the fluorescence intensity of individual molecules detected in the, simultaneously recorded, s- and p-polarized imaging channels, which are parallel and perpendicular with respect to the long antenna axis, respectively. We expect the DOLP to directly report on the antenna-molecule coupling and hence the molecules' position within the enhanced electric field around the nanorod. For molecules in close vicinity to a nanorod, the emission should be strongly polarized along the antenna axis thus resulting in the largest possible DOLP. Figure 3.3b shows a DOLP-localization error correlation graph, which indicates a qualitative correlation between the two values. As expected, we observe a shift towards larger DOLP values when filtering for events with small localization errors, and therefore higher fluorescence intensity. We note that DOLP $>$ 0.8 can be readily obtained in our experiment

as the molecules exhibit near-isotropic emission as they are freely diffusing in n-BuOH with a refractive index of nBuOH=1.4 which is close to the n=1.52 of the substrate. As a result, the commonly observed depolarization for high-NA objectives is far less pronounced[51,72].

Based on the correlation-graphs, we now attempt a refined antenna-reconstruction seen in Figure 3.3c. We keep the DOLP > 0.8 to select molecules that show considerable antenna-coupling and evaluate different localization error intervals. For the most precise localization, we observe a pronounced double-spot pattern with an approximate spot-to-spot separation of 35nm, for shorter antennas, which merges into a single, slightly elongated spot, for longer antennas (Figure 3.3 c, center). As we move towards higher localization errors, the features disappear, even for errors as small as 4.5 nm, which is surprising given the spot-separation of 35nm. Intuitively, we would assume that any super-resolved feature is blurred by the localization error but a mere increase of 4.5-2.5=2.0nm results in complete disappearance of the, previously, clearly resolved double-spots. To rationalize this surprising observation we quantify the deterioration by computing the spread of the localizations around the mean antenna position ($\bar{x}$,$\bar{y}$) as:

$$\frac{\sum_{n=1}^{N} \sqrt{(x-\bar{x})^2 + (y-\bar{y})^2}}{N} \tag{3.1}$$

Here, we observe a dramatic departure from the expected shot-noise-limited like increase (Figure 3.4) with the spread around the antenna mean increasing by 124nm for a localization error increase of 10.5 nm. From a SRM point-of-view, this observation might appear surprising. However, the electric field distribution around a nanoantenna is not a structure with a well-defined, binary shape but rather a function with boundaries that depend on the intensity-enhancement and interaction strength with the molecular probes. A poorly-localized molecule is therefore more likely to be further away from the nanorod than a well-localized one thus increasing the absolute area that is sampled around the antenna. This localization error-based sampling space results in a rapid loss of the high electric-field-intensity information. Based on these observations we attempt the *ideal* antenna intensity reconstruction based on all localization events with a DOLP>0.8 and a localization error <3 nm (Figure 3.3c (bottom)), which shows a gradual transition from a double to a single spot upon varying the antenna resonance.

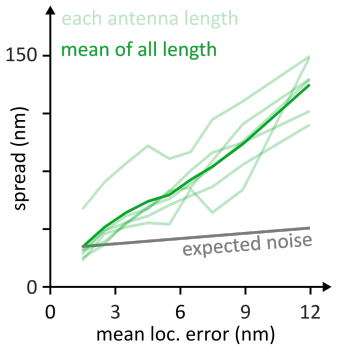

Figure 3.4: Mean localization error dependence of the spread around the mean antenna position for all antenna lengths compared to the expected increase estimated based on shot-noise like localization deterioration.

3.3 Simulating the nanoscale interaction

To rationalize these experimental observations, we perform FDTD simulations using the Lumerical solver, as already introduced in chapter 2. To this end, we start by simulating the radiation patterns of x- and y-oriented dipoles that act as our molecules at different positions around the nanorod, seen in Figure 3.5a. A nearby monitor records the emission of the dipoles next to the nanostructure (Figure 3.5b, see also section 2.4), from which we generate far field images through a fast Fourier transformation (FFT) reflecting our experimental imaging system - which records near-field interaction in the far field.

We employ the FFTs for the x,y and z component of the complex electric field recorded in Figure 3.5b), and subsequently need to account for the finite numerical aperture of our objective. Hence, we set all wavevectors with a larger angle than that of our objective to zero, as shown for the x and y components in Figure 3.5c. We perform an inverse Fourier transformation to leave the far-field frequency space and sum up all three - x,y and z - modified components to get the total intensity image in the far field of a dipole emitter next to a nanoantenna, seen in Figure 3.5d. We consecutively fit the x and y position of the emitters intensity. We determine this *far-field displacement* for 184 dipole positions and two different dipole orientations. Before lastly reconstructing the determined positions in a new image (example for x- and y-dipole displacement is shown in Figure 3.6), we need to account for the excitation enhancement by the close-by nanoantenna. Depending on the near-field intensity in the hotspots at the different dipole-positions, the emitters will experience a distinct enhancement. We therefore calculate the intensity distribution around the nanoantenna in TIRF-configuration at a plane 5nm above the surface, shown in Figure 3.5e. Since its z contribution is minor

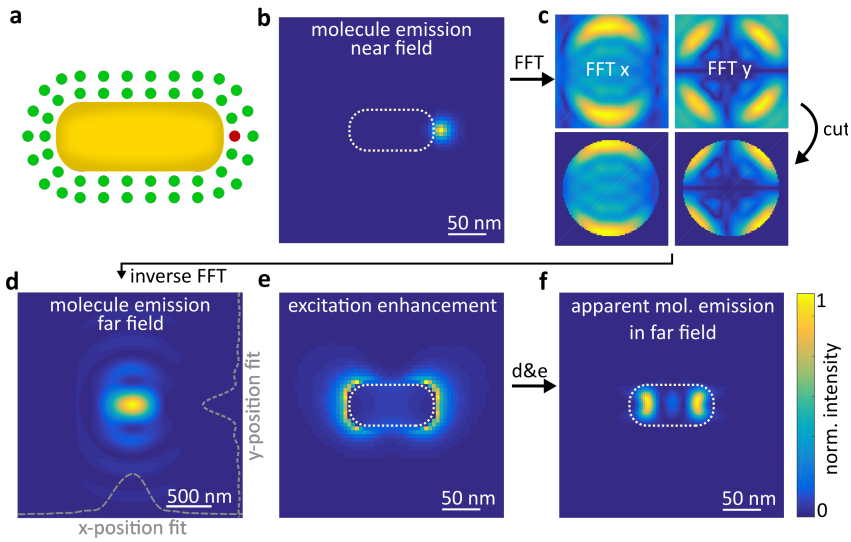

Figure 3.5: Procedure for simulating the nanoscale interaction of antenna and molecule with FDTD software and Matlab-software analysis.a) For every FDTD simulation, a single dipole emitter is placed at a different position with either x- or y-dipole orientation next to the nanoantenna. Part b) shows the collected dipole emission of a power monitor placed at -12nm below the nanostructure, the antenna is schematically drawn as white dotted line. In c) we perform fast Fourier transformations of the x- and y-component of the electric field in b), to subsequently cut the images to account for the finite aperture of our imaging system, before being individually inverse Fourier transformed into real space, shown in d). A subsequent x- and y-position fit of the observed spot is combined with the simulated excitation enhancement of the antenna, e), - recorded at the same height as the molecules in a) were placed (5nm) - to yield the final simulation of the apparent position of the molecules emission in the far field, f).

(below 5%), we only took the x and y components of the excitation field and dipole orientations into account.

The final step consist in combining the emission of each molecular dipole emitter next to the nanoantenna with the amount of excitation that they experience at their respective positions. In order to reconstruct the simulated far-field interaction map, we take the value of excitation intensity in x (y) at the actual position of the x (y) dipole, and plot this number at the fitted position of the dipole (after the far-field-projection and angle-cut). The combined result for all dipole positions is seen in Figure 3.5f. For the reconstruction process we take a pixel size of 2.5 nm and plot the fitted positions as Gaussians with a width of 6nm. The set width is larger than in the experiment to blur the reconstructed fluorescence localizations, since we have a relatively small number of molecules probing the field in the simulation, contrarily to many thousand events in the experiment.

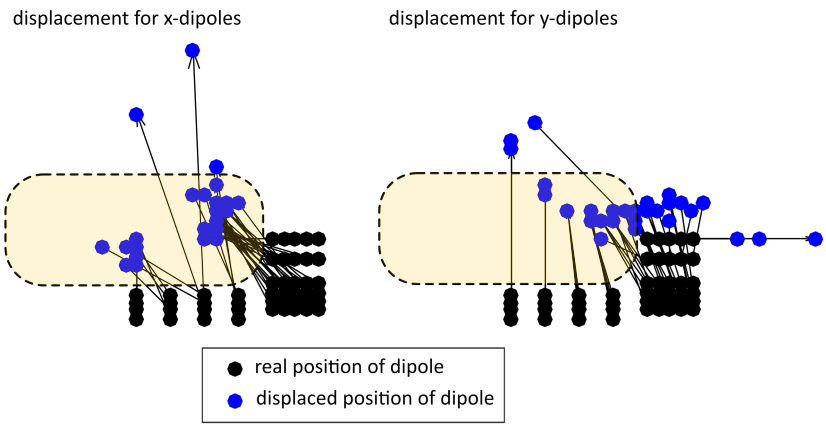

Figure 3.6: Example of simulated x- and y- dipole displacements (left and right, respectively) for a 115nm rod. For symmetry reasons, the dipoles are placed in one quarter only. The arrows indicate the shifts from the real positions (black) to the displaced positions of the molecules (blue), determined after placing them next to the nanorod.

In summary, we obtain a simulated reconstructed image where the intensity of each dipole emitter corresponds to the excitation field intensity of the nanorod at the a emitters' location.

3.4 Comparing simulation and data

Figure 3.7a shows a comparison between the experimentally obtained results for 115nm, 135nm and 145nm long nanorods and the simulation. Here, the three lengths show qualitatively the transition from excitation to emission enhancement. As in the experiment, we observe a the pattern change with most of the fluorescence intensity being localized in the center of the antenna once its resonance overlaps with the molecular emission spectrum, which is in good agreement with previously reported experimental studies and simulations[31,73]. The slight deviations between our experimental data and the simulations are most likely due to the insufficient quality of the experimental data as well as the crude modelling of the antenna-molecule coupling strength. Here, we restrict our model two a single 2D plane, located 5nm above the sample-substrate, of molecule-nanorod interactions rather than the full 3D volume around the antenna. Additionally, we model the ideal shape of the nanorod after fabrication, where surface irregularities and slight deformations are ignored, an ideal scenario that we tried to reproduce by summing a total of 12 individual antennas per length. Especially for excitation wavelengths blue-shifted with respect to an antenna resonance the excitation

enhancement is generally reduced[3,74] thus complicating the experiment considerably, a fact that manifests itself in the reduced data quality of the 135nm and 145nm data as compared to the data obtained with the red-shifted excitation of the 115nm antenna.

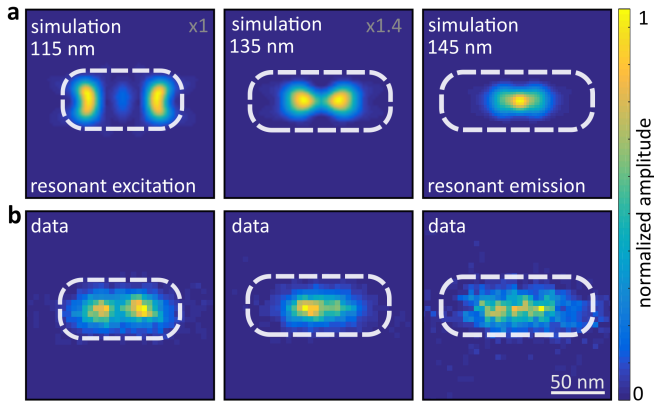

Figure 3.7: Comparison between simulations and experimental observations. (a) Localization maps from FDTD simulations for 115nm, 135nm and 145nm antennas compared to (b) experimental intensity distributions, reconstructed by applying a threshold with localization error $<$ 4nm and DOLP $>$ 0.8.

Double spot and DOLP behavior

In the nanoscale maps for the off-resonant cases which are dominated by excitation enhancement, we observe slightly inwards shifted spots, compared to the actual hotspot locations at the apexes of the dipole antenna. Although molecule and nanoantenna are not strongly interacting in this case, the broadness of the antenna resonance and its stronger oscillation - compared to the molecule - still imply a weak interaction. Therefore, the far field projection of a strong dipole oscillator, the nanorod, and the weakly coupled small dipolar molecule causes the apparent emission from the hotspots at the apex to shift slightly to the center of the stronger nanorod oscillator. The dominant oscillator strength of the nanorod, when driven along its long axis, also forces the molecule to change its dipole orientation, even in the weak, off resonant case. In the following sections we will consider two special cases of the nanoscale interaction with the emitted fluorescence polarized either perpendicular or along the nanorod. The first example shows the mapping of the cross-polarization in detection - the case where the molecular emission does not adapt to the dominant nanoantenna polarization (section 3.5). The second example considers solely the emission enhancement of the molecule, as the excitation occurs purely along the short, non-resonant axis of the nanoantenna, while the emission polarization is solely detected along the long antenna axis (section

3.6).

3.5 Mapping the cross polarization

To conclude the data-driven mapping of molecule-antenna coupling strength we now turn our attention to the molecular events detected with emission polarization perpendicular with respect to the excitation polarization as well as the antenna-resonance axis. Contrary to the coupling case in Figure 3.7, molecular events detected in this "cross-polarization" do not couple to the long axis of the nanoantenna – hence we are able to separate the coupling and non-coupling events around the same nanoantenna. Based on the strong DOLP bias of our experiment (Figure 3.3b) and the unfavorable excitation and emission enhancement of perpendicularly-oriented molecules we expect few emission events with little-to-no intensity in the cross-polarized imaging channel. The large amount of localization events recorded nevertheless allows us to analyze the electric fields governing emission through this channel. Figure 3.8a shows an emission-intensity reconstruction of the 115nm and 125nm nanorods for 12 summed antennas based on approximately 1100 events with a localization error < 7.1 nm and DOLP $<$(-0.4). The reconstructed patterns are both reminiscent of the cloverleaf-like PSFs previously observed as far-field emission patterns of individual emitters positioned above a nanowire[75]. However, our reconstruction is based on post-detection reconstruction, which incorporates Gaussian fitting which necessarily results in a complete loss of PSF shape-information. To rationalize our observation, we simulate the y-component of the electric field present around a nanorod of 125nm length after far-field TIRF-excitation with light polarized along the long axis of the nanorod, seen in Figure 3.8b. The near-perfect agreement between experimentally observed fluorescence localizations and theoretically predicted excitation intensity suggests that we purely probe the y-component of the electric antenna field without any interaction of molecule and nanoantenna. The cloverleaf pattern does not depend on the nanorod length, however the size of the cloverleaf pattern increases (decreases) with increasing (decreasing) nanorod dimensions. Our results confirm the findings obtained by direct near field imaging of the vectorial nanorod fields with a scanning antenna tip[20].

3.6 Excitation parallel to the short axis of the nanoantenna

The complete set of the four possible polarization configurations in our experiment are shown in Figure 3.9 as determined by the two antenna orientations and the Wollaston

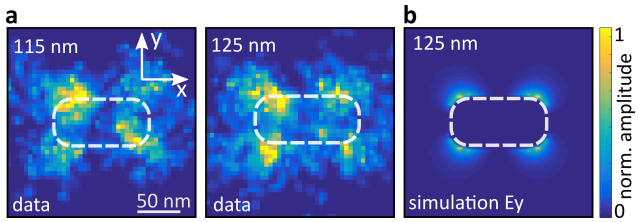

Figure 3.8: Crosspolarization analysis. a) Experimentally reconstructed intensity distribution for cross-polarized localizations with localization error < 7.1 nm and DOLP < -0.4 for 115nm and 125nm antennas, in comparison to (b) a FDTD simulation of the y-component of the electric field around the nanoantenna.

prism imaging perpendicular and parallel polarized light onto the camera. The two orientations of rod antennas on our sample ensure to have the polarization alongside the long axis of one of the two nanoantennas, independent on the sample orientation on the microscope. The polarization of the exciting laser cannot be rotated easily, as we are in TIRF configuration, where one linear polarization leads to a cartwheel-like rotating polarization on the sample.

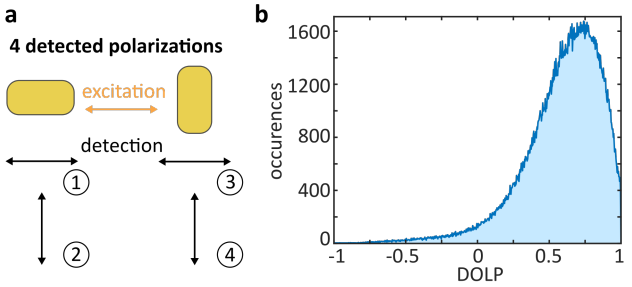

Figure 3.9: Polarization configurations. (a) The four different polarization configurations; (1) excitation and detection along the long axis of the nanorod, (2) excitation along the long axis and detection along the short axis, (3) excitation and detection along the short axis and (4) excitation along the short axis and detection along the long axis. (b) DOLP histogram for all detected events in the experiment.

The DOLP is 1 for configurations ① and ③, while it is -1 for configurations ② and ④. Figure 3.9b (based on Figure 3.3b) shows the histogram of the DOLP values calculated for every detected event. Its distribution around 1 underlines the favorable configuration polarizations ① and ③, where configuration ① is favored due to the excitation alongside the long axis of the nanorod. The analysis so far was based on the polarization configuration ① (section 3.2) and ② (section 3.5), showing a double spot or a cloverleaf structure, respectively, where the excitation is always polarized along the long axis of the nanorod. In this section, we consider configurations ③ and

④, where the excitation occurs along the short axis of the nanoantenna.

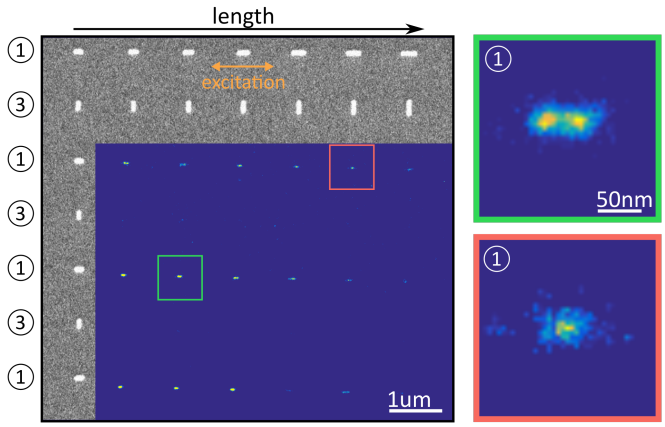

Figure 3.10: EBL-image of the sample, alongside the reconstructed image of detected events in polarization configuration ① and ③, labeled on the left side. The zoom in shows two single antenna reconstructions for two different lengths in polarization configuration ①, as already analyzed in the previous sections.

The reconstruction for configurations ① and ③ is seen in Figure 3.10, where we excite and detect along the horizontal axis (orange arrow) seen in the integrated EBL image of the sample. Here, horizontal antennas resemble polarization configuration ①, while the vertical ones represent configuration ③. The former shows a lot of counts in the reconstructed image - equal to many high intensity emission events detected - with a zoom in on specific antennas showing a clear double spot (short antenna) and single spot (long antenna) behavior. For configuration ③ however, we hardly observe any signal due to the unfavorable excitation and detection alongside the short axis of the nanoantenna.

For polarization configuration ④, with excitation along the short axis and detection along the long axis, we observe sufficient events to reconstruct an image (Figure 3.11). However, we are not able to observe any transition from a double to a single spot pattern, but rather only a displacement to the center of the nanorod. In this configuration, we can disregard the weak excitation enhancement where no hotspots are present and, most probably, mainly observe the emission of the molecule through the antenna - solely resulting in a displacement directed to the center of the nanorod.

3.7 Conclusion and outlook

In summary, we constructed a wide-field TIRF microscope and employed arrays of nanoantennas with increasing length that resonantly interact with individual emit-

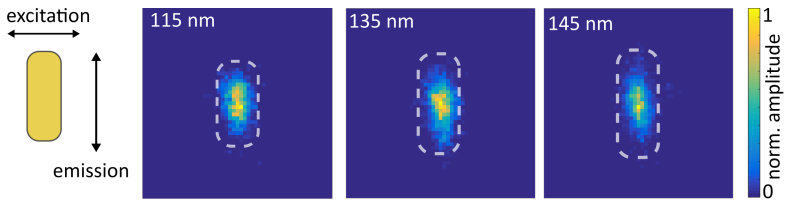

Figure 3.11: Reconstructed maps for three different nanoantennas in polarization configuration ④.

ters at both excitation and emission frequencies. Depending on the antenna length, either emission- or excitation-induced effects resulted in remarkable changes in the observed super-resolved intensity reconstructions. Instead of concentrating on these now well- understood, and widely studied, discrepancies between expected and measured electric field distributions, we instead emphasize the true strength of wide-field super-resolution mapping of plasmonic structures: the possibility to perform highly-parallelized high-throughput experiments in combination with thorough statistical analysis. While most of nano-plasmonics relies on point-scanning, or confocal, observations, which are intrinsically throughput-limited, the "PAINT"-technique yields millions of single-molecule observations while, simultaneously, being considerably easier to experimentally implement. As a result, intensity and polarization measurements allow us to isolate a small subset of strongly-coupled single molecules from an enormous number of less-coupled emitters and background, purely based on statistical analysis that relies on physically meaningful expectations. Based on this analysis we resolved the expected double-spot excitation enhancement pattern present around the antenna-apexes, which would have remained unresolved if statistical filtering would not have been applied.

Furthermore, we were able to resolve the Ey-component of the electric field in a cross-polarization analysis, by isolating the few events that did not couple to the long axis of the nanoantenna. We also analyzed the excitation along the short axis of the nanorod, where the detection along the short nanoantenna axis does not give any signal, while the detection along the long axis shows solely emission displacement.

Our approach highlights that single-molecule based approaches are extremely powerful when conducted at ensemble-level detection levels. Here, rarely occurring events, such as the strong coupling of an individual molecule to a plasmonic structure, can be identified with statistical significance. Importantly, such observations are impossible with ensemble based techniques and would have most likely been discarded as artefacts in traditional single emitter experiments, which often draw conclusions based on a few tens of observations. Ensemble-level single molecule spectroscopy eliminates

these problems and allows confident identification and study of physical phenomena based on rigorous statistical analysis.

Overall, this is a robust method for finding specific and rare cases of stronger interaction out of an ensemble of many random occurrences. We can imagine an implementation e.g. in a bioanalytical laboratory, where a simple post-processing thresholding program will reveal specific interactions. Compared to the serial near-field scanning antenna approach, our parallel experiment is considerably easier to implement and execute. In the near future, our method might be applied for subwavelength sensing in future mini CMOS cameras. Finally, the occurrence of light re-localization provides an interesting concept for light concentration applications in general, such as in solar light harvesting.

4

Control of vibronic transition rates by nanoantennas

In this chapter, I explore the extreme spectral shaping of single molecules next to plasmonic nanoantennas.

Plasmonic nanostructures dramatically alter the radiative and non-radiative properties of single molecules in their vicinity. This coupling induced change in decay channels selectively enhances specific vibronic transitions, which can enable plasmonic control of molecular reactivity. Here, we report coupling dependent spectral emission shaping of single Rhodamine 800 molecules in the vicinity of plasmonic gold nanorods. We show that the relative vibronic transition rates of the first two vibronic transitions of the spontaneous emission spectrum can be tuned in the weak coupling regime, by approximately 25-fold, on the single molecule level. Furthermore, our setup permits seeing many surfaced-enhanced-raman-scattering signals of single molecules next to resonant nanorods.

This chapter is based on the following publication:
L.Saemisch, M. Liebel and N.F. van Hulst, Control of vibronic transition rates by resonant single-molecule-nanoantenna coupling, *Nano Lett.* **20**, 4537-4542 (2020)

4.1 Introduction

In the past years, plasmonic structures are increasingly being used for manipulating and controlling chemical reactions[76]. The combination of nanometric control with the well-known catalytic activity of noble metals allows performing chemical reactions in defined reaction volumes and enables studying chemical reactivity, even on the single-catalyst level[69,77,78]. Beyond understanding mechanistic details, precisely defined reactant-nanostructure interactions should allow the active control of chemical reactions[79]. Single emitters in the vicinity of plasmonic nanostructures can be regarded as a test-case for such active interaction control, where the emitters experience a dramatic change in their radiative and non-radiative properties[15,80–82], which impact the overall emission spectrum through the selective control of individual vibronic spontaneous emission rates[57,83]. Surprisingly, the spectral shaping induced by the interaction with nanostructures has remained largely unexplored and most of our understanding is based on ensemble-based experiments[37,38,53] where it is difficult to distinguish overall spectral shifts from the, potentially, dominating contribution of individual, highly-coupled, emitters.

Recently, Lee et al. performed single-molecule measurements of fluorescence emission spectra near spherical gold-nanoparticles[39] but only presented averaged single molecule spectra, which, unfortunately, did not show a strong spectral shaping. This is surprising given the strong effects that have been reported in the seminal ensemble-work by Ringler and co-workers[37]. In our work, we address the need of a more versatile approach to achieve strong shaping of not only averaged or ensemble, but single molecule spectra. First, we use top-down fabricated gold nanorods that we spectrally tune across the molecular resonance (Figure 4.1a). Second, we operate in liquid, which allows the molecule to probe the hot spot zone, and our wide-field approach allows for the acquisition of a large amount of single-molecule events of different interaction strengths. Selecting the stronger interactions we show that the fluorescence spectrum of single Rhodamine800 (Rho800) molecules can be dramatically altered by the interaction with the top-down fabricated antennas.

4.2 Average spectral shaping of single Rho800 molecules

The setup

In this experiment, Rhodamine 800 dye molecules (Rho800) are used due to the existence of two vibronic bands in the visible to near-infrared region of the spectrum

which are easily accessible by gold nanorods. To tune the spectral overlap between molecule and nanoantenna the length of the nanorods is varied from 60nm to 150nm, with a cross-section of 58nm x 58nm and a separation of 1.5 µm between adjacent nanorods. We rely on a home-built total-internal-reflection microscope (Figure 2.6a) equipped with an NA=1.49 objective (Olympus APON60x) and an EM-CCD camera (Andor iXon+ 897e) for wide-field detection, as described previously in chapter 2. The sample is plane-wave illuminated, with 633nm linearly polarized light at 5 kW/cm2 under the critical angle, and the collected single-molecule Rho800 fluorescence alongside its spectrum is imaged onto the camera by using a grating in front of the detector to disperse the light (Figure 2.6b). Importantly, the systematic stepwise increase of antenna length on the same sample allows simultaneous imaging of molecular emission spectra in the vicinity of particles with plasmon-resonances ranging from 650nm to 850nm, all through the Rho800 emission band.

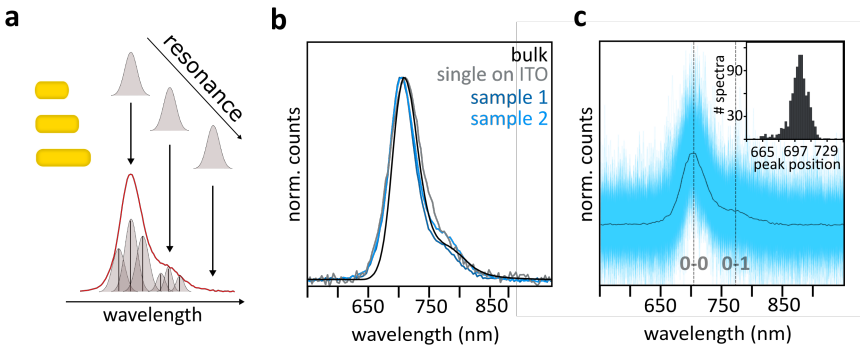

Figure 4.1: Single-molecule spectral emission control by plasmonic structures. a) The nanorod-length dependent antenna spectrum selectively enhances a subset of vibronic transitions responsible for single-molecule fluorescence emission. b) Comparison of Rho800 spectra measured in bulk solution (black) and as the sum of single Rho800 molecules landing on either bare ITO coverslips (grey) or far away, >400nm, from individual Au-antennas on ITO on the nanofabricated samples for two different arrays (light and dark blue); the main 0-0 transition and weak 0-1 side band can be appreciated. c) Plot of all 938 single molecule spectra used for computing the spectral average shown in b) (sample 2) alongside the mean. The inset shows a histogram of the spectral position of the 0-0 transition of all single molecule spectra.

Uncoupled Rho800 spectra

Experimentally, we submerge the antenna array in an ethanol solution of Rho800 and record widefield images at 20 frames per second to capture the stochastically occurring transient emission events of individual molecules, similar to the previous chapter 3. To put our observations into the context of coupling-induced modulations it is im-

perative to first determine the spectra of uncoupled single molecules and to quantify variations between individual spectra which might be due to a nanoscopically varying dielectric environment[16]. Contrary to previous studies of QDI (quarterrylene diimide) molecules[16], Rho800 shows only minor deviations between emission from freely diffusing and surface-bound molecules (Figure 4.1b). Importantly, the fluorescence spectra of 938 individually recorded single molecule events, which were detected spatially separated by >400nm from the nearest gold nanoantenna, are almost identical (Figure 4.1c).

Spectral-overlap-depending coupling

Following these control-experiments we now focus our attention on emission in the vicinity, i.e. <400nm, of the nanoantennas where we initially concentrate on ensemble-spectra obtained by averaging all single molecule events corresponding to a respective antenna length. We observe an altered behavior with spectral emission changes which are dependent on the precise nanoantenna length (Figure 4.2). For the shorter antennas with lengths between 80-110nm, the vibrational sideband - the 0-1 transition - of the fluorescence spectrum, around 775nm, is inhibited with almost all emission occurring via the main vibronic, the 0-0, transition. Contrarily, the emission in the vicinity of longer antennas, 120-140nm, shows enhanced 0-1 emission compared to the uncoupled spectrum (Figure 4.2). Yet, the changes are small compared to our anticipated calculations.

A simple coupling model

Qualitatively, the emission spectra in Figure 4.2 follow the plasmon-resonance of the gold nanorods, but to further rationalize our observations, we simulate the spectra with a simple coupling-model[37]. In ensemble-based studies, the total fluorescence is a weighted sum of all contributing molecules that feel different nanoscopic field enhancements in the vicinity of the nanostructure. Our single-molecule approach however allows ignoring fluorescence changes due to excitation enhancement, as we observe every single molecule spectrum separately. Consequently, the plasmonically shaped emission spectrum, F(ω), can be described as a simple sum of all vibronic transition probabilities $t_n(\omega)$ multiplied with a nanoantenna-resonance dependent enhancement factor $\sigma_n(\omega)$:

$$F(\omega) = \sum_{0}^{n} t_n(\omega) \cdot \sigma_n(\omega) \tag{4.1}$$

At room temperature organic molecules exhibit typical homogeneous linewidths of a few hundred wavenumbers, corresponding to electronic dephasing times on the order

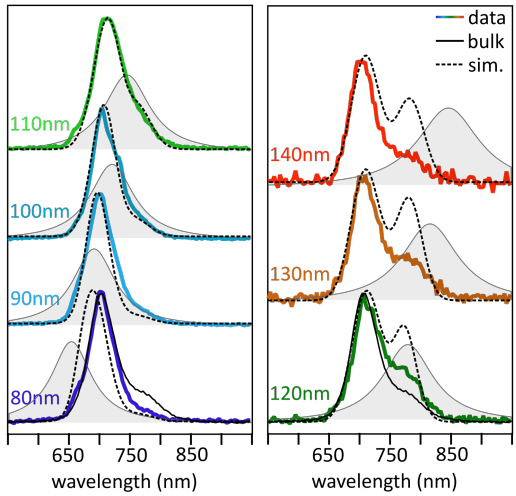

Figure 4.2: Spectral shaping of molecules next to nanoantennas. Averaged fluorescence spectra of many single molecule events near nanoantennas of different lengths (colored thick lines) alongside normalized extinction spectra of the respective nanoantennas (grey, filled), where we approximate the measured antenna scattering spectra by simple Lorentzians. The unenhanced spectrum of bulk solution (Figure 4.1b) is indicated with a solid black line. Simulated antenna-enhanced emission spectra, obtained by multiplying the unenhanced Rho800 emission with the nanoantenna spectrum, are shown as thin dashed black lines.

of a few tenth of femtoseconds[84]. Therefore, we simplify the coupling model to a multiplication of the antenna spectrum, $S(\omega)$, with the unperturbed molecular emission spectrum, $F_0(\omega)$:

$$F(\omega) = F_0(\omega) \cdot S(\omega) \tag{4.2}$$

Here, the nanoantenna scattering spectrum directly relates to its local density of states (LDOS) and thus to the frequency dependent emission enhancement of single emitters in the vicinity of the structure.

The model outlined above qualitatively reproduces the trends in the emission spectra, but suggests changes in ratio of the vibronic sideband to the main vibronic transition, that significantly deviate from our experimentally obtained results (Figure 4.2). This difference is due to the fact that we are comparing to ensemble-averaged emission spectra, which naturally include a wide range of antenna-molecule coupling strengths – which reflects directly on the distribution of distances and orientations of emitter and nanoantenna in the ensemble. As a result, weakly coupled molecules, with spectra resembling free, uncoupled, Rho800, reduce the shaping effect of the averaged coupling-induced spectra. To avoid this issue, we record single molecules and are able to select the relevant fraction of stronger coupled molecules.

4.3 Strong spectral shaping of single molecules

In this section, we will differentiate between 80-100nm and 120-140nm antenna length - measured on two different antenna arrays. The first array (sample 1), whose results were already presented in the previous section, contains a broad spectrum of antenna lengths ranging from 60nm to 150nm. The second antenna array (sample 2) only contains three antenna lengths - 120nm, 130nm, 140nm - ensuring sufficient statistics to investigate the spectral shaping in the case of the overlap of vibrational sideband (0-1 transition) and antenna resonance.

We select the spectra of stronger coupled molecules by thresholding the single molecule emission events above a certain intensity level. Even though our measurements are performed in the low-fluence regime, the intrinsically low Rho800 fluorescence quantum yield of approximately 0.25[85] allows associating intense emission with antenna-induced radiative rate enhancement and hence stronger coupling, see previous chapter 3. Figure 4.3a shows the spectral evolution of the 80-100nm and 120-140nm nanoantennas for intervals of increasing intensity, i.e. stronger coupling. Here, we sort the molecules by their integrated intensity, through defining intensity intervals between 300 and 3100 counts. We define 7 equally spaced intensity intervals for the shorter antennas, increasing the minimal intensity counts in each interval by 400 counts (e.g. first interval has spectra with counts between 300 and 700, second interval spectra with 700 and 1100 and so on). The longer antennas are sorted in 15 intensity intervals of 200 counts. For each interval, the average single molecule spectrum is shown. The three short antennas show essentially the 0-0 transition, irrespective of emission intensity, but for longer nanorods we observe a significant spectral evolution when analyzed analogously. We rationalize these trends by considering the spectral overlap between antennas and molecules, as discussed previously. For 80-100nm antennas, the intrinsically strong 0-0 transition is further enhanced, due to its near-perfect overlap with the antenna-resonance, thus resulting in considerable suppression of the 0-1 transition, even for relatively weak interactions. For the longer nanorods the opposite trend is observed, favoring the 0-1 interaction. However, the intrinsically low oscillator strength of the 0-1 transition results in only minor changes for weakly coupled emitters. Therefore, only the strongly interacting molecules show considerable spectral deviations from the unenhanced scenario. A direct comparison of the intensity, and hence coupling, dependent spectral evolution with our theoretical prediction shows that it is possible to reach, and even slightly surpass, the predicted degree of spectral shaping (Figure 4.3b).

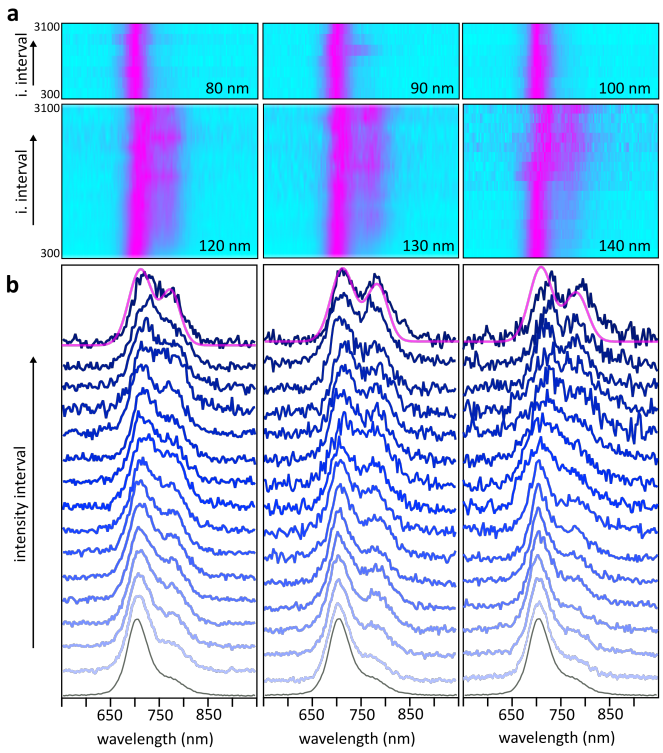

Figure 4.3: Change of spectra with increasing coupling. a) Spectral evolution with increasing fluorescence emission for nanoantennas of 80-140nm in length. For the short nanoantennas (80-100nm) the integrated intensity increases in intervals of 400 counts, up to a maximum of 3100 counts; for the longer nanoantennas (120-140nm) the intensity increases in intervals of 200 counts, up to a maximum of 3100 counts. b) Mean spectral evolution (blue) with increasing intensity intervals for the same 120-140nm nanoantenna array as in a), compared to the uncoupled spectrum (grey, bottom), and a theoretical prediction of the coupled spectra (pink, top).

The vibronic transition ratio

To quantify the coupling dependent vibronic decay we define the vibronic transition ratio R_{0-1}. To this end we fit the spectra shown in Figure 4.3b to the sum of two Gaussian functions and compute the normalized ratio of the Gaussian amplitudes, equivalent to the vibronic transition ratio

$$R_{0-1} = \frac{1}{R_{unE}} \cdot \frac{I_{0-0}}{I_{0-1}} \tag{4.3}$$

as a measure of the relative 0-0 to 0-1 oscillator strength, with I_{0-0} and I_{0-1} being the Gaussian amplitudes and the vibronic transition ratio of the unenhanced molecule R_{unE}=5.5 a constant that normalizes the ratio to unity for unenhanced molecules. In

other words, $R_{0-1} = 1$ corresponds to relative vibronic oscillator strengths reminiscent of an unenhanced Rho800 molecule, while $R_{0-1} > 1$ implies an enhancement of the main vibronic, the 0-0, transition and $R_{0-1} < 1$ an enhancement of the 0-1 transition. The two transitions are of equal strength, meaning that their peaks in the spectrum are of equal height, at a value of $1/5.5 \approx 0.18$. To obtain the normalization value of $R_{unE} = 5.5$ we kept the spectral separation between the two Gaussian functions fixed at 70nm to ensure a fit to the weaker vibronic sideband and calculated the mean value of the fit to samples 1 and 2 in Figure 4.1b. We maintained the fixed separation in our analysis, to ensure convergence of the fit also at low signal-to-noise ratios. However, owing to the clear presence of two peaks in Figure 4.3b, we implied only a constraint fit to determine the vibronic transition ratios R_{0-1} in Figure 4.4a, keeping all fit parameters constraint, but not at a fixed value as for R_{unE}.

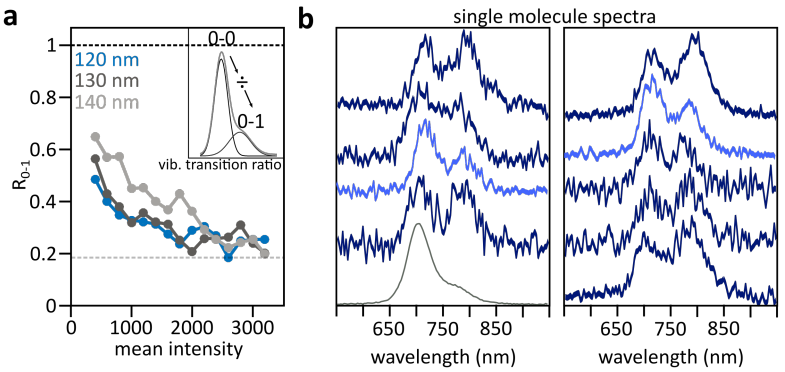

Figure 4.4: Vibronic transition ratio and single molecule spectra. a) Vibronic transition ratio of the 0-0 to 0-1 spectral bands (see inset), for the spectra presented in Figure 4.3b), normalized to the uncoupled Rho800 ratio (black dotted line at ratio 1). The grey dotted line at a value of 0.18 is the ratio below which the 0-1 vibronic sideband transition becomes stronger than the 0-0 transition. b) Selected spectra of interacting single Rho800 molecules next to 120-140nm nanoantennas; dark blue shows a 0-1 peak higher than the 0-0 peak.

The analysis outlined above shows that already the weakest, or most-uncoupled emitters are affected by the presence of the nanorods, showing vibronic transition ratios R_{0-1} reduced from 1.0 to ~0.6 (Figure 4.4a). With increasing emission intensity, the ratio changes dramatically, reaching values below 0.2, which corresponds to the 0-1 transition being of equal strength as the normally dominating 0-0 transition, which is a rather interesting scenario where the LDOS of the nanoantenna compensates for the unfavorable wavefunction-projection of the respective vibronic transitions. The ratios discussed thus far are intensity-filtered averaged single-molecule spectra but even larger deviations are observed for single molecules (Figure 4.4b). It should be noted

that we simultaneously observe a considerable fraction of strongly emitting molecules with essentially unaltered spectra, thus underlining the need for single-molecule observations to uncover the true spectral-control-potential of the gold nanorod structures employed here.

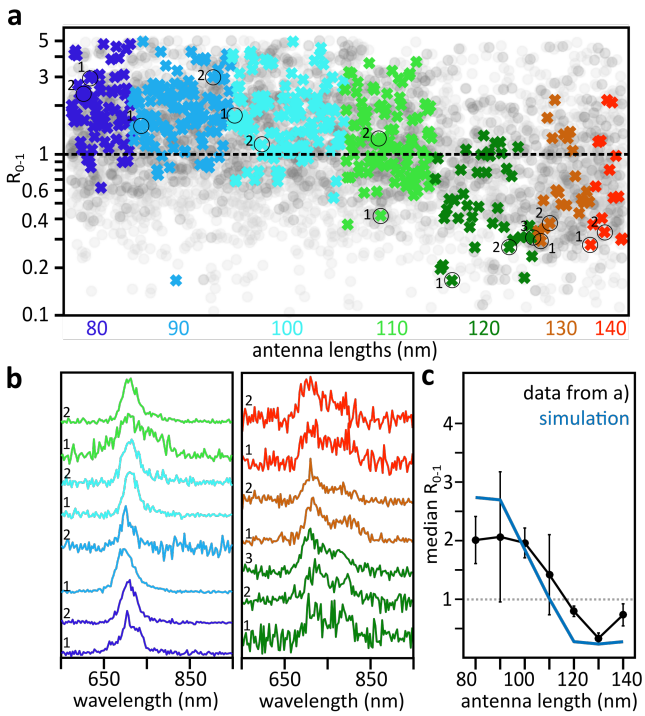

Figure 4.5: Single molecule vibronic transition ratio. a) Single molecule 0-0 to 0-1 vibronic transition ratios R_{0-1} sorted according to antenna lengths, measured on sample 1 only (all molecules: grey, low intensity threshold: dark grey, high intensity threshold: color-coded). The grey dotted line indicates the normalized ratio of the uncoupled system, $R_{0-1} = 1$. b) Selected single molecule spectra, for the molecules indicated by the circles in a). c) Median vibronic transition ratio R_{0-1} for the colored data presented in a), with overlaid simulation-results, for which we approximate the measured antenna scattering spectra by simple Lorentzians to obtain F(ω) and hence a simulated R_{0-1}. Grey dotted line: R_{0-1} for the free, uncoupled, Rho800 molecule. All shown data stems from the measurements of sample 1 only.

We conclude with a full single-molecule analysis of the antenna length dependent changes in molecular emission spectra, following the Gaussian fitting-based analysis as outlined above. For the interacting molecules, we determine R_{0-1} (Figure 4.5a) where a ratio lower (higher) than 1.0 corresponds to 0-1 enhancement (suppression), respectively. As anticipated from the ensemble data (Figure 4.2) the enhancement gradually moves from being 0-0 to 0-1 dominant as the nanoantenna-resonances sweep across the Rho800 fluorescence spectrum, with R_{0-1} decreasing from >5.0, through

1.0, to <0.2 for certain single molecule encounters. However, a more detailed analysis reveals strong spectral heterogeneity (Figure 4.5 b) albeit good agreement between the population-ensemble and our theoretically expectations (Figure 4.5c). It should be noted, that the laser excitation wavelength favors the shorter nanorod spectral resonance; therefore, we observe fewer high intensity spectra for the longer nanoantennas.

Beyond strongly differing fluorescence spectra obtained for identical nanoantennas we occasionally observe strong spectral modulations in Figure 4.5b (e.g spectrum 1 in dark blue and spectrum 2 in orange), in the form of sharp transitions, reminiscent of strong coupling induced spectral reshaping[86]. These modulations are surprising, as our plasmonic cavities, in the form of simple rod-antennas, should not support the ultra-small mode volume necessary to reach the strong coupling regime. Furthermore, in the advent of strong coupling we would expect fluorescence quenching, while experimentally we observe the opposite. One possible explanation could be single molecule surface enhanced Raman scattering (SERS) due to individual molecules landing at favorable hot-spot position on the nanoantenna, i.e. a SERS "hot particle"[14].

4.4 An excursion into SERS

4.4.1 Surface Enhanced Raman Scattering - A short introduction

Surface Enhanced Raman Scattering (SERS) is the effect of enhanced inelastic Raman scattering signal of molecules close to a plasmonic surface or structure. Raman scattering, like Rayleigh scattering, is a largely non-resonant process. In both cases, the scattering of a photon off an emitter can be described by bringing the emitters electron to a virtual energy state. From the virtual state, it comes back to a different vibronic ground state, causing the scattered photon to either maintain its energy (Rayleigh scattering), loose energy (Stokes Raman scattering) or gain energy (Anti-Stokes Raman scattering). This is visualized in Figure 4.6. Raman scattering is therefore a direct measure of the vibronic energies of the molecule.

Raman spectroscopy is used since its discovery in the early 20th century[87] to identify materials and single molecules and to study their chemical - vibrational - bonds as well as the intermolecular bonds. By placing the molecules next to a plasmonic structure - as first done by Fleischmann and co-workers in 1974[5] and identified thoroughly in 1977[6,7]-, the frequencies characterizing these bonds can be enhanced by up 11 orders of magnitude[88,89].

There have been extensive studies on SERS and single-molecule SERS (SM-SERS) to uncover molecular properties[14,65,90]. A review of these findings and applications, especially in biosensing[91], would go beyond the scope of this thesis and can be found

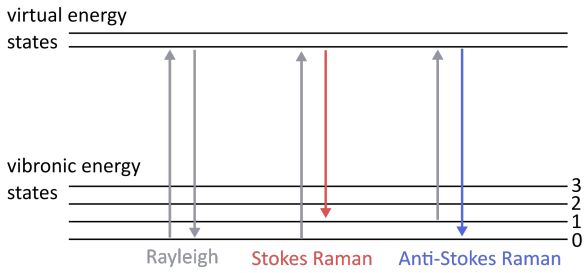

Figure 4.6: Three different scattering processes. a) Elastic Rayleigh scattering is caused by the excitation of an exciton in a molecule from the vibrational ground state to a virtual energy state, and the consecutive emission of a photon brings the molecule back to its vibronic ground state. b) Stokes and c) anti-Stokes radiation occurs if the the initial and final vibrational energy levels are different, with the initial one lower and the final one higher in the case of Stokes, b), and vice versa in the case of Anti-Stokes, c).

in numerous articles[92–94].

4.4.2 SERS versus surface enhanced fluorescence

Surface enhanced Raman scattering and surface enhanced fluorescence (SEF) are unavoidably tied to one another, as they originate - most probably - from the same electromagnetic enhancement process. While SEF can reach enhancement factors of up to 1500[15,95], its cousin - SERS - can reach enhancement factors of up to 10^{11}. There is often a direct competition between fluorescence and Raman scattering, as we will also see in this section. However, there are important differences between the two mechanisms. While the quenching of fluorescence prohibits molecules to experience more fluorescence enhancement when undercutting a certain distance to a nanostructure (typically 3-5 nanometers)[3,4], SERS intensities continue to increase when the distance to the metal is decreased[96]. Thus the strongest SERS signals are observed when placing a molecule directly on top of the metal, since energy losses to the metal can be ignored in the Raman scattering process. As the fluorescence detection, photobleaching and photodissociation are processes that hinder the detection of SERS signals. Contrarily to the fluorescence signal, the spectral footprint of SERS is dependent on the wavelength of the probing photon, as in Raman scattering the molecule is brought to a virtual energy state that depends on the exciting energy. Hence, the Raman shift can be calculated via

$$\Delta\nu = (\frac{1}{\lambda_0} - \frac{1}{\lambda_1}) \tag{4.4}$$

where λ_0 is the excitation wavelength and λ_1 the wavelength of the Raman peak in the spectrum. The Raman shift is presented in units of cm^{-1}.

Results of SERS vs. SEF in our widefield microscope

In order to verify the possible observation of SERS signals in Figure 4.5, we repeat the experiments described above, yet with two different illumination wavelengths λ_0 at 638nm and 660nm. We synchronize the sample illumination with two different lasers and fluorescence detection by the EM-CCD through the use of a field-programmable gate array (FPGA). Therefore, we ensure the consecutively recording of images that are illuminated at either 638nm or 660nm, both on the same antenna. Under these experimental conditions signals due to Raman scattering will spectrally shift by approximately 522cm^{-1} - the difference between the excitation wavelengths - whereas fluorescence emission should be spectrally unaffected. These measurements rely on our capability to record single molecule spectra in two consecutive frames, which is difficult to achieve with Rho800, showing predominantly transient single molecule emission events. However, Rhodamine 700 (Rho700), which is structurally almost identical to Rho800, seems to exhibit slightly altered surface interactions, which often results in temporally longer lasting emission events. The favorable overlap of laser emissions and Rho700 absorption also contributes to the enhanced probability of encountering SERS signal, as seen in Figure 4.7 .

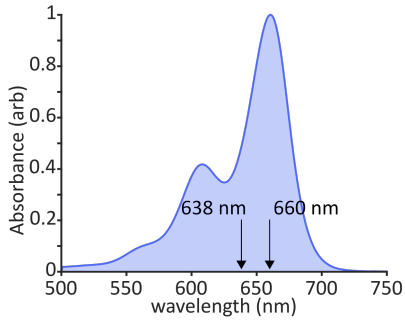

Figure 4.7: Absorption spectrum of rhodamine 700 in ethanol, alongside the two laser wavelengths for SERS excitation.

Therefore, we perform the two-color excitation experiments using Rho700. Similar to the previous section, we observe antenna-dependent median spectra that change with the antenna length for both laser excitation wavelengths, as shown in Figure 4.8. We also observe certain peaks in the median spectra that shift with excitation wavelengths, which is the clear indicator of observing SERS spectra.

Consecutively, we can discard those single molecule spectra that clearly show a shift

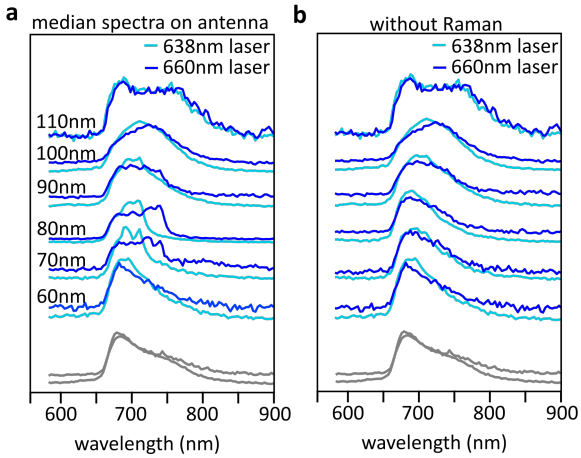

Figure 4.8: Median spectra of single rho700 (tresholded above 6000 counts) landing next to different antennas, for two different excitation wavelengths. Part (a) shows the median spectra as measured, without removing obvious single molecule SERS spectra. Part (b) shows the Raman-free median spectral evolution after removing the SERS spectra.

in peaks for the two different excitation wavelengths. We then obtain the clean median spectra without SERS peaks, seen in Figure 4.8b. The clean median spectra for Rho700 on different antennas show a spectral change which depends on the overlap of molecules emission spectrum, shown in grey in Figure 4.8, and the antenna resonance. For longer antennas the vibrational 0-1 sideband is enhanced significantly, as it overlaps with the respective antenna resonances as described extensively in the previous section. The spectral cut-off seen on the blue side of the spectra is caused by the long-pass filters used to eliminate the excitation wavelengths.

4.4.3 SM-SERS spectra

We now take a closer look at the many SM-SERS spectra recorded in our microscope. Therefore, we plot the spectra comprising the median spectra in Figure 4.8a for the most resonant antennas (70nm to 90nm length) for the two different excitation wavelengths, which is seen in Figure 4.9. Our setup clearly allows the recording of many of single molecule spectra, with the majority showing narrow and shifted peaks when comparing 660nm and 638nm excitation, characteristic for SERS. The shift in the narrow peaks can be easily calculated using Equation 4.4. As an example, we take the lower-wavelength peak of the spectra showing double-peaks seen in Figure 4.9a for the 638nm laser, yielding a Raman shift of $\Delta\nu = 1181[cm^{-1}]$ for a peak-position at 690nm. Now we can calculate the expected shift of this peak when using the 660nm laser, which yields a peak position of 715nm, nicely corresponding to the position

observed for the laser excitation at 660nm (Figure 4.9a, top).

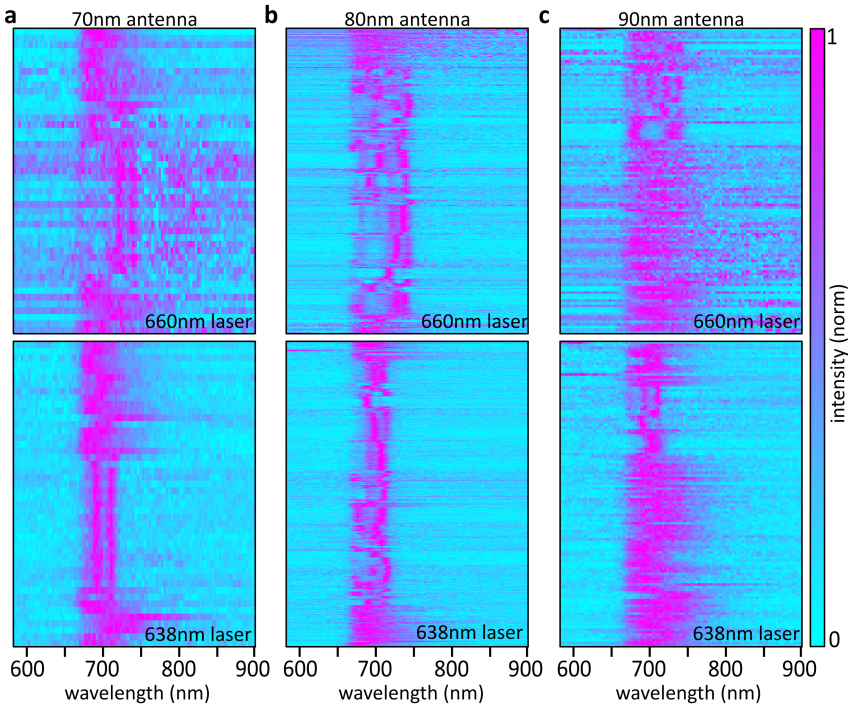

Figure 4.9: SM-SERS spectra for different antennas (a to c) and two different laser excitations, 660nm (up) and 638nm (down).

Figure 4.10 shows another representative spectra of strongly split, strong-coupling like, molecular emission of Rho700. After correcting for the illumination wavenumber (see equation 4.4), we indeed observe near-identical spectra, showing typical Raman peaks of organic bonds (double carbon bond, single carbon bond, carbon-oxygen bond etc.) at around $1500/1600 cm^{-1}$ and $1200 cm^{-1}$. We can finally conclude with certainty, that the spikes observed in Figures 4.5,4.8,4.9 and 4.10 are indeed SM-SERS spectra of favorably bound molecules.

As discussed previously, the high intensity SERS signals originate from molecules that are directly bound to the metallic surface, where fluorescence is quenched and therefore not visible. We suspect that the Rho700 has a slightly different chemical composition, allowing it to bind more favorably to the gold surface than Rho800. Furthermore, the excitation wavelength nicely overlaps not only with the absorption of Rho700, but also with the antenna resonance, which results in strong SERS signals.

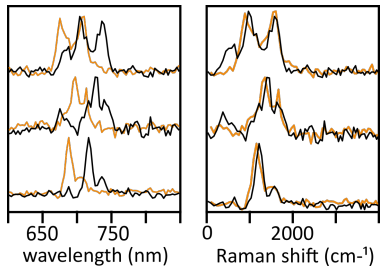

Figure 4.10: Selected Raman spectra of Rho700 molecules for 3 nanoantennas, excited at two different wavelengths of 638nm (orange) and 660nm (black), and the resulting Raman shift, showing independence on excitation wavelength.

4.5 Conclusion

In summary, we measured the fluorescence spectra of single Rho800 molecules in the vicinity of gold nanorods with precisely defined spectral resonances that we tune across the Rho800 emission. The spectrally dependent antenna-molecule coupling impacts the spontaneous emission rates of individual vibronic transitions, in a frequency-dependent manner, allowing to enhance the vibronic sideband to the level of the zero phonon line. Beyond control of vibronic transition rates, we observe the onset of single-molecule SERS, which is especially pronounced for Rho700, most likely due to favorable gold-molecule interactions.

We qualitatively describe the fluorescence reshaping with a simple model that estimates the anticipated emission spectra by computing the overlap of the nanorods' resonances and an unperturbed Rho800 spectrum. The model near-quantitatively reproduces the spectra of strongly coupled, intensely emitting, molecules but underestimates the transition perturbations on an ensemble level, which is unsurprising given the expected heterogeneity in interaction strength.

Our single molecule work suggests that it is possible to tune the relative rates of the 0-0 and 0-1 transitions by approximately 25-fold (5x up, 5x down). Here, either near-perfect suppression of the latter is possible by employing shorter, 80-100nm, nanorods or, alternatively, we can boost the 0-1 oscillator strengths up to a point where it acts as the molecules' main decay channel by using longer, 120-140nm, antennas. We anticipate that, instead of gold, using silver antennas with more narrow resonances, the tuning contrast of 25-fold can still be substantially enhanced.

Our work marks an important step towards nanoscale-manipulation of chemistry at the single molecule level and has direct implications for the rational design of future solar light-harvesting solutions based on plasmonic materials.

5

One-shot phase image distinction of plasmonic and dielectric nanoparticles

In this chapter we proceed from fluorescent based measurements as presented in the previous chapters to an interferometric technique, that measures the phase of the scattered light of nanoparticles.

Measuring the qualitative scattering phase of nanoparticles has become a hot topic in a crossover of many scientific fields as biology and nanophotonics, to sense, track and characterize the particles and their surrounding environment. Although the quantitative knowledge of the phase change in nanoparticles can deepen our understanding of nanoscale processes and develop methods of phase distinction, in practice it has proven hard to quantify and exploit the phase changes. Here, we implement a widefield holographic microscope that is capable of measuring the quantitative phase change of many different nanoparticles in a single image. We demonstrate distinction of different plasmonic and dielectric particles via their phase behavior. Furthermore, we implement a novel single-shot two-color excitation method, capable of rapidly identifying two types of nanoparticles on one sample.

This chapter is based on the following submitted manuscript:
L.Saemisch, N.F. van Hulst and M. Liebel, One-shot phase image distinction of plasmonic and dielectric nanoparticles, *submitted* (2021)

5.1 Introduction to Phase measurements

Phase is a rather elusive quantity in day-to-day life, but one of the most crucial parameters in physics and the life-sciences. As early as 1930s Fritz Zernike realized that the phase of light is extremely powerful and highly sensitive to tiny changes in the morphology of structures[97]. Since then, technology has advanced rapidly and different phase-detecting techniques are of crucial importance across many scientific fields. In nanoscale physics, the phase of a nanoparticle is intimately related to its nanoscale properties[98–101] and is a crucial parameter for tailoring complex photonic structures such as metasurfaces, which manipulate the amplitude, direction and polarization of light at nano- to microscales[102,103]. At the interface of nanophysics and biology phase measurements are used to detect protein binding to plasmonic structures[42,43,104] or to sense and track nanoparticles on different samples[105] and ultimately in biological specimen[106,107].

Qualitative vs quantitative phase imaging

Qualitatively recording the phase has emerged as a label-free technique in biology[108–110], to sense nanoscale cell dynamics and growth, which, amongst other medical applications[110], can ultimately help monitoring the alterations of cells due to viral infections and cancer. In qualitative phase imaging, the phase is normally turned into contrast in intensity, where it is more complicated to measure the absolute phase of a nanoparticle (or specimen), especially in a wavelength dependent manner. Such *qualitative* methods include traditional phase contrast (PC) microscopy techniques and differential interference contrast microscopy (DIC)[111,112], where the light passing through an object of different refractive indices will accumulate a phase shift that is visualized as a contrast in intensity on the camera, or the well-known interferometric scattering microscopy (iSCAT)[113–117].

With the invention of the digital camera in the mid-1990s, several digital phase-imaging techniques have evolved, which are commonly known as *quantitative* phase imaging (QPI) methods, assigning a number to the measured phase shift. One of the principal methods is known as digital holographic microscopy (DHM)[118], where amplitude and phase of a sample are measured, interfering an object wave and reference wave in-line or off-line with each other. A related technique is diffraction phase microscopy (DPM), a compact in-line interferometer, where object and image wave are created using the different refractive orders of a grating[119]. While the PC and DIC microscopy are still the prevalent techniques used in biological research, QPI techniques have a higher phase sensitivity and allow for a higher image contrast making them valuable and necessary for future applications in biology and biomedicine[110].

Measuring the absolute scattering phase

Even though many macro-scale phase measurements are relatively easy to implement, determining the absolute scattering phase of individual nano-objects is far from trivial. The above mentioned QPI methods quantify the phase solely as a relative number, however one has to consider the phase of the observation wave to measure an absolute phase shift of the particle. Furthermore, to measure *nano* objects, the sub-diffraction limited nature of the particle has to be accounted for. An experimental approach to directly and reproducible determine the absolute phase of such objects would both advance the observation-based development of nanophotonic materials and allow implementing novel imaging methodologies that exploit absolute phase measurements as a robust contrast mechanism for distinguishing and identifying different materials in a complex environment.

Here, we implement such an imaging platform in the form of a widefield off-axis holographic microscope that detects the pure scattering phase of many individual but different nanoparticles simultaneously, in a wavelength resolved fashion. Due to their inherent phase properties we can easily distinguish between plasmonic and dielectric particles. Furthermore, we extend our approach to a single-shot-technique, which rapidly identifies and distinguishes different NPs in a single widefield phase-image.

5.2 Widefield off-axis holographic microscope

5.2.1 Experimental set-up

Figure 5.1 schematically depicts our experimental setup that enables wavelength resolved absolute phase measurements by tuning the spectrally filtered output of a supercontinuum laser (SuperK Extreme) across the desired frequency range. The laser widefield illuminates the sample of interest, either by passing through the objective, in a reflection geometry, or by free-space illumination, in a transmission geometry (Figure 5.1, inset). In reflection, the laser light is injected via a 50:50 beamsplitter and focused into the center of the back focal plane of an oil-immersion objective. The objective (Olympus Apo N 60x TIRF objective with NA = 1.49) then collects sample scattering as well as the, reflected or transmitted, illumination wave.

The collected light is 1:1 relay imaged and divided by a 50:50 beam splitter to generate a reference- and an image-path. The latter passes an additional three-lens imaging system which, ultimately, generates a real-space image of the sample on the CMOS camera (acA2040-90um Basler ace, Basler AG) with a final magnification of 100x. To increase the contrast between the, often weak, sample scattering and the residual illumination wave, we, furthermore, insert a semi-transmissive Fourier-filter into the plane

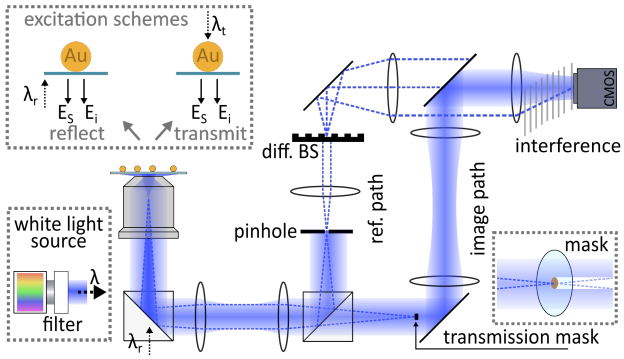

Figure 5.1: Schematic of the widefield off-axis interferometric microscope. Two possible excitation schemes are shown: reflection (excitation λ_R)and transmission (excitation λ_T), the scattered field is indicated as E_S and the partially reflected, or transmitted, illumination wave as E_i. A spectrally filtered white light source illuminates the NPs and both the illumination wave (blue dotted line) as well as the NP-scattering (blue blurred line) are guided through a relay imaging system until being separated into a reference and image path. A pinhole in the reference path eliminates the image information to create the reference wave, which passes a diffractive beamsplitter and its first order is interfered on the camera with the image wave. In the image path the illumination wave is selectively attenuated with a transmission mask (inset right lower edge), consisting of a small disk of gold evaporated onto a glass window.

conjugate with the back-focal-plane (BFP). The semi-transmissive Fourier-Filter consists of a gold disc of about 1 mm in diameter and 120 nm in thickness in the center of a glass window. It reduces the amplitude of the illumination field approximately 30-fold (Figure 5.1,lower right inset)[116], while the scattered field passes almost unhindered, since most of its amplitude is concentrated towards the critical angle.

The reference-path and the image path are equipped with the same three-lens imaging system, consisting of two pairs of identical lenses in each path (AC254-150-A, AC508-250-A, Thorlabs) with a third shared lens (AC508-500-A, Thorlabs). The reference path has a pinhole placed into the conjugate BFP[119], which essentially deletes all sample-related information, thus generating a plane-wave at the position of the camera. A diffractive beamsplitter (grating) is then used to recombine reference- and image-paths, as shown in Figure 5.1, and the two waves consecutively interfere on the camera. This arrangement can be regarded as an off-axis interferometer which in-situ generates its reference wave[119] and, furthermore, allows independent image manipulation by additional Fourier filtering. As a result, we measure simultaneously a phase response at the particles position and everywhere else on the sample, in the following noted as "p" and "nop", respectively, which allows us to extract the absolute particle phase at "p" positions by referencing to the “nop” positions.

5.2.2 Image formation and interference

To simplify the discussion we will initially consider the image- and the reference-path separately before discussing their interference. This allows us to describe their respective camera images $I_{img}(x,y)$, formed by the interference of the scattered light and the fraction of the illumination wave passing through the attenuation mask, and $I_{ref}(x,y)$, created through the pinhole, as::

$$I_{img}(x,y) = A_s^2(x,y) + \frac{A_i^2(x,y)}{a^2} + \frac{2A_sA_i}{a}cos(\Delta\varphi)(x,y) \tag{5.1}$$

and

$$I_{ref}(x,y) = A_{ref}^2(x,y) \tag{5.2}$$

, with x and y describing the position, A_s and A_i the electric field amplitudes of the scattering and illumination waves, and $\Delta\varphi$ the phase-difference between the two waves and a the attenuation amplitude of the semi-transparent transmission mask. A_{ref} is the amplitude of the reference wave, which is generated by passing the illumination wave through the pinhole in the BFP as outlined above. We experimentally select the illumination wave attenuation to ensure $A_s >> \frac{A_i}{a}$. This condition leads to the following two conclusions:

1. At the position of the particle ("p") the illumination as well as the interference term in Equation 5.1 can be neglected, since both are conditioned to be much smaller than the scattering term.

2. At the positions without particle ("nop") no scattering, and hence no interference term, is present.

Therefore, the mathematical description of the I_{img} simplifies to:

$$I_{img}(x,y) = \begin{cases} A_s^2(x_p,y_p) & \text{if a nanoparticle is present at x,y} \\ \frac{A_i^2(x_{nop},y_{nop})}{a^2} & \text{if no nanoparticle is present at x,y} \end{cases} \tag{5.3}$$

, where x_p and y_p describe image-regions where scattering particles are located and x_{nop} and y_{nop} regions without particles. Following this simplification, we are able to describe the holographically recorded interferometric image (see also[120]), considering A_s and A_i and A_{ref}, as:

$$\begin{aligned} I_{hol}(x,y) = A_s^2(x_p,y_p) + \frac{A_i^2(x_{nop},y_{nop})}{a^2} + A_{ref}^2(x,y) \\ +2A_{ref}A_scos(\Delta\varphi_{sref})(x_p,y_p) + \frac{2A_{ref}A_i}{a}cos(\Delta\varphi_{iref}))(x_{nop},y_{nop}) \end{aligned} \tag{5.4}$$

, where the phase-difference terms can be described as:

$$\Delta\varphi_{sref} = \varphi_s(x_p, y_p) - \varphi_{ref}(x_p, y_p) - \varphi_{gx} * x - \varphi_{gy} * y \tag{5.5}$$

and

$$\Delta\varphi_{iref} = \varphi_i(x_{nop}, y_{nop}) - \varphi_{ref}(x_{nop}, y_{nop}) - \varphi_{gx} * x - \varphi_{gy} * y \tag{5.6}$$

, with $\varphi_s(x_p, y_p)$, $\varphi_i(x_{nop}, y_{nop})$ and $\varphi_{ref}(x, y)$ being the position dependent phase of the scattered, illumination and reference wave, respectively.

Although the reference phase front is considered flat, the slight position variance stems from the diffraction properties of the lenses in our imaging system, and can be seen in Figure 5.2b. The camera-chip position dependent terms $\varphi_{gx} * x$ and $\varphi_{gy} * y$ are grating induced, linear phase-ramps that are necessary for off-axis holography based image processing and permit the spatial isolation of the interference terms in momentum space[121].

We will now outline three additional steps that are necessary to isolate the pure scattering phase from the experimentally acquired hologram (Equation 5.4): i) isolation of the interference terms; ii) separation of the reference and illumination phase and iii) accounting for de-focus and setup-induced phase effects.

5.2.3 Interference term isolation

Figure 5.2 outlines the computational steps taken to isolate the interference term of interest.

A fast Fourier transformation of the experimentally obtained image yields its momentum-space representation (Figure 5.2a, center), where the amplitude-square terms are located in the center and the interferometric terms are visible as diagonally-shifted mirror images. We then isolate one of the interference terms and multiply the cut image by a unity circle to set the frequency background around the interference term to zero. Next, we shift the interference term to the center (Figure 5.2a, right), which is equivalent to removing the two linear-phase terms φ_{gx} and φ_{gy} introduced via the grating (Equations 5.5, 5.6). Inverse Fourier transformation finally isolates the complex image, $I_{filtered}(x, y)$:

$$\begin{aligned} I_{filtered}(x, y) = A_{ref}(x, y)[A_s(x_p, y_p)e^{-i(\varphi_s(x_p, y_p) - \varphi_{ref}(x_p, y_p))} \\ + \frac{A_i}{a}(x_{nop}, y_{nop})e^{-i(\varphi_i(x_{nop}, y_{nop}) - \varphi_{ref}(x_{nop}, y_{nop}))}] \end{aligned} \tag{5.7}$$

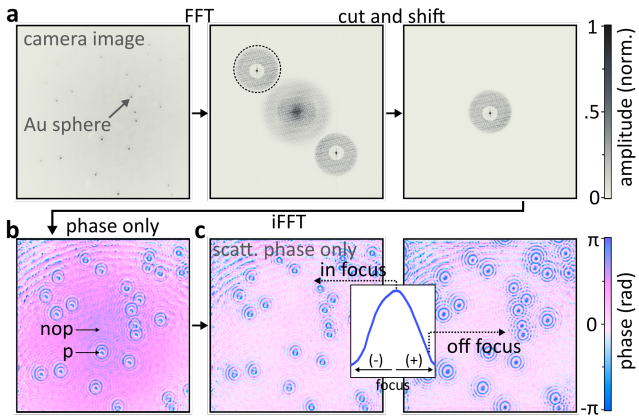

Figure 5.2: a) Computational analysis procedure after capturing the off-axis hologram (up,left) on the camera. Following a FFT (center) we isolate (dashed circle in center image) and shift the modulated interference contribution (right). We consecutively extract the phase (b), where example regions of particle (p) and non-particle (nop) phases are indicated by arrows. We correct for imperfections in the imaging system to fit and subtract the phase at nop-positions (c, left) and propagate the image digitally to find the optimal focus by identifying the focus position with highest intensity around a NP (c, right).

5.2.4 Separating the reference and illumination phase

Equation 5.7 shows that we can directly separate the image into its amplitude and phase terms but to obtain the pure scattering phase of a particle we need to take into account both the residual reference phase, $\varphi_{ref}(x, y)$, and account for the fact that the measured scattering phase is intrinsically coupled to the phase of the illumination wave:

$$\varphi_s(x_p, y_p) = \varphi_{s\_final}(x_p, y_p) + \varphi_i(x_p, y_p) \tag{5.8}$$

, with $\varphi_{s\_final}(x_p, y_p)$ being the pure scattering phase of interest. To access this information, we subtract the illumination wave phase described in the second term of Equation 5.7, assuming that its phase measured next to the particles is equivalent to its value at the particles' position. This is a justified assumption, since both the reference- and illumination- phase are strongly confined in momentum space and hence vary slowly. We consequently describe this slowly varying residual phase (Figure 5.2b) using Zernike polynomials (n=0-3: piston, tilt, defocus, astigmatism, coma and trefoil) and, following subtraction, obtain an image with a flat phase, of close-to-zero, over the entire image (Figure 5.2c, left). Additional division by the, separately measured, reference amplitude A_{ref} then yields the final amplitude image:

$$A_{corrected}(x,y) = A_s(x_p,y_p)e^{-i(\varphi_{s\_final}(x_p,y_p))} + \frac{A_i}{a}(x_{nop},y_{nop}) \tag{5.9}$$

5.2.5 Additional corrections

Lastly, having acquired the complex image, we can now computationally refocus the image by means of the angular spectrum method[122], where we define the focus as the z-position of maximum particle-amplitude (Figure 5.2c, inset). Furthermore, we apply an additional phase-offset to account for the semi transmissive mask, acting as Fourier-filter. Said filter adds additional material, in the form of a d=120nm gold film, to the optical path of the illumination wave. Since only the illumination wave passes the thin gold film, while the scattering wave propagates through air, we simply calculate the phase-difference as:

$$\varphi_{diff}(\lambda) = 2\pi(n_{gold}(\lambda) - n_{air}(\lambda))\frac{d}{\lambda} \tag{5.10}$$

, where n_{gold} and n_{air} are the respective refractive indices, d the thickness of the gold film and λ the wavelength. We note that even though a description relying on Fresnel equations could be used, we opted for the mathematically less complex description, as we did not note any significant deviations for the relatively thick films used here, even for different film-materials. This is described in detail in the appendix section 5.7 at the end of this chapter. Following the correction for the mask thickness, we extract the absolute scattering-phase of each individual NP as the phase value in the center of each particles' point-spread-function.

5.3 Experimental benchmark on nanorod antennas

We benchmark the performance of our setup on gold nanorods. We employ arrays of e-beam lithography fabricated gold nanorods (positive resist lithography, see Chapter 2) with a width/height of 50 nm and lengths increasing from 70nm to 220nm in steps of 10nm. These samples provide plasmonic resonances that span from the visible to the near infrared, which make them an ideal candidate for ensuring that spectrally resolved scattering phases can be obtained in an artifact-free manner.

Figure 5.3 shows amplitude and phase images, recorded for an array of nanoantennas, using a transmission geometry, at wavelengths of 615nm and 875nm, respectively. The shorter wavelength is off-resonant for the nanoantenna length-range and all phases show similar values, around -π/2. Using 875nm illumination we observe a scattering amplitude-maximum for the 150/160nm-long nanoantennas. As we pass the resonance, we identify a phase-flip of approximately π with shorter antennas exhibiting

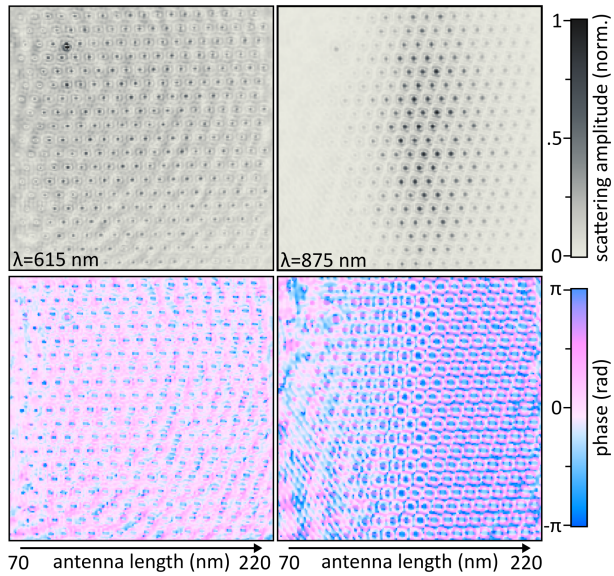

Figure 5.3: Intensity (up) and phase (down) images of gold nanoantennas with lengths increasing from 70 nm to 220 nm for two different excitation wavelengths, 615 nm (left) and 875 nm (right).

$\pi/2$ phases and longer antennas values around -$\pi/2$.

To gain further insight, we record the scattering amplitude and phase of all antennas as a function of illumination wavelength. To gauge the reproducibility of our measurements and phase corrections, we perform two measurements. First, we tune the illumination wavelength from 615nm to 975nm and then from 980nm to 620nm, both in steps of 10nm in ascending and descending order, respectively.

Figure 5.4a compares the amplitude data of both scans and highlights how the expected scattering resonance red-shift as we increase the antenna-length. At the same time, we observe a phase flip of approximately π as we move across the resonance of the individual antennas (Figure 5.4b), going from $\varphi = -\pi/2$ to $\varphi = \pi/2$. The intuitively expected π to zero phase-change for a driven harmonic oscillator, when passing the resonance from blue (higher frequency) to red (lower frequency), is shifted here because of a $\pi/2$ Gouy-phase shift due to scattering off a NP[123]. Therefore, we expect a $3\pi/2$ - $\pi/2$ phase change, which is equivalent to -$\pi/2$ - $\pi/2$ after phase-wrapping - which coincides with our observations. Importantly, the Gouy-phase shift is solely a near-field effect, similar to the well-known -$\pi/2$ shift when passing a nano-aperture. Additional Gouy-phase shifts when propagating the imaging system might occur but will not impact our measurement as both the scattered as well as the illumination

waves acquire said shifts, albeit at different planes in the relay-imaging system.

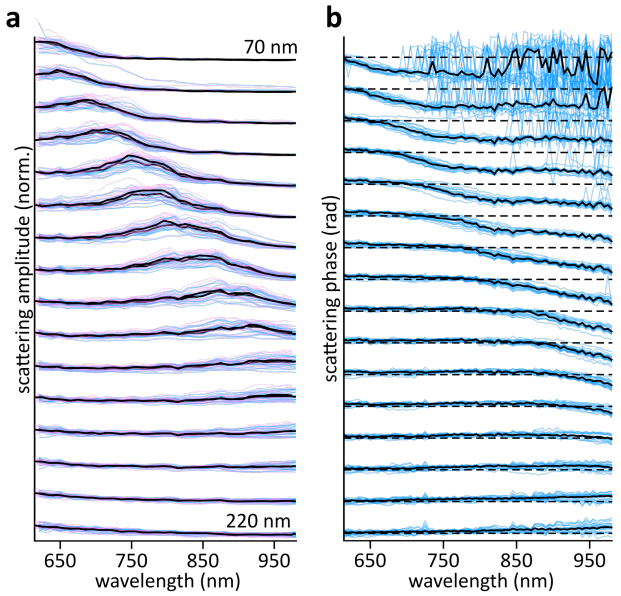

Figure 5.4: a) Scattering amplitude at different excitation wavelengths for all nanorods seen in Figure 5.3, length increases from top to bottom. The color indicates forward scanning of the excitation wavelength (615 to 975nm in steps of 10nm) – pink – and backward scanning (980 to 620nm). The medians of the two scanning procedures are seen in black for each nanorod length. b) Phase values for the different nanorods from a), combining the forward and backward scanning experiments. Single nanorods are seen in blue, the median for each length is presented in black. The individual phase curves are offset by π, the dashed line indicates $\varphi = \pi/2$ for the respective rod-length. Hence the nanorod phase change is observed from $\varphi = -\pi/2$ to $\varphi = \pi/2$, considering the phase wrapping from $3\pi/2$ to $\pi/2$. For representation purposes, we hence move the point of phase wrapping from π to 1.5 rad to avoid phase wrapping as we move through the particles' resonance.

We note that the dramatic phase-fluctuations observed for shorter nanoantennas in the near-infrared spectral region are due to insufficient signal to noise ratio for these weakly scattering objects and not an intrinsic limitation of our experimental approach. Importantly, the data presented in Figure 5.4a and 5.4b is composed of two consecutively performed experiments, with 5nm shifted illumination wavelength, which highlights the robustness of our phase-extraction approach.

5.4 Gold and dielectric nanoparticles

5.4.1 Phase and amplitude change

Even though the lithographically fabricated nanorods described in the previous section are an ideal model system for gauging the robustness and operational reliability of our approach, most biophysical applications rely on considerably smaller spherical nanoparticles which are often detected in a so called back-scattering, or reflection, configuration, which avoids propagating through the sample[114,124,125]. Additionally, this configuration conveniently reduces the amplitude of the residual illumination wave, as only a fraction is back-reflected into the microscope objective, thus yielding favorable higher scattering to illumination wave ratios. To mimic the experimental conditions of a live-cell experiment where scattering from gold (Au) nanoparticles alongside scattering-background of the dielectric cellular environment might be simultaneously present, we perform phase and scattering amplitude measurements of Au and polystyrene (PS) nanospheres, with respective diameters of 60nm and 100nm, using the reflection geometry.

For the fabrication of the nanosphere samples, the cover glass (0.17mm) was first cleaned for 10min in acetone in the ultrasonic bath followed by 10min in milliQ water. Consecutively the coverglasses were exposed to oxygen plasma for about 10min. The particles are immobilized by spin coating aqueous polyvinyl alcohol dispersion (2%) of the respective nanoparticles.

Figure 5.5a shows results obtained for samples containing only Au or PS particles. As expected, the gold nanoparticles show a localized surface plasmon resonance (LSPR) around 550-560nm whereas the PS's scattering amplitude approximately scales with the anticipated λ^{-2} dependence, as expected from Rayleigh scattering. As we move through the gold nanoparticles' LSPR we observe a phase change, with a median value of $\Delta\varphi \sim 2.4$ rad, while the PS's phase changes by approximately 0.8rad. These results suggest that a phase measurement should allow distinguishing the two types of nanoparticles albeit their comparable scattering amplitudes.

Figure 5.6 further strengthens this hypothesis by comparing amplitude and phase images, acquired at two different wavelengths, for a mixed Au/PS sample. While the amplitude values are insufficient for separating Au from PS nanoparticles the phase-change suggests that two of the particles are resonant Au nanoparticles. Indeed, wavelength dependent phase and amplitude measurements, based on a mixed sample with a total of 81 nanoparticles (Figure 5.5b), allow recovering results reminiscent of the separate measurements (Figure 5.5a) by classifying the individual nanoparticles based on their wavelength-dependent phase response.

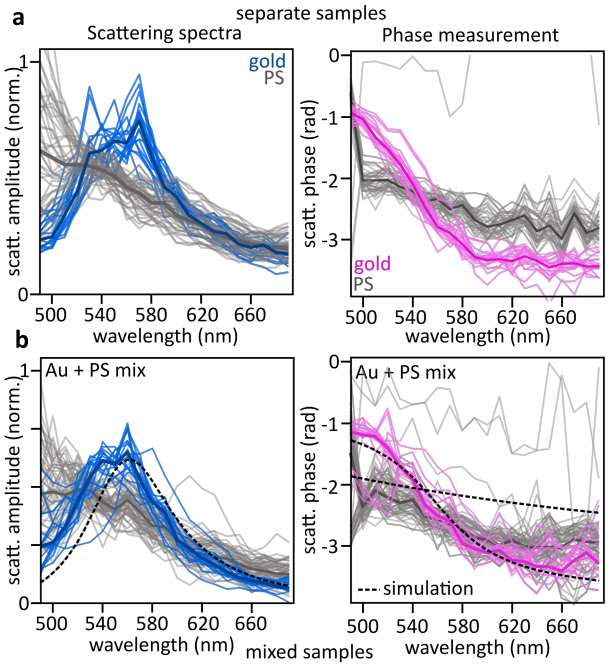

Figure 5.5: Phase and scattering properties of gold and dielectric nanoparticles. a) Scattering amplitude (left) and phase (right) for gold (blue and pink, respectively) and PS particles (gray). The faint lines show the measurement for each single particle, while the bold lines indicate the median value. b) Same as a), but for two mixed samples where PS and gold nanoparticles are measured at the same time and are distinguished by their phase properties. The black dotted lines show the simulations for the spectra of the gold nanoparticles, and the phase simulations for both gold and PS nanoparticles. We corrected for the transmission and the induced phased through the gold attenuation mask when normalizing the spectra and plotting the phase values.

5.4.2 Additional phase shifts in reflection geometry

The PS nanoparticle measurements presented in Figure 5.5 show a wavelength dependent phase that, generally, deviates from the, intuitively expected, $\varphi = 0$ rad for dielectric particles. Similarly, the Au nanoparticles phase is offset and slightly deviates from the expected π phase-change that we had previously observed for the Au nanorods using the transmission geometry.

These differences can be attributed to the fact that we are performing the measurements using a reflection geometry, see sketch in Figure 5.7. Under these conditions, the center-of-mass of the individual particles is, approximately, one radius, r, above the glass-air interface of the sample support. As a result, the scattered wave accumulates an additional, wavelength-dependent, phase-shift with respect to the illumination

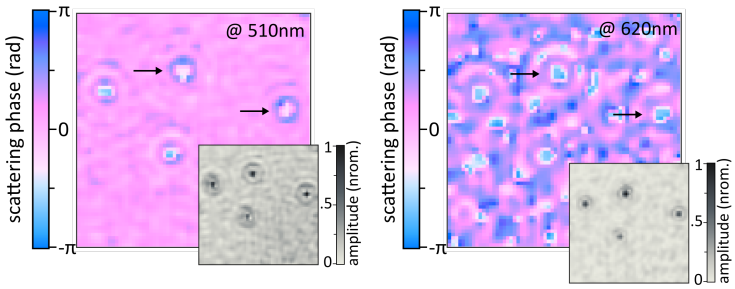

Figure 5.6: Phase and amplitude images at two different wavelengths of a mixed sample, showing two gold spheres (marked by arrows) and two polystyrene beads.

wave that is reflected at the interface. We estimate this shift as:

$$\varphi_{\Delta r}(\lambda) = 2\pi n_{PS-PVA/Au-PVA}(\lambda)\frac{2r}{\lambda} \tag{5.11}$$

, where $n_{PS-PVA/Au-PVA}$ is the wavelength dependent weighted refractive index of PS or Au in the PVA matrix, assuming that the NPs' material contributes as a half-sphere in a box with dimensions 2r x 2r x r.

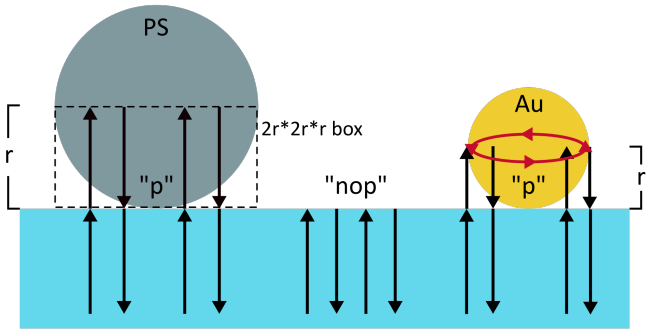

Figure 5.7: Schematic of phase accumulations in reflection geometry. Seen are the "p" positions for polystyrene and gold nanospheres, in which an additional, radius dependent phase shift is acquired with respect to the illumination wave at "nop" positions. The phase shift is determined via the refractive index, which is calculated considering the box shown in dashed lines assuming both particles are embedded in a PVA layer (see text). In red the additional light oscillation in a gold nanoparticle, resulting in a resonant phase behavior, is visualized.

5.4.3 Simulating the scattering phase

While Equation 5.11 is sufficient to describe the wavelength dependent scattering phase of the dielectric PS nanoparticles, when adding the additional $\pi/2$ Gouy-phase

shift we need to further account for the Au's LSPR to fully describe its scattering properties. We employ a simple Lorentzian resonator model to describe the LSPR, with a resonant frequency of $\nu_0 = 535.7$THz, corresponding to $\lambda_0 = 560$nm, and a damping of $\gamma = 82.4$THz. The simulation parameters are chosen based on the measured scattering amplitude (Figure 5.5), where we describe the Lorentzian-shaped scattering amplitude as:

$$A_s(\nu) = \frac{1}{\pi} \frac{0.5\gamma}{(\nu - \nu_{res})^2 + (0.5\gamma)^2} \tag{5.12}$$

And the scattering phase as:

$$\varphi_1(\nu) = atan(\frac{\gamma\nu}{\nu_0^2 - \nu^2}) + \pi/2 \tag{5.13}$$

Albeit being a simple one-frequency resonator model, the results obtained from Equation 5.12 and 5.13 qualitatively agree with our experimental observations (Figure 5.5c). In essence, the deviation from a full π phase shift is due to the large bandwidth of the LSPR which we only partially cover with our, comparatively, narrow spectral observation window. We attribute the minor discrepancies between our analytical model and the experimental data to the complex dielectric environment with the glass-polyvinyl alcohol-air interface whose exact dimensions are unknown. These variables have been shown to often considerably impact the absolute phase values[102], which complicates a quantitative description using a simple analytical model. Importantly, the directionality of the phase change observed, e.g. π to 0 or -π to 0, is directly related to which interference terms is analyzed (Figure 5.2a, center). The two terms across the diagonal are directly related, with one being the complex conjugate of the other thus effectively inverting the directionality of the phase change.

5.5 Spectral multiplexing: Identifying nanoparticles beyond the phase-offset

The dependence on the environment slightly hampers our ability to use the absolute scattering-phase to reliably identify metallic particles in a scattering environment, such as Au nanoparticles inside live cells, as the environment itself impacts the measured phase. In our experience, simulating absolute scattering phases with finite difference time domain methods is highly non-trivial (see appendix 5.8) and even after successfully implementing such a calculation one is left with the problem that the precise scattering environment is generally unknown when measuring in a complex biological

structure.

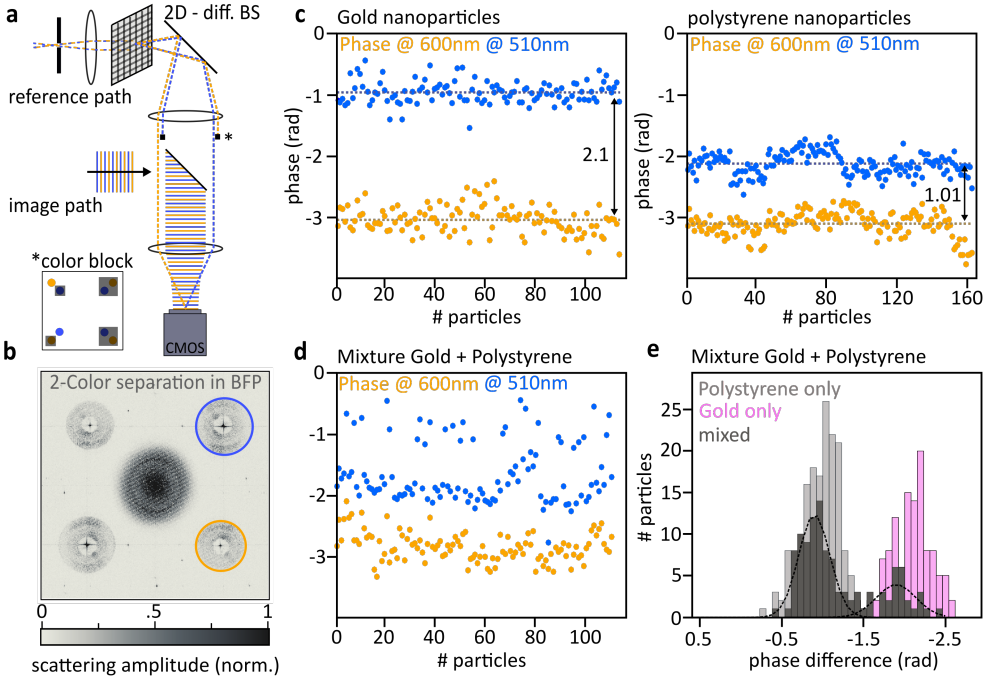

Figure 5.8: One-shot detection with a 2-color interference experiment. a) Drawing of a part of the modulated setup for two-color phase detection, the two excitation wavelengths are seen in blue (510nm) and yellow (600nm). The reference waves are sketched as dotted lines, while the image beams are visualized with continous lines. The diffraction orders are blocked by hard apertures, visualized as the two small black rectangles and seen in the small inset on the lower left. b) BFP image after the 2-color interference. Seen are all 4 modulated interference terms, while one component of the 510nm (600nm) interference is seen in blue (yellow). c) Measurement of gold (left) and PS (right) nanoparticles at two different excitation wavelengths of 510nm and 600nm. d) Measurement of a mixed sample of gold and polystyrene nanoparticles. e) Distribution of the phase difference at the two different wavelengths for each particle, plotted together with the distributions of the separate measurements from c). Two Gaussian distributions are drawn on top of the mixed histogram to visualize the two peaks.

Despite these complications, the markedly different wavelength dependent quantitative phases measured for metallic and dielectric particles should, nevertheless, allow distinguishing the two. Even though the absolute phase-values might shift, the relative phase-difference between two wavelengths is directly coupled to the resonance properties of the particles and, therefore, relatively unaffected by changes in the dielectric environment, albeit potential spectral LSPR changes of a few tens of nanometers in wavelength. A two-color measurement should thus allow identifying the nature of the nanoparticles.

As our spectral-scanning approach is time-consuming and hence not optimal for observing dynamic processes we opt for a multiplexed two-color illumination scheme where we employ two wavelengths, red- and blue-shifted with respect to NPs' resonance around 560nm. To implement said experiment in a single-shot manner we modify the initial imaging system (Figure 5.1) by replacing the 1D diffractive beamsplitter by a 2D beamsplitter, as schematically outlined in Figure 5.8a. Rather than selecting a single color from our laser source we opt for collinear two-color excitation, employing wavelengths of 510 nm and 600 nm. The two-color image is detected in a colorblind fashion, as previously. To, nevertheless, distinguish the contributions of the individual wavelengths, we selectively block different colors in the diffraction orders of the beam-splitter (Figure 5.8a, inset). As such, we obtain single-color reference waves at distinctly different k-vectors, as seen in Figure 5.8a. As these reference waves interfere with the scattered electric field, they transfer the single-color image-information to distinctly different positions in momentum space (Figure 5.8b) which allows simple separation via Fourier filtering. Following the analysis procedure outlined above we retrieve two absolute phase values for each particle in our widefield image, from a single camera-exposure observation.

We, initially, measure pure Au or PS samples, the results of which are shown Figure 5.8c. Based on the spectrally resolved measurements we would have expected a phase-difference of approximately 2.4 rad (Figure 5.5 a), which is in good agreement with the measured value of 2.1 rad. Similarly, for PS we expected 0.8 rad, and observe 1.0 rad. Finally, we measure a sample which, simultaneously, contains both PS and Au nanoparticles and attempt distinguishing the respective particles based on our single-shot observation. The results obtained for 115 nanoparticles are presented in Figure 5.8d. To better visualize these observations, we plot the phase difference at the two wavelengths, for each individual particle (Figure 5.8e). We observe well-separated histograms, reminiscent of a bimodal distribution, which are well described by two Gaussian distribution functions centered at approximately 0.9 rad and 1.9 rad. The relative amplitude of about 3:1 of PS (0.9 rad) to Au (1.9 rad) nanoparticles is in good agreement with the concentrations of the respective particles prior to spin-coating.

5.6 Conclusion and Outlook

In conclusion, we successfully implemented a widefield off-axis holographic microscope that allows determining the wavelength dependent absolute scattering phase of any nanoparticle, both plasmonic as well as dielectric. We measured the particles' phase response in an intrinsically self-referenced manner by comparing the scattering-phase of interest to the, simultaneously obtained, phase of the illumination phase. Albeit

being an important ingredient for performing the holographic phase measurements, the absolute phase of the reference wave is irrelevant. We do not require external calibrations or complex corrections, with the only exception being the phase-term added by the semi-transparent transmission mask which is readily calculated for the relatively thick film used.

First, we measured in a single image the phases and scattering spectra of an array of gold nanorods of different lengths, whose phase change of approximately π across their respective LSPR is in good agreement with the expected results. We not only observe the anticipated phase-change but also measure the predicted $\pi/2$ Gouy-phase contribution, for scattering off a NP, which shifts the expected π to 0 change to - $\pi/2$ to $\pi/2$. We further measured the absolute scattering phase of small plasmonic and dielectric nanospheres and were able to readily distinguish metallic from dielectric NPs based on their wavelength dependent phase. To account for potential deviations in complex 3D environments and to nevertheless allow phase-based particle-identification, we devised a single shot two-color approach where the phase of every particle was simultaneously determined at two distinct wavelengths. The phase difference between these simultaneously performed experiments was then successfully used for particle-identification. We aim to use this approach in future tracking experiments in biological samples, such as gold NPs in cells, where the constant scattering environment of the specimen can be easily distinguished from the 2-color-phase properties of the NP.

5.7 Appendix 1: Gold and Palladium transmission mask measurements

In our phase measurements of gold and polystyrene beads we accounted for the accumulated phase when passing the 120nm gold transmission mask. To validate this additional phase-correction, we perform comparative measurements using the 120nm thick gold and an 88nm thick palladium mask. We opted for palladium as it is relatively easy to deposit and, additionally, shows a linear refractive index change over the visible/NIR spectral region, with a refractive index greater than one (Figure 5.9a).

To ensure comparable transmission amplitudes we fabricated an 88nm thick Pd mask and an Au mask with 120nm thickness, both of which transmit approximately 0.05%. Figure 5.9b shows the phase-difference acquired when passing the respective masks, calculated as $\varphi_{Au/Pd}(\lambda) = 2\pi\ n_{Au/Pd}\frac{2r_{Au/Pd}}{\lambda}$.

To verify this assumption, we perform consecutive phase measurements of the same gold nanoparticles using either the gold and palladium mask, respectively. Figure 5.9c shows good agreement between the transmission mask-corrected wavelength dependent

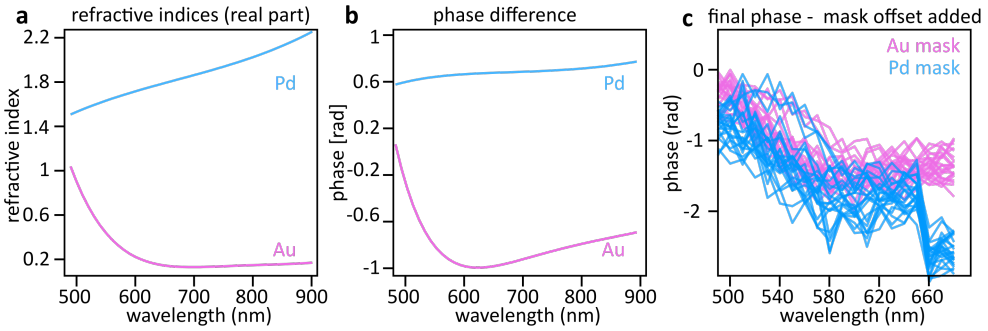

Figure 5.9: Gold vs. palladium mask. a) Refractive indices of palladium (blue) and gold (pink). b) Expected phase differences acquired between a wave passing air (n=1) or the 88nm palladium (blue) or 120nm gold mask (pink), respectively. c) Transmission mask-corrected phase measurements performed on the same nanoparticles using the gold (pink) or the palladium mask (blue).

scattering phase albeit a nominal correction-difference of approximately 2 rad (5.9b), thus validating our correction approach.

5.8 Appendix 2: Simulation of the absolute phase with FDTD

We have tried different approaches to calculate the absolute scattered phase of a nanoparticle using the FDTD solver. The most logical, and most correct approach seems to create two simulations, one containing the Au-NP and one without Au-NP, serving as a reference. The FDTD setup is depicted in Figure 5.10a, where the top drawing shows the FDTD setup with NP and the bottom one without NP. To simplify the simulations, we first used a glass/air interface without an embedding medium. A broadband plane-wave illuminates the sample (a TSFS source has also been tried, but did not change the results significantly), and three different 2D-monitors for detection are placed at -100nm, -200nm and -400nm from the glass/air interface.

First, we reference the complex electric field in the NP-simulation to the detected fields in the reference, the no-NP, simulation. While the electric fields in the NP simulation contain the scattering of the NP as well as the reflection of the illumination wave from the glass/air interface, the reference fields are composed of solely the illumination wave reflection. Consecutively we can subtract the respective complex electric field monitors in the NP and no-NP simulations to be left with solely the scattering signal for the three different monitors. The phase is calculated at every point of the monitor, by taking the real and imaginary (im) parts of the complex electric field E

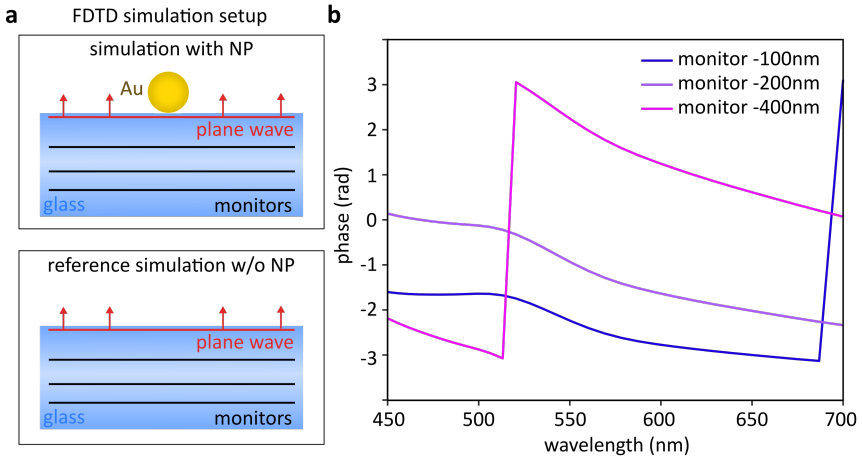

Figure 5.10: FDTD simulation of the absolute scattering phase of nanoparticles. a) FDTD simulation setup, (top) shows the simulation with a gold NP on top of a coverglass slide, illuminated by a plane wave. The scattering and the reflected illumination wave are detected by 2D monitors at three different positions, at -100nm, -200nm and -400nm from the glass surface. (down) shows the same simulation without NP, acting as a reference. b) Absolute scattering phase as a function of wavelength, calculated from the three monitors shown in (a), where the phase results in the reference simulation (a, down) are subtracted from the phase values in the NP-simulation (a, up).

and calculating the phase via $\varphi = atan(\frac{im(E)}{real(E)})$. The returned values are furthermore limited to the interval of $[-\pi, \pi]$ and are calculated for all wavelengths used in the plane-wave illumination. For simplicity reasons, we take the phase-median of the pixels in the center of the monitor, hence below the particles position. Figure 5.10b shows the obtained spectral phase curves for the three monitors. The phase change through the resonance is nicely calculated. Yet, we observe different phase offset values for different monitor locations, although the referencing to the reflection of the illumination field should prohibit different absolute phase values. The differing curves seem to be due to different contribution of the superposed planewaves with varying k-vectors. As we are dealing with a single standalone NP, this is unavoidable since the farfield will be created based on the a multitude of planewaves with varying k-vectors.

The FDTD-solver support agreed with us and could unfortunately not provide another way of calculating the absolute phase of a single nano-scatterer.

6

Conclusion and outlook

The research work presented in this thesis has investigated the nanoscale interaction of single molecules with nanoantennas, using a stochastic approach. The main goal has been to develop a versatile platform to watch thousands of encounters between single molecules and nanoantennas, to draw statistically valid conclusions on the different interaction strengths and their impact on the molecules properties. The nature of this experiment allows for the rapid distinction between strongly and weakly interacting molecules, managing to identify the rarest events normally hidden in single-molecule experiments that typically consist of a few tens to hundreds of encounters. While intensity measurements of the coupled system of molecule and nanoantenna are relatively easy to implement, they are not the most sensitive. With the final aim to observe small changes in the interaction, I implemented a holographic phase microscope that can quantify the scattering phase change of plasmonic particles, and is able to easily distinguish between many different nanoparticles at the same time.

6.1 Widefield microscopy for nanoscale interaction statistics and spectral manipulation of single molecules

A home-built widefield fluorescence localization microscope measured the nanoscale interaction of single molecules and nanoantennas via freely diffusing molecules probing nanofabricated optical antennas. Depending on the antenna length, either emission- or excitation-induced effects resulted in remarkable changes, not only in the observed super-resolved intensity reconstructions, but also in the emission spectra of the molecules. As a result, intensity and polarization measurements allowed for the

isolation of a small subset of strongly-coupled single molecules from an enormous number of less-coupled emitters and background, purely based on a statistical analysis that relies on physically meaningful expectations. Based on this analysis, I was able to resolve the expected double-spot excitation enhancement pattern present around dipole antenna-apexes. Near-field to far-field simulations using the FDTD solver also confirmed the experimental findings. Furthermore, a cross-polarization analysis revealed the mapping of the perpendicular component of the electric field, by isolating the few events that did not couple to the long axis of the nanoantenna.

In comparison to other works, the research presented in this PhD thesis implements a very controlled high-throughput method, that tunes systematically the overlap of molecule and nanostructure, providing hundreds of thousands of data points for statistical tresholding in a, furthermore, polarization resolved fashion. Results published earlier by Wertz and co-workers implemented the PAINT method to study the nanoscale interaction of nanoislands and nanotriangles with different molecules[30,126]. They showed (and quantified) a misplacement of a molecule next to a resonant and non-resonant nanostructure. While this research nicely identified the situations of excitation enhancement, emission enhancement or no enhancement on a few nanotriangles varying the sizes, molecules and excitation wavelengths, here I can directly, and more easily, compare the separate influences by observing many nanorods of different sizes. The polarization resolved analysis, as well as the large number of single molecules allowed to select the most special events and see the strongest coupling. Su and coworkers[31] worked with synthesized nanorods and observed a misplacement of the molecules fluorescence when overlapping with the nanorod's resonance - yet further, the systematic analysis of resonance overlaps, statistical tresholding and polarization resolved analysis were not presented. Other works using DNA labeling of nanostructures[32,35], measuring misplacements between the true single emitter position and the observed one, have the advantage of controlling the molecule's position up to a certain point - but they miss the simplicity and convenience of the easy exchange of sample (and therefore nanostructure) and molecule, and hence the systematic resonance tuning. The research on the decoupling of excitation and emission processes of a molecule in a plasmonic hotspot is probably one of the experiments closest to our work on the nanoscale interaction mapping[34]. Here, Mack et al. used a trimer structure and two spectrally different types of molecules to show either emission enhancement or only excitation enhancement using the PAINT method. They used different excitation polarizations to emphasize on different electric field distributions and therefore see different nanoscale interactions between the molecule and the structure. Their work, however, appears more noisy and lacks rigorous statistics - contrary to our stochastic approach. The work presented in this thesis has the advantage of measuring a

lot of encounters of different antennas and single molecules, exciting and detecting in both polarizations which makes it possible to treshold for DOLP and intensity of the molecular emission. Statistical filtering and therefore the high-throughput experimental approach made it possible to observe a transition from double spot to single spot, which would have probably remained unresolved or would have at least stayed fragmentary.

I extended the widefield localization microscope by adding a grating to the existing setup, with which both location and spectra of single emitters could be simultaneously imaged on the camera. Here, dramatic changes in the fluorescence spectra of single molecules next to different nanoantennas were revealed, where the vibronic sideband of the molecules emission went from a total suppression to an enhancement to the level of the main (0-0) vibronic transition. Remarkably, The high-throughput approach of combining many single molecules with many different antennas also led to the observation of rare, narrow peaks in the spectrum. These peaks shifted spectrally when employing two different laser excitation wavelengths simultaneously, which led to the conclusion that these peaks are a result of SERS.

More than ten years ago, Ringler and co-workers already showed strong effects in the spectral shaping of an ensemble of single molecules contained in a dimer-nanoresonator[37]. They observed that the vibrational sideband of the ensemble spectrum rose higher than the main vibronic transition for very small dimer-gap sizes. Recently, also Lee et al. performed single-molecule measurements of fluorescence emission spectra near spherical gold-nanoparticles[39], yet only presented averaged single molecule spectra, which, unfortunately, did not show a strong spectral shaping. While their approach allowed to quantify the single-molecule spectra as a function of distance from the molecule, the work in this thesis is based on intensity filtering of a lot of encounters of single molecules and nanostructures. My experimental approach allows to detect these rarely occurring events with statistical significance, where vibronic sidebands of single molecules are strongly enhanced to rise higher than the main electronic transition - the *one in a million* case.

Future experiments

Overall, the high-throughput experiment presented in this thesis is a robust method for finding specific and rare cases of stronger interaction out of an ensemble of many random occurrences. The simplicity of the setup allows for the easy exchange of sample, and hence nanostructures, and probing molecules. To achieve stronger coupling,

gap- or Bowtie antennas can be fabricated and probed by different molecules. The nanoscale mapping of the interaction of molecules and a three dimensional dipole nanoantenna, with a typical height of about 50nm, can be further improved and by full three dimensional mapping through the use of a cylindric lens in the detection path. This lens causes the fluorescence events to have elliptic shapes depending on the deviation from the focus and the fitting of a Gaussian function would therefore result in information of the x,y and z position of the molecule. This procedure would allow to identify the regions of strongest interaction on the nanoantenna surface and could reveal surface irregularities leading to ultra-strong electric field enhancements as needed for SERS detection.

One implementation of the high-throughput method might be in a bio-analytical laboratory, where a simple post-processing thresholding program will reveal specific interactions. Also, the occurrence of light re-localization provides an interesting concept for light concentration applications in general, such as in solar light harvesting.

Moreover, the strong spectral shaping marks an important step toward nanoscale manipulation of chemistry at the single molecule level, as any photoreactive molecular system composed of a reaction coordinate and a radiative decay, or loss, channel can be actively controlled by relying on the experimental coupling approach presented in this thesis. The possibility of strong spectral shaping has also direct implications for the rational design of future solar light- harvesting solutions based on plasmonic materials. Furthermore, it should be noted that the spectral shaping occurs fully in the weak interaction limit and does not need strong coupling, thus it would allow for the rational design of suitable plasmonic structures based on the molecules' native reactivity as the wave function is only minimally perturbed.

6.2 An interference microscope to measure absolute phase and distinguish nanoparticles

The last part of this thesis has paved the path towards measuring the change in phase of the coupled system of a plasmonic nanoantenna and a single molecule, by implementing a widefield interferometric microscope capable of measuring the absolute phase of plasmonic and dielectric particles. The experiment interferes reference and image paths to obtain the phase, where the latter contains intrinsic information about both the scattering of the nanoparticle and the illumination beam, which allows the extraction of the pure scattered phase shift of the nanoparticles. Consecutively, the absolute phase change of gold nanorods of different lengths was measured and a phase change of (nearly) π at the resonance frequency observed, in accordance with the

simultaneously measured scattering spectra. Scaling down the particle size, the phase change in small gold nanospheres was measured and successfully distinguished from dielectric nanoparticles via their different phase values. The lastly employed two-color approach measured the phase change in different nanoparticles in a single-shot image, eliminating phase-offset problems in different environments in the reflection geometry. Importantly, the employed interference setup allows to discriminate the simultaneous interference between each of the two colors with the image beam by their spatial separation in the Fourier plane. This is a simple, but powerful method that allowed to readily distinguish dielectric and plasmonic particles mixed on one sample detecting one image only.

Qualitative, label-free phase imaging techniques, such as PC and DIC, have long been dominating the biological research labs, providing contrast images of cells and intracellular features. Quantitative techniques however offer a more sensitive and high-contrast method to identify details and variations in materials and morphologies. Detection of phase has been reported in several experiments[99,100] to characterize and determine nanoparticles properties. In these experiments however, the interference occurred between the scattering and the reference branch only, resulting in a relative phase value. The interference experiment presented in this thesis work has the unique characteristic of interfering a reference beam with an image beam containing the nanoparticle scattering signal and a very attenuated signal form the reflection off the samples surface around the nanoparticles - in a widefield configuration. This allowed for the observation of the absolute phase change of π in a resonant nanoparticle together with the expected Gouy phase shift of $\pi/2$, which could have not been achieved with a relative interference measurement. Furthermore, our widefield interference setup can identify, and possibly track, many different nanoparticles at the same time - an advantage which other "single-point" experiments do not have, albeit presenting other nice features such as spectral interferometry[99].

Future experiments

The next step is to measure a change in phase of the combined system of molecule and nanoantenna. Here, one can think of controlled experiments where the molecule is placed at an exact position next to the nanostructure, while the change in scattering phase is observed by measuring the phase before and after the placement of the molecule. A more logical option in line with the method described in the previous section is to probe the interaction stochastically with freely diffusing molecules while continuously monitoring the phase change of the nanoparticle.

The widefield interferometric microscope has already proven to be exact and effective in measuring the scattering phase of plasmonic particles and in distinguishing many different particles at the same time. This approach is thus promising for future tracking experiments in biological samples, such as gold nanoparticles in cells, where the well-defined 2-color-phase properties of the nanoparticle act as a "label" that allows an easy distinction of the particle from the variable scattering environment of the specimen. In this context, the size of the nanoparticle is crucial as it affects nanoscale processes within the cell: While we are confident in measuring small (40nm) gold particles, which would sizewise have less impact on the cell and its processes, too small nanoparticles are more susceptible to Brownian motion hindering the tracking of actual intracellular processes.

6.3 A personal reflection on challenges and achievements

While the presentation of the experimental approaches and the obtained results seems to be straight-forward, there have been - naturally - multiple challenges on the way. The stochastic approach for the nanoscale mapping experiment requires long term nanoscale stability of the optical set-up. Here, a crucial point was to check and to improve the stage stability - where the first experiments failed on a non-floated optical table and a too-large distance between sample and optical table. Also, the handling of many terabyte-sized data sets and their filtering for different parameters required very structured analysis. Furthermore, the incidence and intensity of emission events of single molecules diffusing over nanoantennas was different for varying molecules, which resulted in various attempts for the spectral-shaping experiments - but also in the finding of the SERS signal and the consecutive implementation of a two-laser excitation approach to observe the Raman shift. Another difficult step was to achieve a working interferometric phase microscope - from calculating and meeting the requirements of the optical components to matching the time delay between reference and image paths. Here, the use of a less dispersive mask material (e.g. palladium instead of gold) would have been advantageous.

After almost five years of research, this thesis work has contributed largely to the field of nanoscale interactions between single molecules and nanoantennas, with the novelty of ensemble level observation of single molecule interaction. Here, large number statistics have been obtained to distinguish rare strong interactions that otherwise would have been lost in simple ensemble or low-number single molecule experiments. Furthermore, the interferometric setup, capable of distinguishing different nanoparti-

cles through their absolute phase values, is a promising candidate to explore biological processes in cells through tracking the movements of injected nanoparticles.

I truly hope that this scientific contribution will serve other scientists on their way to understand nano- and microscale processes in fundamental nanophotonic science, as well as biology - to advance the knowledge and technology needed for the future world.

Publications

List of publications included in this thesis:

L.Saemisch, M. Liebel and N.F. van Hulst, Isolating strong nanoantenna-molecule interactions by ensemble-level single-molecule detection, *Nanoscale* **12**,3723-3730 (2020)

L.Saemisch, M. Liebel and N.F. van Hulst, Control of vibronic transition rates by resonant single-molecule-nanoantenna coupling, *Nano Letters* **20**, 4537-4542 (2020)

L.Saemisch, N.F. van Hulst and M. Liebel, One-shot phase image distinction of plasmonic and dielectric nanoparticles, *submitted* (2021)

Other publications from the author not included in this thesis:

V. Remesh, M. Stührenberg, L.Saemisch, N. Accanto, Niek F. van Hulst, Phase control of plasmon enhanced two-photon photoluminescence in resonant gold nanoantennas, *Applied Physics Letters* **113**, 211101 (2018)

Bibliography

1. Born, M. & Wolf, E. *Principles of Optics* (1999).
2. Maier, S. A. *Plasmonics : fundamentals and applications* 223 (Springer, 2007).
3. Anger, P., Bharadwaj, P. & Novotny, L. Enhancement and Quenching of Single-Molecule Fluorescence. *Physical Review Letters* **96,** 113002 (2006).
4. Bharadwaj, P., Anger, P. & Novotny, L. Nanoplasmonic enhancement of single-molecule fluorescence. *Nanotechnology* **18,** 044017 (2006).
5. Fleischmann, M., Hendra, P. J. & McQuillan, A. J. Raman spectra of pyridine adsorbed at a silver electrode. *Chemical Physics Letters* **26,** 163–166 (1974).
6. Albrecht, M. G. & Creighton, J. A. Anomalously Intense Raman Spectra of Pyridine at a Silver Electrode. *Journal of the American Chemical Society* **99,** 5215–5217 (1977).
7. Jeanmaire, D. L. & Duyne, R. P. V. Surface Raman Spectroelectrochemistry Part1. Heterocyclic. *Journal Electroanal Chemistry* **84,** 1 (1977).
8. Li, J. F., Li, C. Y. & Aroca, R. F. Plasmon-enhanced fluorescence spectroscopy. *Chemical Society Reviews* **46,** 3962–3979 (2017).
9. Weitz, D. A., Gersten, J. I., Garoff, S., Hanson, C. D. & Gramila, T. J. Fluorescent lifetimes of molecules on silver-island films. *Optics Letters* **7,** 89 (1982).
10. Gersten, J. & Nitzan, A. Spectroscopic properties of molecules interacting with small dielectric particles. *The Journal of Chemical Physics* **75,** 1139–1152 (1981).
11. Wokaun, A., Lutz, H. P., King, A. P., Wild, U. P. & Ernst, R. R. Energy transfer in surface enhanced luminescence. *The Journal of Chemical Physics* **79,** 509–514 (1983).
12. Moskovits, M. Surface-enhanced spectroscopy. *Reviews of Modern Physics* **57,** 783–826 (1985).
13. Glass, A. M., Liao, P. F., Bergman, J. G. & Olson, D. H. Interaction of metal particles with adsorbed dye molecules: absorption and luminescence. *Optics Letters* **5,** 368 (1980).
14. Nie, S. & Emory, S. R. Probing single molecules and single nanoparticles by surface enhanced raman scattering. *Science* **275,** 1102–1106 (1997).
15. Wientjes, E., Renger, J., Curto, A. G., Cogdell, R. & van Hulst, N. F. Strong antenna-enhanced fluorescence of a single light-harvesting complex shows photon antibunching. *Nature Communications* **5,** 1–7 (2014).

16. Piatkowski, L., Gellings, E. & Van Hulst, N. F. Broadband single-molecule excitation spectroscopy. *Nature Communications* **7,** 10411 (2016).

17. Kramm, K. *et al.* DNA origami-based single-molecule force spectroscopy elucidates RNA Polymerase III pre-initiation complex stability. *Nature Communications* **11,** 1–12 (2020).

18. Schedlbauer, J. *et al.* Ultrafast Single-Molecule Fluorescence Measured by Femtosecond Double-Pulse Excitation Photon Antibunching. *Nano Letters* **20,** 1074–1079 (2020).

19. Pohl, D. W. *Optical Near-Field Scanning Microscope* 1982.

20. Kühn, S., Hakanson, U., Rogobete, L. & Sandoghdar, V. Enhancement of Single-Molecule Fluorescence Using a Gold Nanoparticle as an Optical Nanoantenna. *Physical Review Letters* **97,** 017402 (2006).

21. Singh, A., Calbris, G. & van Hulst, N. F. Vectorial Nanoscale Mapping of Optical Antenna Fields by Single Molecule Dipoles. *Nano Letters* **14,** 4715–4723 (2014).

22. Singh, A., de Roque, P. M., Hugall, J. T. & van Hulst, N. F. Nanoscale Mapping and Control of Antenna-Coupling Strength for Bright Single Photon Sources. *Nano Letters* **18,** 2538–2544 (2018).

23. Mivelle, M., Zanten, T. S. V., Neumann, L., van Hulst, N. F. & Garcia-Parajo, M. F. Ultrabright Bowtie Nanoaperture Antenna Probes Studied by Single Molecule Fluorescence. *Nano Letters* **12,** 5972–5978 (2012).

24. Betzig, E. *et al.* Imaging Intracellular Fluorescent Proteins at Nanometer Resolution. *Science* **313,** 1642–1645 (2006).

25. Hell, S. W. & Wichmann, J. Breaking the diffraction resolution limit by stimulated emission : stimulated-emission-depletion fluorescence microscopy. *Optics letters* **19,** 780–782 (1994).

26. Hess, S. T., Girirajan, T. P. K. & Mason, M. D. Ultra-High Resolution Imaging by Fluorescence Photoactivation Localization Microscopy. *Biophysical Journal* **91,** 4258–4272 (2006).

27. Rust, M. J., Bates, M. & Zhuang, X. Sub-diffraction-limit imaging by stochastic optical reconstruction microscopy (STORM). *Nature Methods* **3,** 793–795 (2006).

28. Cang, H. *et al.* Probing the electromagnetic field of a 15-nanometre hotspot by single molecule imaging. *Nature* **469,** 385–388 (2011).

29. Willets, K. A., Wilson, A. J., Sundaresan, V. & Joshi, P. B. Super-Resolution Imaging and Plasmonics. *Chemical Reviews* **117,** 7538–7582 (2017).

30. Wertz, E. A., Isaacoff, B. P. & Biteen, J. S. Wavelength-Dependent Super-resolution Images of Dye Molecules Coupled to Plasmonic Nanotriangles. *ACS Photonics* **3,** 1733–1740 (2016).

31. Su, L. *et al.* Super-resolution Localization and Defocused Fluorescence Microscopy on Resonantly Coupled Single-Molecule, Single-Nanorod Hybrids. *ACS Nano* **10,** 2455–2466 (2016).

32. Blythe, K. L., Titus, E. J. & Willets, K. A. Effects of Tuning Fluorophore Density, Identity, and Spacing on Reconstructed Images in Super-Resolution Imaging of Fluorophore- Labeled Gold Nanorods. *Journal of Physical Chemistry C* **119,** 28099–28110 (2015).

33. Ropp, C. *et al.* Nanoscale probing of image-dipole interactions in a metallic nanostructure. *Nature Communications* **6,** 1–8 (2015).

34. Mack, D. L. *et al.* Decoupling absorption and emission processes in super-resolution localization of emitters in a plasmonic hotspot. *Nature Communications* **8** (2017).

35. Raab, M., Vietz, C., Stefani, F. D., Acuna, G. P. & Tinnefeld, P. Shifting molecular localization by plasmonic coupling in a single-molecule mirage. *Nature Communications* **8,** 1–6 (2017).

36. Lim, K. *et al.* Nanostructure-Induced Distortion in Single-Emitter Microscopy. *Nano Letters* **16,** 5415–5419 (2016).

37. Ringler, M. *et al.* Shaping emission spectra of fluorescent molecules with single plasmonic nanoresonators. *Physical Review Letters* **100,** 1–4 (2008).

38. Dadosh, T. *et al.* Plasmonic control of the shape of the raman spectrum of a single molecule in a silver nanoparticle dimer. *ACS Nano* **3,** 1988–1994 (2009).

39. Lee, S. A. & Biteen, J. S. Spectral Reshaping of Single Dye Molecules Coupled to Single Plasmonic Nanoparticles. *The Journal of Physical Chemistry Letters* (2019).

40. Chikkaraddy, R. *et al.* Single-molecule strong coupling at room temperature in plasmonic nanocavities. *Nature* **535,** 127–130 (2016).

41. Zengin, G. *et al.* Realizing strong light-matter interactions between single-nanoparticle plasmons and molecular excitons at ambient conditions. *Physical Review Letters* **114,** 1–7 (2015).

42. Huang, Y. H., Ho, H. P., Kong, S. K. & Kabashin, A. V. Phase-sensitive surface plasmon resonance biosensors: Methodology, instrumentation and applications. *Annalen der Physik* **524,** 637–662 (2012).

43. Kabashin, A. V., Patskovsky, S. & Grigorenko, A. N. Phase and amplitude sensitivities in surface plasmon resonance bio and chemical sensing. *Optics Express* **17,** 21191 (2009).

44. Chong, S., Min, W. & Xie, X. S. Ground-state depletion microscopy: Detection sensitivity of single-molecule optical absorption at room temperature. *Journal of Physical Chemistry Letters* **1,** 3316–3322 (2010).

45. Novotny, L. & van Hulst, N. Antennas for light. *Nature Photonics* **5,** 83–90 (2011).

46. Muhlschlegel, P. Resonant Optical Antennas. *Science* **308,** 1607–1609 (2005).

47. Crozier, K. B., Sundaramurthy, a., Kino, G. S. & Quate, C. F. Optical antennas: Resonators for local field enhancement. *Journal of Applied Physics* **94,** 4632–4642 (2003).

48. Giannini, V., Fernández-Domínguez, A. I., Heck, S. C. & Maier, S. A. Plasmonic nanoantennas: Fundamentals and their use in controlling the radiative properties of nanoemitters. *Chemical Reviews* **111,** 3888–3912 (2011).

49. Govorov, A. O. & Richardson, H. H. Generating heat with metal nanoparticles. *Nano Today* **2,** 30–38 (2007).

50. Abadeer, N. S. & Murphy, C. J. Recent Progress in Cancer Thermal Therapy Using Gold Nanoparticles. *Journal of Physical Chemistry C* **120,** 4691–4716 (2016).

51. Taminiau, T. H., Stefani, F. D., Segerink, F. B. & van Hulst, N. F. Optical antennas direct single-molecule emission. *Nature Photonics* **2,** 234–237 (2008).

52. Mertens, H., Biteen, J. S., Atwater, H. A. & Polman, A. Polarization-Selective Plasmon-Enhanced Silicon Quantum-Dot Luminescence. *Nano Letters* **6,** 12–15 (2006).

53. Biteen, J. S., Lewis, N. S., Atwater, H. A., Mertens, H. & Polman, A. Spectral tuning of plasmon-enhanced silicon quantum dot luminescence. *Applied Physics Letters* **88,** 131109 (2006).

54. Cao, D. *et al.* Mapping the radiative and the apparent nonradiative local density of states in the near field of a metallic nanoantenna. *ACS Photonics* **2,** 189–193 (2015).

55. Carminati, R. *et al.* Electromagnetic density of states in complex plasmonic systems. *Surface Science Reports* **70,** 1–41 (2015).

56. Krachmalnicoff, V. *et al.* Towards a full characterization of a plasmonic nanostructure with a fluorescent near-field probe. *Optics Express* **21,** 930–933 (2013).

57. Ming, T., Chen, H., Jiang, R., Li, Q. & Wang, J. Plasmon-controlled fluorescence: Beyond the intensity enhancement. *Journal of Physical Chemistry Letters* **3,** 191–202 (2012).

58. Sharonov, A. & Hochstrasser, R. M. Wide-field subdiffraction imaging by accumulated binding of diffusing probes. *Proc. Natl. Acad. Sci. U.S.A.* **103,** 18911–18916 (2006).

59. Zhang, Z., Kenny, S. J., Hauser, M., Li, W. & Xu, K. Ultrahigh-throughput single-molecule spectroscopy and spectrally resolved super-resolution microscopy. *Nature Methods* **12,** 935–938 (2015).

60. Howell, S. B. *Handbook of CCD Astronomy* (Cambridge University Press, 2012).

61. McFarlane, N. J. & Schofield, C. P. Segmentation and tracking of piglets in images. *Machine Vision and Applications* **8,** 187–193 (1995).

62. Flauraud, V. *et al.* In-Plane Plasmonic Antenna Arrays with Surface Nanogaps for Giant Fluorescence Enhancement. *Nano Letters* **17,** 1703–1710 (2017).

63. Punj, D. *et al.* A plasmonic ' antenna-in-box ' platform for enhanced single-molecule analysis at micromolar concentrations. *Nature Nanotechnology* **8,** 512–516 (2013).

64. Stipe, B. C., Rezaei, M. A. & Ho, W. Single-Molecule Vibrational Spectroscopy and Microscopy. *Science* **280,** 1732–1753 (1998).

65. Kneipp, K. *et al.* Single Molecule Detection Using Surface-Enhanced Raman Scattering (SERS). *Physical Review Letters* **78,** 1667–1670 (1997).

66. Liu, T.-l. *et al.* Observing the cell in its native state: Imaging subcellular dynamics in multicellular organisms. *Science* **360,** eaaq1392 (2018).

67. Backlund, M. P., Lew, M. D., Backer, A. S., Sahl, S. J. & Moerner, W. E. The Role of Molecular Dipole Orientation in Single- Molecule Fluorescence Microscopy and Implications for Super-Resolution Imaging. *ChemPhysChem* **15,** 587–599 (2014).

68. Jungmann, R. *et al.* Single-Molecule Kinetics and Super-Resolution Microscopy by Fluorescence Imaging of Transient Binding on DNA Origami. *Nano Lett.,* 4756–4761 (2010).

69. Simoncelli, S., Li, Y. & Maier, S. A. Imaging Plasmon Hybridization of Fano Resonances via Hot- Electron-Mediated Absorption Mapping. *Nano Letters* **18,** 3400–3406 (2018).

70. Simoncelli, S., Li, Y., Corte, E. & Maier, S. A. Nanoscale Control of Molecular Self-Assembly Induced by Plasmonic Hot-Electron Dynamics. *ACS Nano* **12,** 2184–2194 (2018).

71. Taylor, A., Verhoef, R., Beuwer, M., Wang, Y. & Zijlstra, P. All-Optical Imaging of Gold Nanoparticle Geometry Using Super- Resolution Microscopy. *Journal of Physical Chemistry C* **122,** 2336–2342 (2018).

72. Axelrod, D. Carbocyanine Dye Orientation in Red Cell Membrane Studied by Microscopic Fluorescence Polarization. *Biophysical journal* **26,** 557–574 (1979).

73. De Silva Indrasekara, A. S. *et al.* Optimization of Spectral and Spatial Conditions to Improve Super-Resolution Imaging of Plasmonic Nanoparticles. *Journal of Physical Chemistry Letters* **8,** 299–306 (2017).

74. Thomas, M., Greffet, J.-J., Carminati, R. & Arias-Gonzalez, J. R. Single-molecule spontaneous emission close to absorbing nanostructures. *Applied Physics Letters* **85,** 3863 (2004).

75. Su, L. *et al.* Visualization of molecular fluorescence point spread functions via remote excitation switching fluorescence microscopy. *Nature Communications* **6,** 6287 (2015).

76. Baffou, G. & Quidant, R. Nanoplasmonics for chemistry. *Chemical Society Reviews* **43,** 3898–3907 (2014).

77. Zhang, Z., Zhang, C., Zheng, H. & Xu, H. Plasmon-Driven Catalysis on Molecules and Nanomaterials. *Accounts of Chemical Research* **52,** 2506–2515 (2019).

78. Gargiulo, J., Berté, R., Li, Y., Maier, S. A. & Cortés, E. From Optical to Chemical Hot Spots in Plasmonics. *Accounts of Chemical Research* **52,** 2525–2535 (2019).

79. Galego, J., Garcia-Vidal, F. J. & Feist, J. Suppressing photochemical reactions with quantized light fields. *Nature Communications* **7,** 1–6 (2016).

80. Kinkhabwala, A. *et al.* Large single-molecule fluorescence enhancements produced by a bowtie nanoantenna. *Nature Photonics* **3,** 654–657 (2009).

81. Farahani, J. N., Pohl, D. W., Eisler, H. J. & Hecht, B. Single quantum dot coupled to a scanning optical antenna: A tunable superemitter. *Physical Review Letters* **95,** 1–4 (2005).

82. Yuan, H., Khatua, S., Zijlstra, P., Yorulmaz, M. & Orrit, M. Thousand-fold enhancement of single-molecule fluorescence near a single gold nanorod. *Angewandte Chemie - International Edition* **52,** 1217–1221 (2013).

83. Curto, A. G. *et al.* Unidirectional Emission of a Quantum Dot Coupled to a Nanoantenna. *Science* **329,** 930–933 (2010).

84. Troisi, A. & Orlandi, G. Hole migration in DNA: A theoretical analysis of the role of structural fluctuations. *Journal of Physical Chemistry B* **106,** 2093–2101 (Feb. 2002).

85. Alessi, A., Salvalaggio, M. & Ruzzon, G. Rhodamine 800 as reference substance for fluorescence quantum yield measurements in deep red emission range. *Journal of Luminescence* **134,** 385–389 (2013).

86. Hugall, J. T., Singh, A. & Van Hulst, N. F. Plasmonic Cavity Coupling. *ACS Photonics* **5,** 43–53 (2018).

87. Raman, C. V. A new Radiation. *Indian J. Phys.* **2,** 387–398 (1928).

88. Blackie, E. J., Le Ru, E. C. & Etchegoin, P. G. Single-molecule surface-enhanced raman spectroscopy of nonresonant molecules. *Journal of the American Chemical Society* **131,** 14466–14472 (2009).

89. Ru, E. C. L., E. Blackie, Meyer, M. & Etchegoin, P. G. Surface Enhanced Raman Scattering Enhancement Facotrs: A Comprehensive Study. *Journal of Physical Chemistry C* **111,** 13794 (2007).

90. Stranahan, S. M. & Willets, K. A. Super-resolution optical imaging of single-molecule SERS hot spots. *Nano Letters* **10,** 3777–3784 (2010).

91. Bruzas, I., Lum, W., Gorunmez, Z. & Sagle, L. Advances in surface-enhanced Raman spectroscopy (SERS) substrates for lipid and protein characterization: Sensing and beyond. *Analyst* **143,** 3990–4008 (2018).

92. Langer, J. *et al.* Present and future of surface-enhanced Raman scattering. *ACS Nano* **14,** 28–117 (2020).

93. Etchegoin, P. G. & Le Ru, E. C. A perspective on single molecule SERS: Current status and future challenges. *Physical Chemistry Chemical Physics* **10,** 6079–6089 (2008).

94. Pilot, R. *et al.* A review on surface-enhanced Raman scattering. *Biosensors* **9** (2019).

95. Mohamed, M. B., Volkov, V., Link, S. & El-sayed, M. A. The 'lightning' gold nanorods: fluorescence enhancement of over a million compared to the gold metal. *Chemical Physics Letters* **317,** 517–523 (2000).

96. Kovacs, G. J., Loutfy, R. O., Vincett, P. S., Jennings, C. & Aroca, R. Distance Dependence of SERS Enhancement Factor from Langmuir–Blodgett Monolayers on Metal Island Films: Evidence for the Electromagnetic Mechanism. *Langmuir* **2,** 689–694 (1986).

97. Zernike, F. Phase contrast, a new method for the microscopic observation of transparent objects. *Physica* **9,** 686–698 (1942).

98. Husnik, M. *et al.* Quantitative experimental determination of scattering and absorption cross-section spectra of individual optical metallic nanoantennas. *Physical Review Letters* **109,** 1–5 (2012).

99. Gennaro, S. D. *et al.* Spectral interferometric microscopy reveals absorption by individual optical nanoantennas from extinction phase. *Nature Communications* **5,** 3748 (2014).

100. Khadir, S. *et al.* Full optical characterization of single nanoparticles using quantitative phase imaging. *Optica* **7,** 243 (2020).

101. Hauler, O. *et al.* Direct phase mapping of the light scattered by single plasmonic nanoparticles. *Nanoscale* **12,** 1083–1090 (2020).

102. Li, Z. *et al.* Controlling propagation and coupling of waveguide modes using phase-gradient metasurfaces. *Nature Nanotechnology* **12,** 675–683 (2017).

103. Yu, N. & Capasso, F. Flat optics with designer metasurfaces. *Nature Materials* **13,** 139–150 (2014).

104. Yesilkoy, F. *et al.* Phase-sensitive plasmonic biosensor using a portable and large field-of-view interferometric microarray imager. *Light: Science and Applications* **7,** 17152 (2018).

105. Jacobsen, V., Stoller, P., Brunner, C., Vogel, V. & Sandoghdar, V. Interferometric optical detection and tracking of very small gold nanoparticles at a water-glass interface. *Optics Express* **14,** 405 (2006).

106. Wit, G. D., Albrecht, D., Ewers, H. & Kukura, P. Revealing Compartmentalized Diffusion in Living Cells with Interferometric Scattering Microscopy. *Biophysical journal* **114,** 2945–2950 (2018).

107. Taylor, R. W. *et al.* Interferometric scattering microscopy reveals microsecond nanoscopic protein motion on a live cell membrane. *Nature Photonics* **13,** 480–487 (2019).

108. Frohlich, V. C. Phase contrast and differential interference contrast (DIC) microscopy. *Journal of Visualized Experiments,* 2008 (2008).

109. Kasprowicz, R., Suman, R. & Toole, P. O. Characterising live cell behaviour : Traditional label-free and quantitative phase imaging approaches. *International Journal of Biochemistry and Cell Biology* **84,** 89–95 (2017).

110. Park, Y., Depeursinge, C. & Popescu, G. Quantitative phase imaging in biomedicine. *Nature Photonics* **12,** 578–589 (2018).

111. Pluta, M. *Advanced light microscopy* (Elsevier, 1988).

112. Arnison, M. R., Larkin, K. G., Sheppard, C. J., Smith, N. I. & Cogswell, C. J. Linear phase imaging using differential interference contrast microscopy. *Journal of Microscopy* **214,** 7–12 (2004).

113. Lindfors, K., Kalkbrenner, T., Stoller, P. & Sandoghdar, V. Detection and spectroscopy of gold nanoparticles using supercontinuum white light confocal microscopy. *Physical Review Letters* **93,** 037401–1 (2004).

114. Kukura, P. *et al.* High-speed nanoscopic tracking of the position and orientation of a single virus. *Nature Methods* **6,** 923–927 (2009).

115. Taylor, R. W. & Sandoghdar, V. Interferometric Scattering (iSCAT) Microscopy and Related Techniques. *arXiv:1812.10765 [physics.optics]* (2018).

116. Liebel, M., Hugall, J. T. & van Hulst, N. F. Ultrasensitive Label-Free Nanosensing and High-Speed Tracking of Single Proteins. *Nano Letters* **17,** 1277–1281 (2017).

117. Ortega-Arroyo, J. & Kukura, P. Interferometric scattering microscopy (iSCAT): New frontiers in ultrafast and ultrasensitive optical microscopy. *Physical Chemistry Chemical Physics* **14,** 15625–15636 (2012).

118. Kim, M. K. Principles and techniques of digital holographic microscopy. *SPIE Reviews* **1** (2010).

119. Bhaduri, B. *et al.* Diffraction phase microscopy: principles and applications in materials and life sciences. *Advances in Optics and Photonics* **5,** 131 (2013).

120. Kühn, J. *Multiple-Wavelength Digital Holographic Microscopy* PhD thesis (2009).

121. Takeda, M., Ina, H. & Kobayashi, S. Computer-Based Topography and Interferometry. *Journal of the Optical Society of America A* **72,** 156–160 (1982).

122. Goodman, J. W. *Introduction to Fourier Optics* (2005).

123. Hwang, J. & Moerner, W. E. Interferometry of a single nanoparticle using the Gouy phase of a focused laser beam. *Optics Communications* **280,** 487–491 (2007).

124. Ueno, H. *et al.* Simple dark-field microscopy with nanometer spatial precision and microsecond temporal resolution. *Biophysical Journal* **98,** 2014–2023 (2010).

125. Cheng, C. Y., Liao, Y. H. & Hsieh, C. L. High-speed imaging and tracking of very small single nanoparticles by contrast enhanced microscopy. *Nanoscale* **11,** 568–577 (2019).

126. Wertz, E., Isaacoff, B. P., Flynn, J. D. & Biteen, J. S. Single-Molecule Super-Resolution Microscopy Reveals How Light Couples to a Plasmonic Nanoantenna on the Nanometer Scale. *Nano Letters* **15,** 2662–2670 (2015).